

Figure 1.

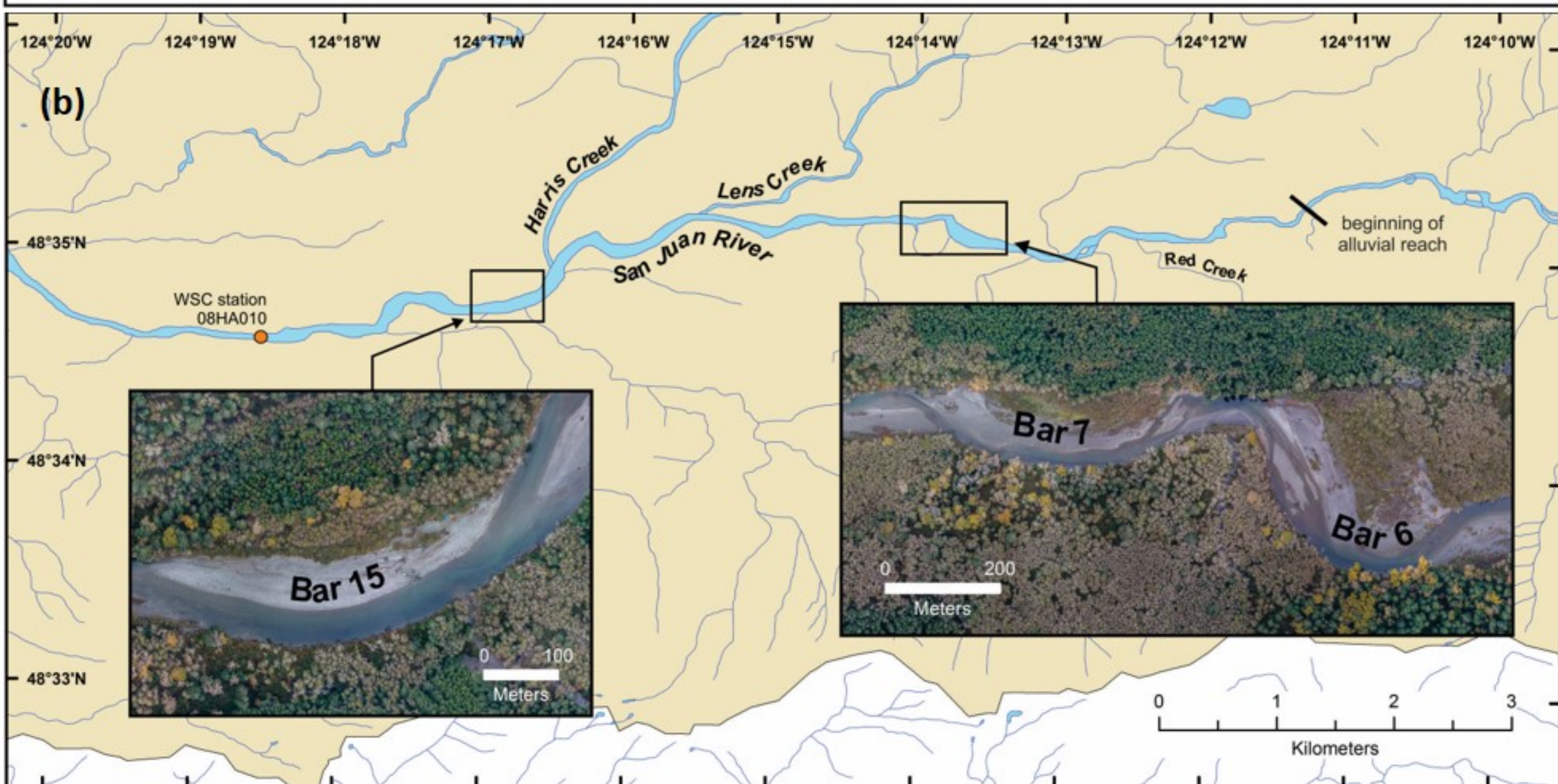
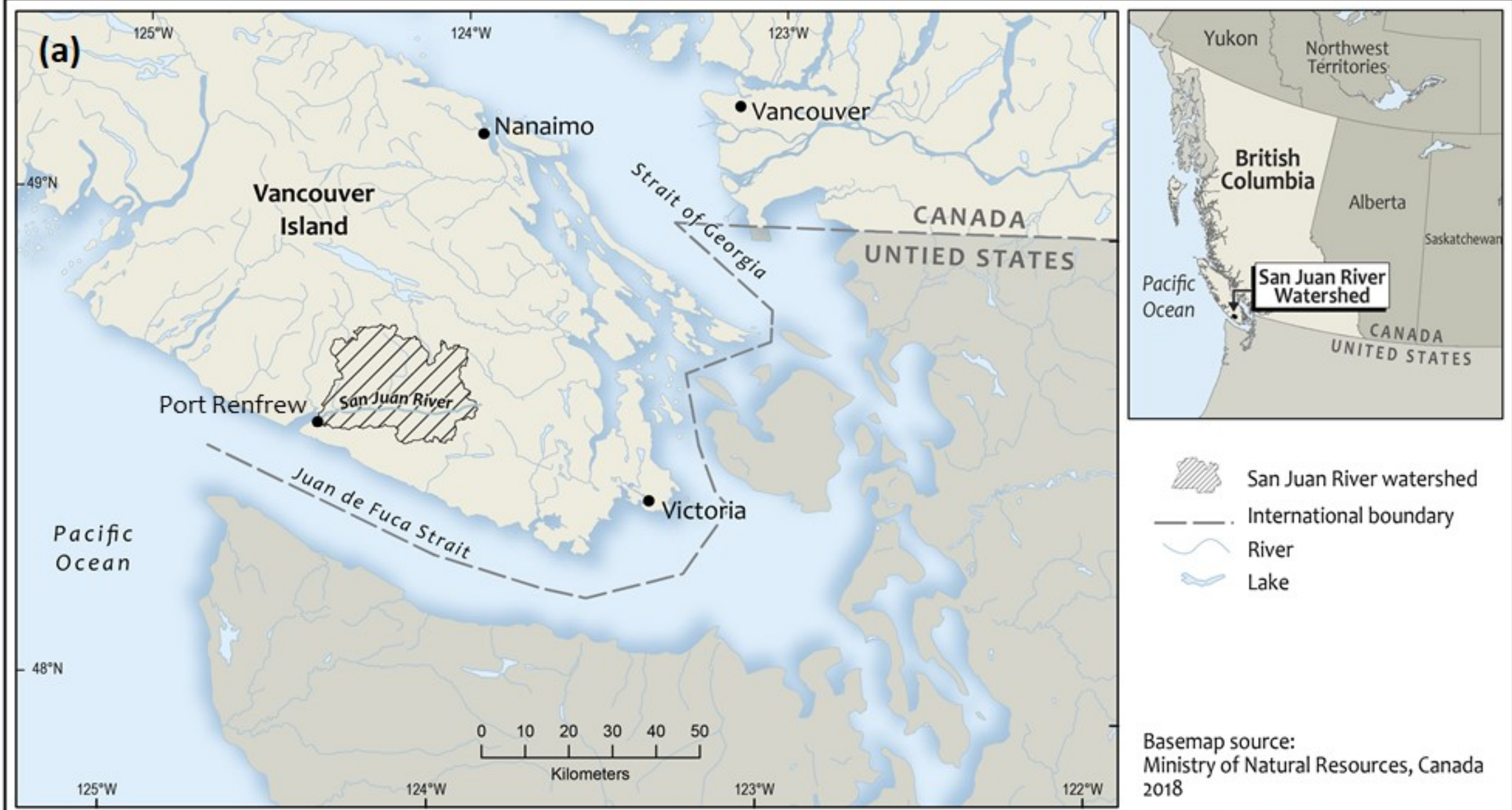


Figure 2.

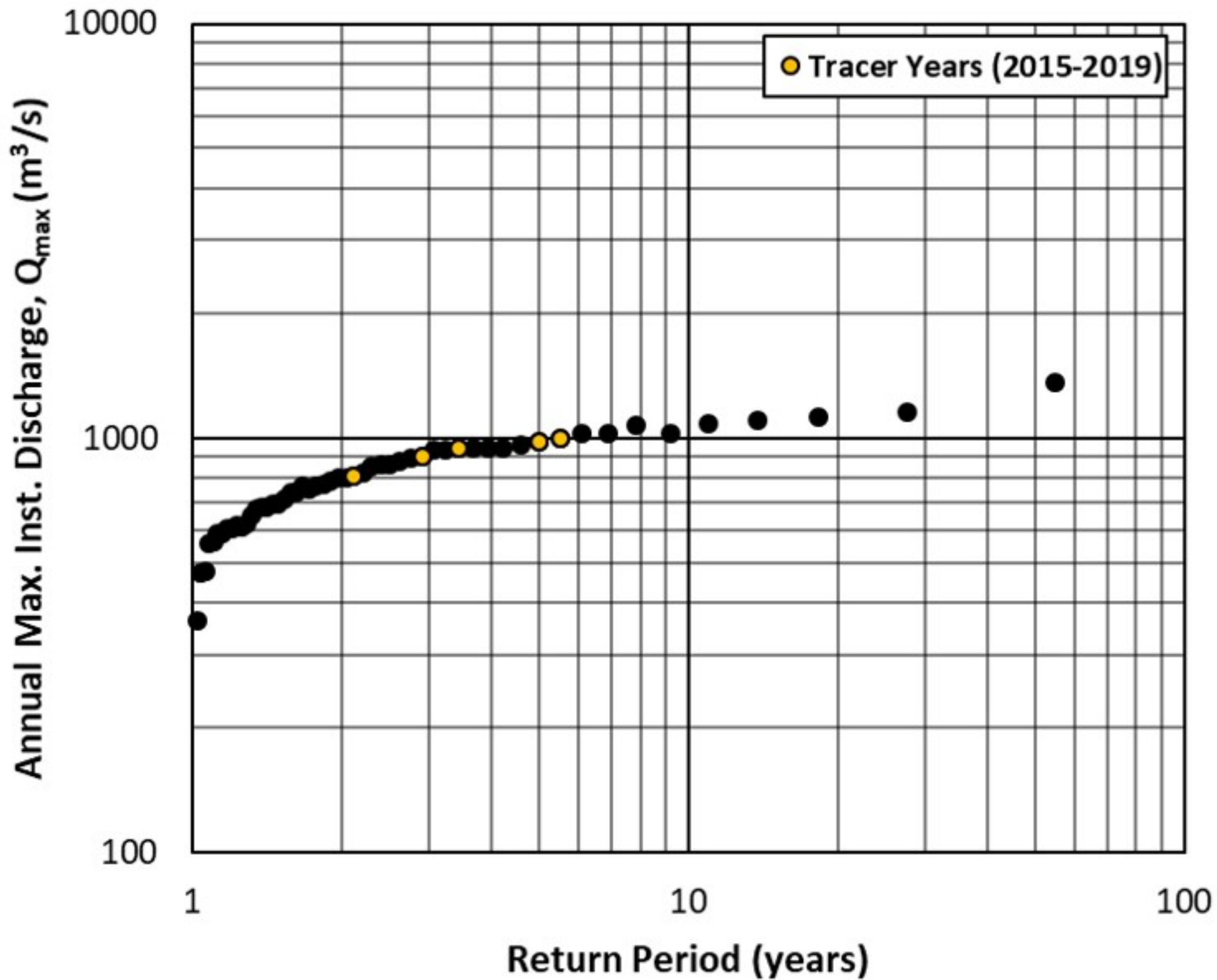


Figure 3.

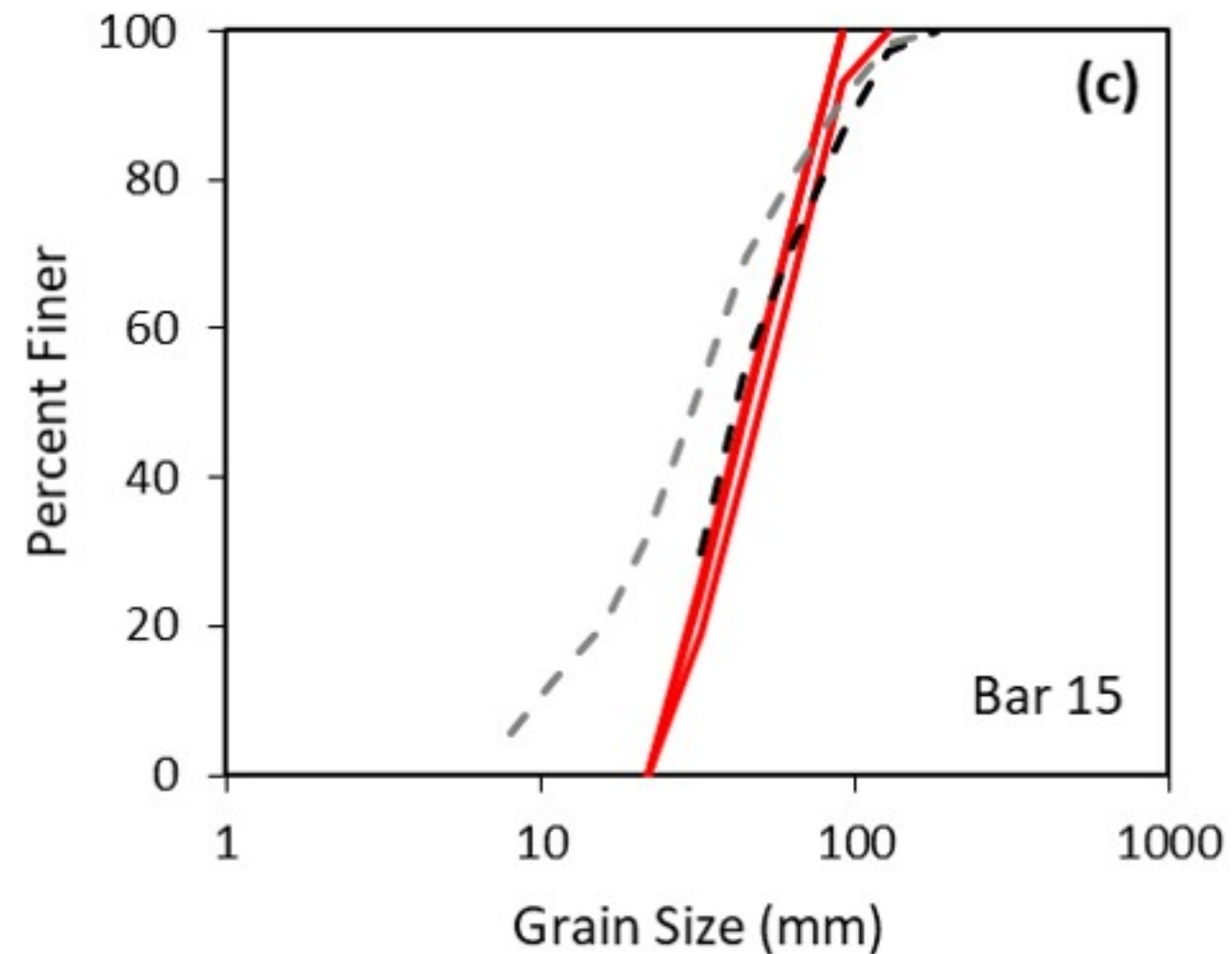
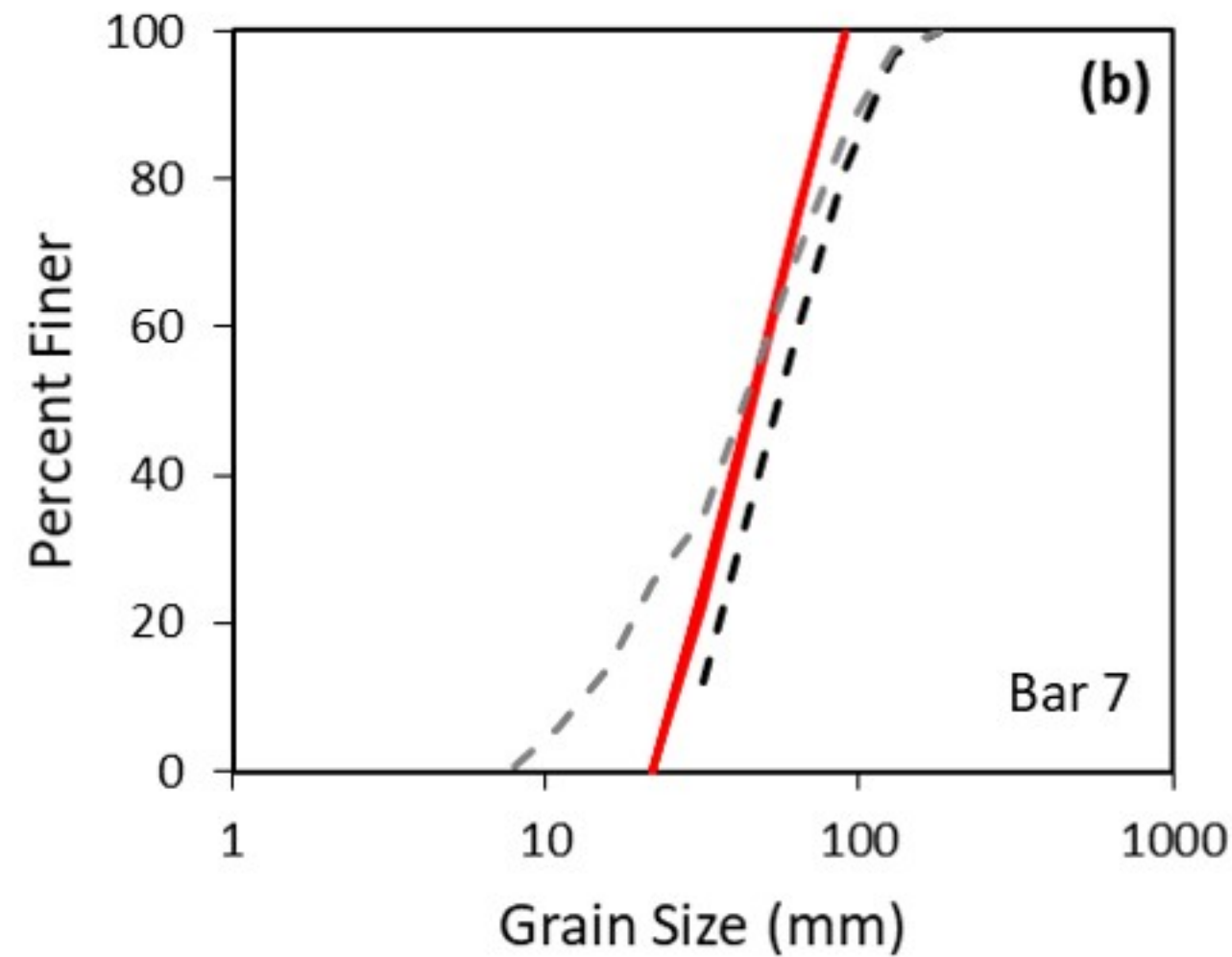
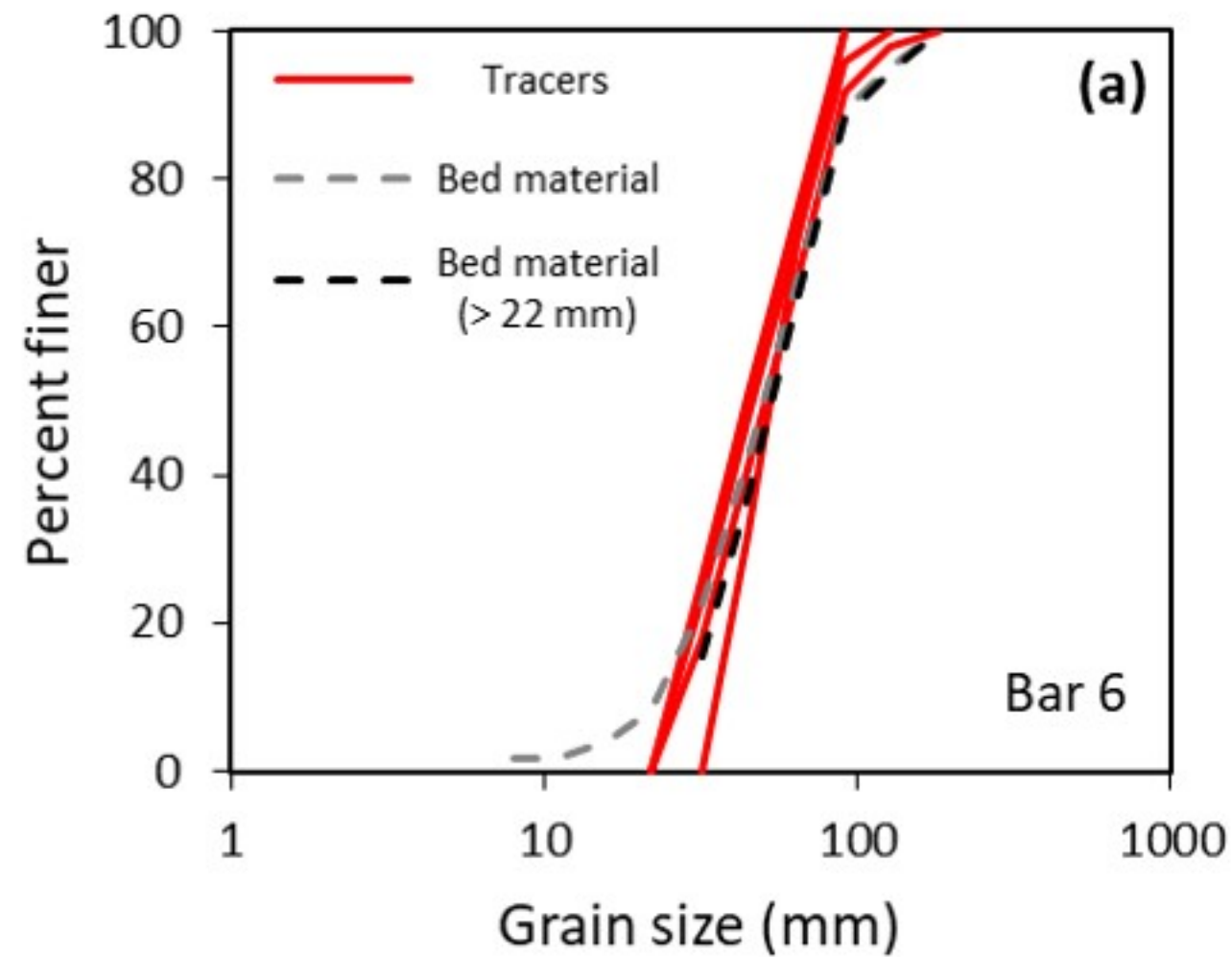


Figure 4.

(a)



(b)



Figure 5.



Figure 6.

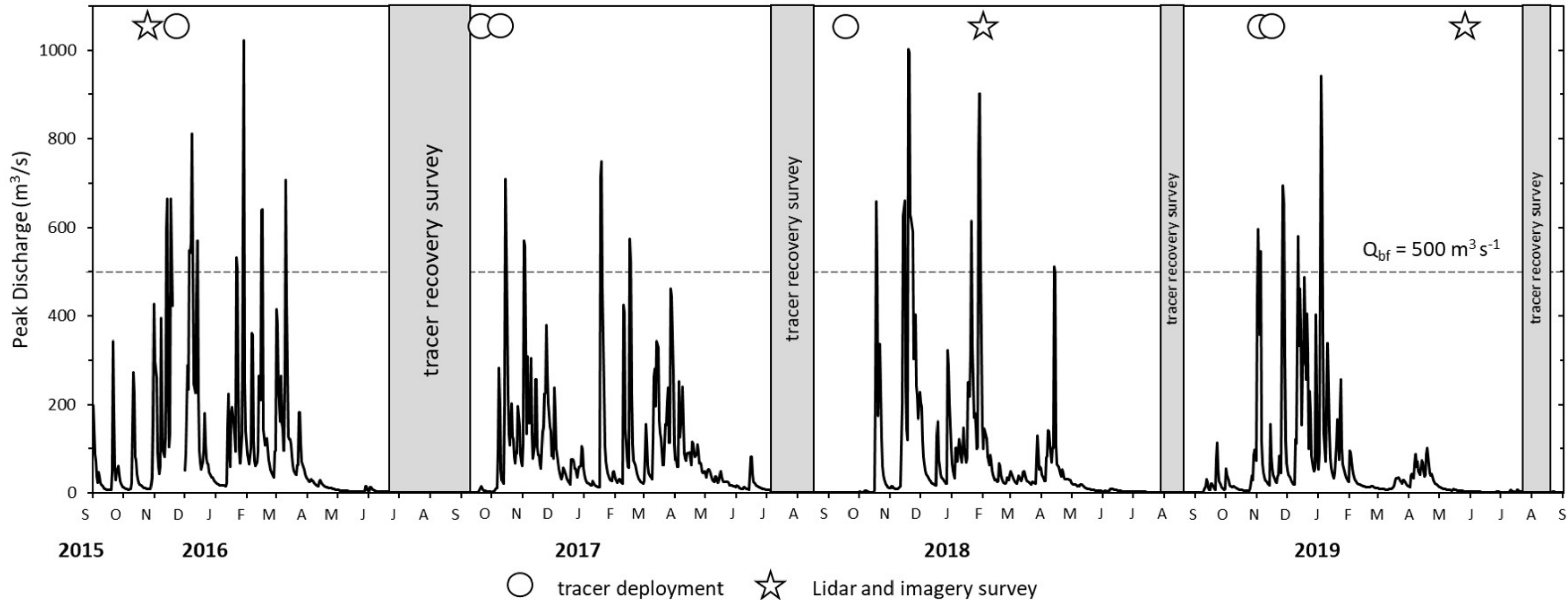


Figure 7.

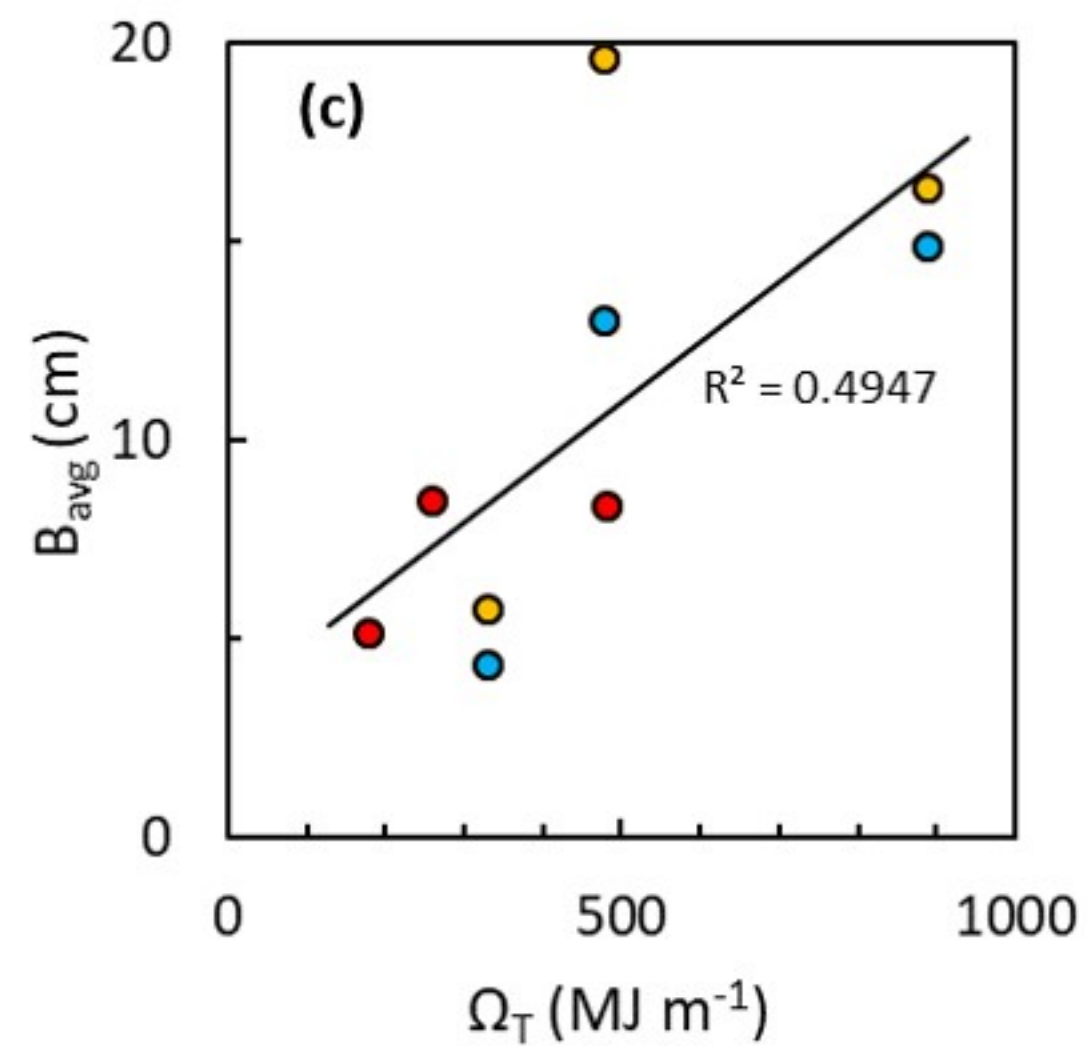
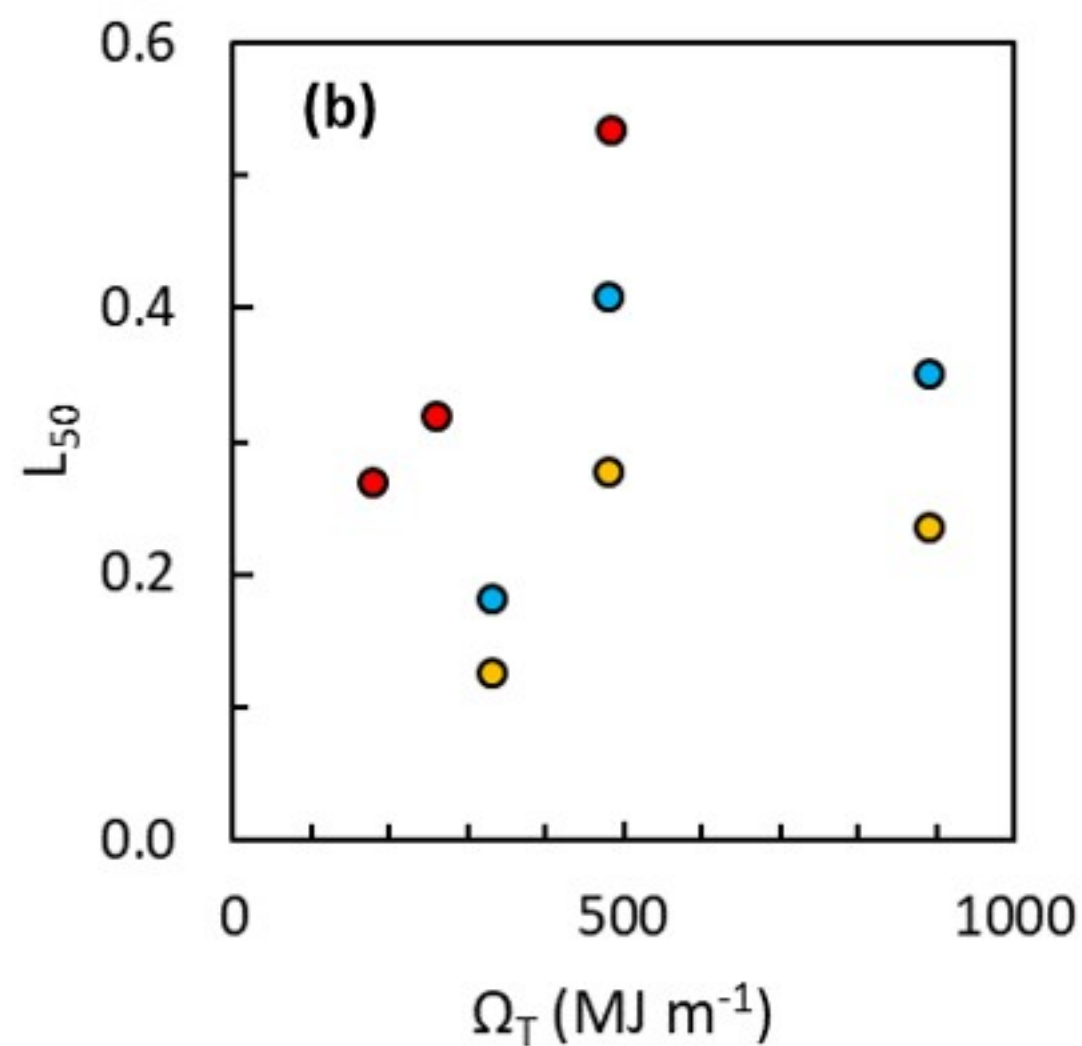
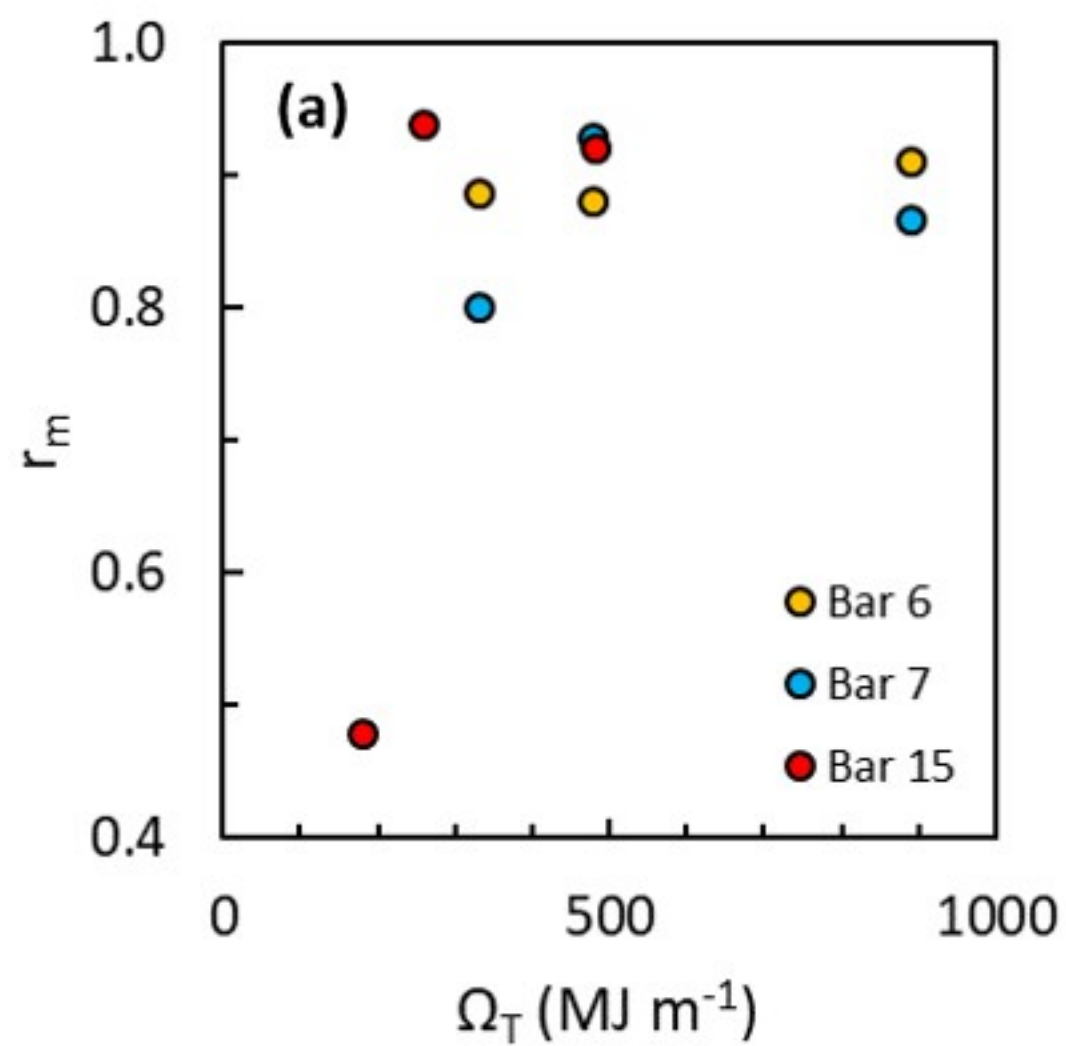


Figure 8.

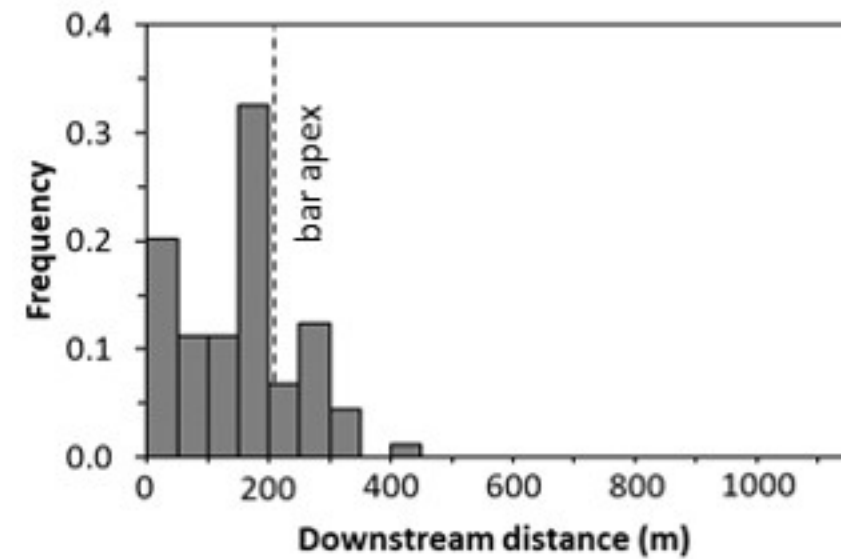
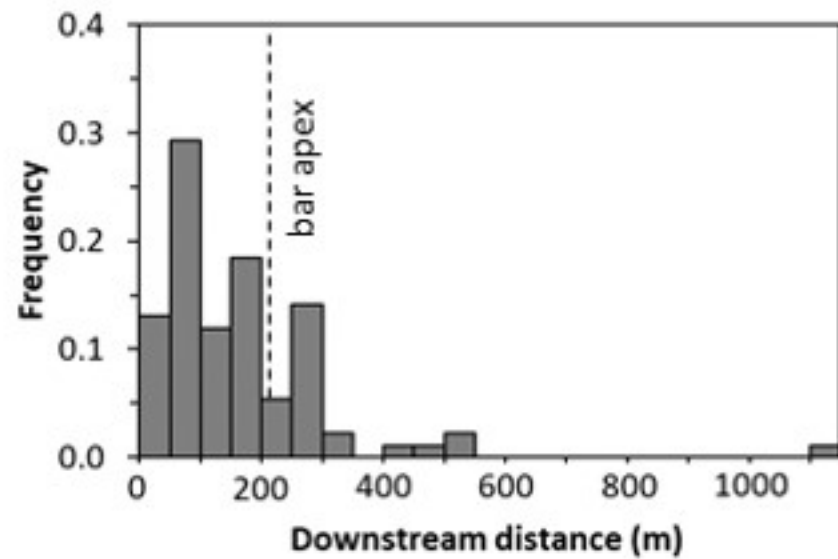
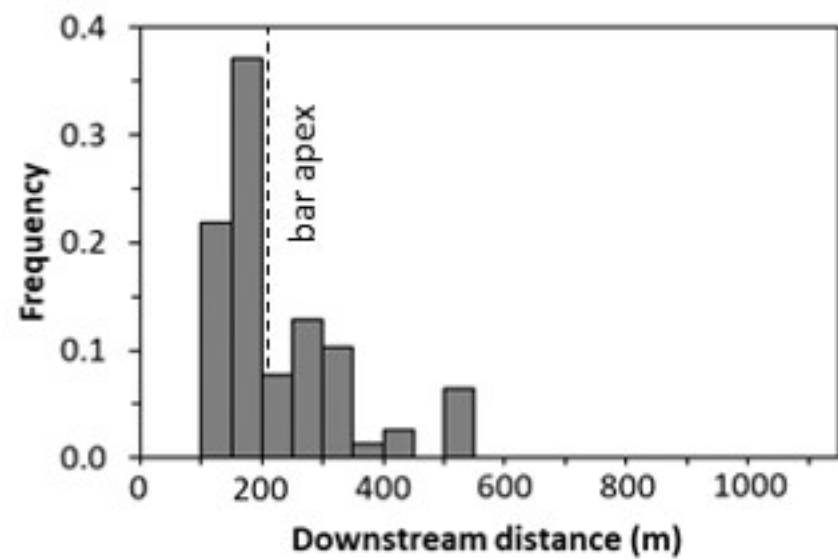
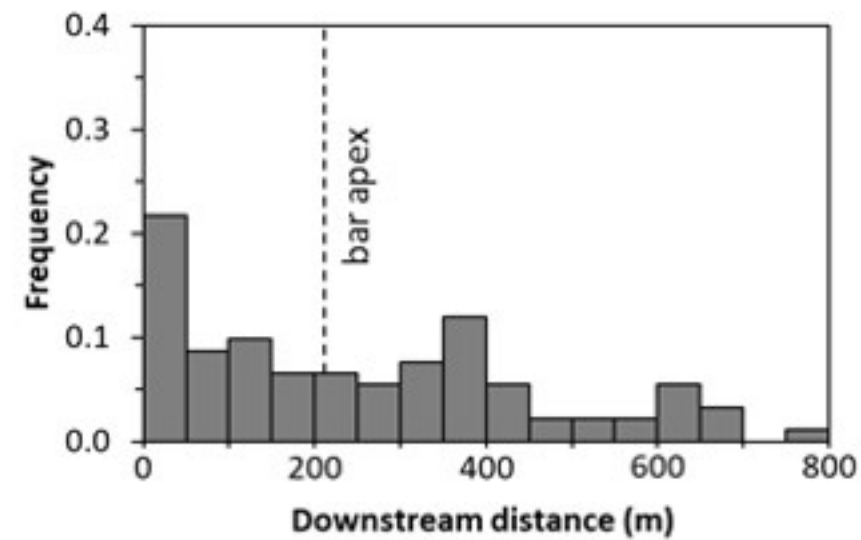
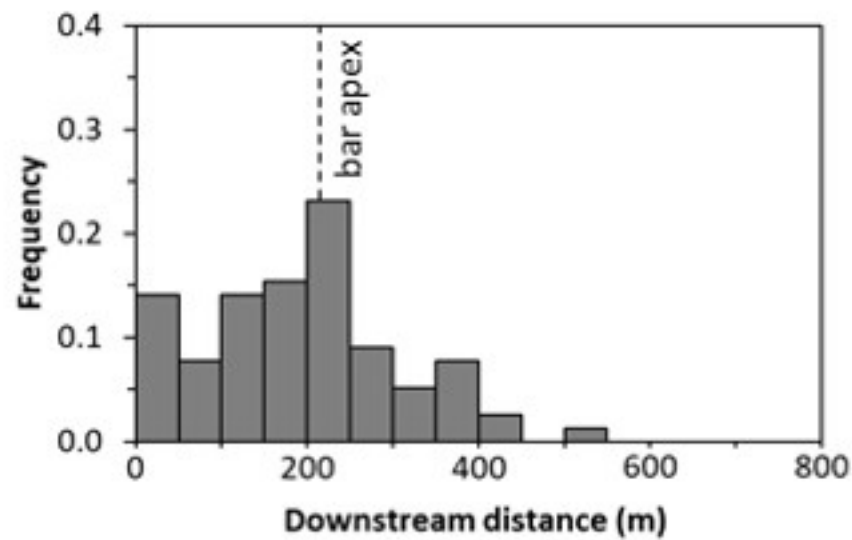
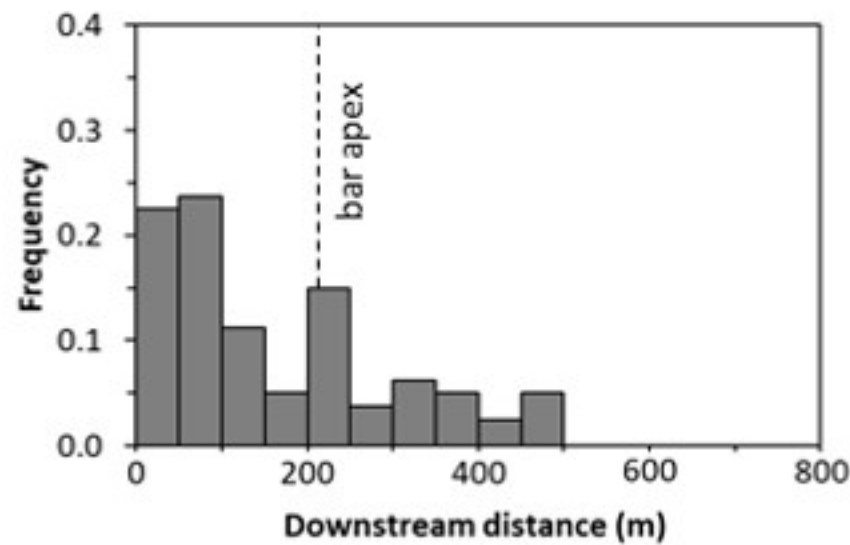
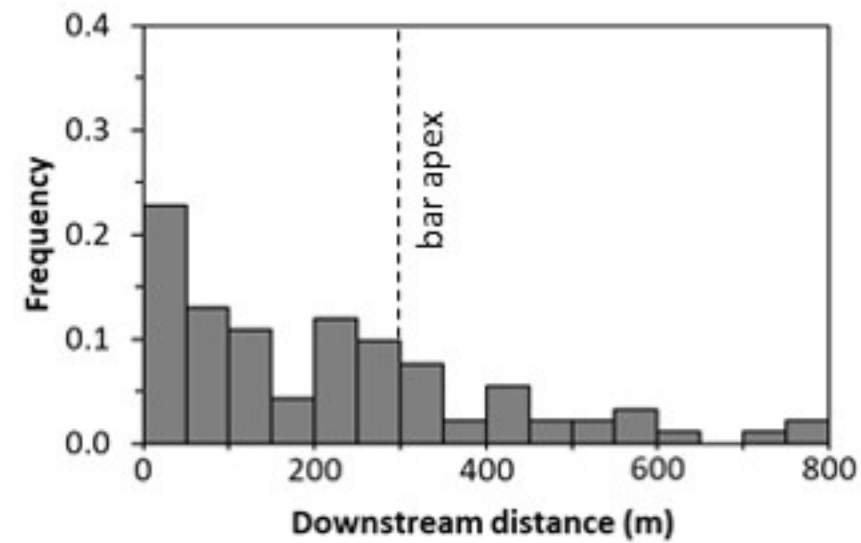
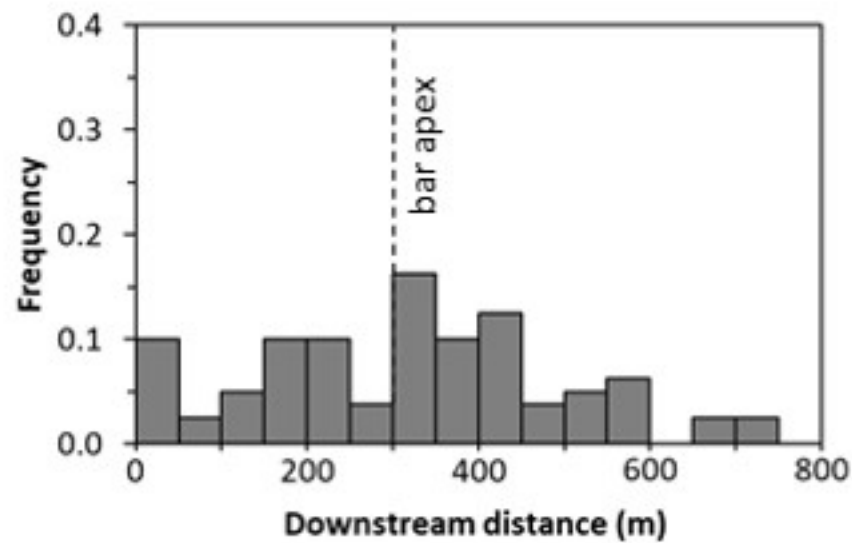
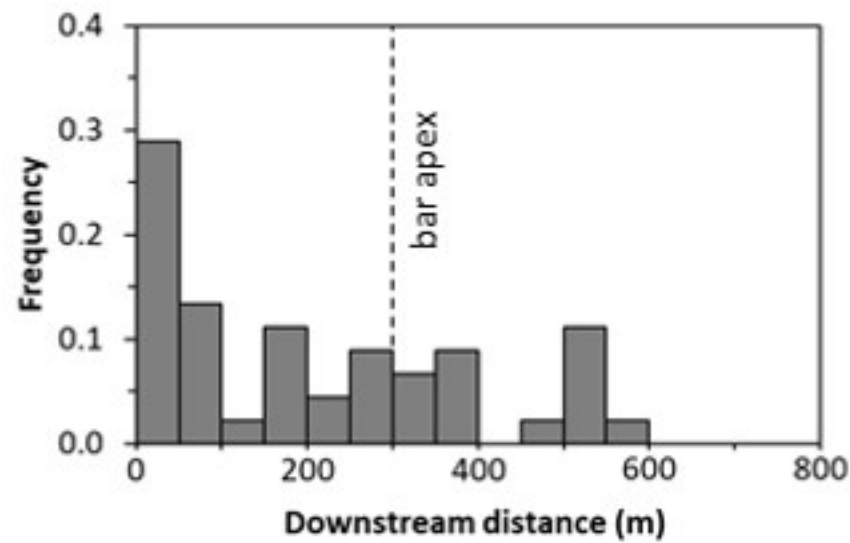
2016-17**2017-18****2018-19****(a)****Bar 6****(b)****Bar 7****(c)****Bar 15**

Figure 9.

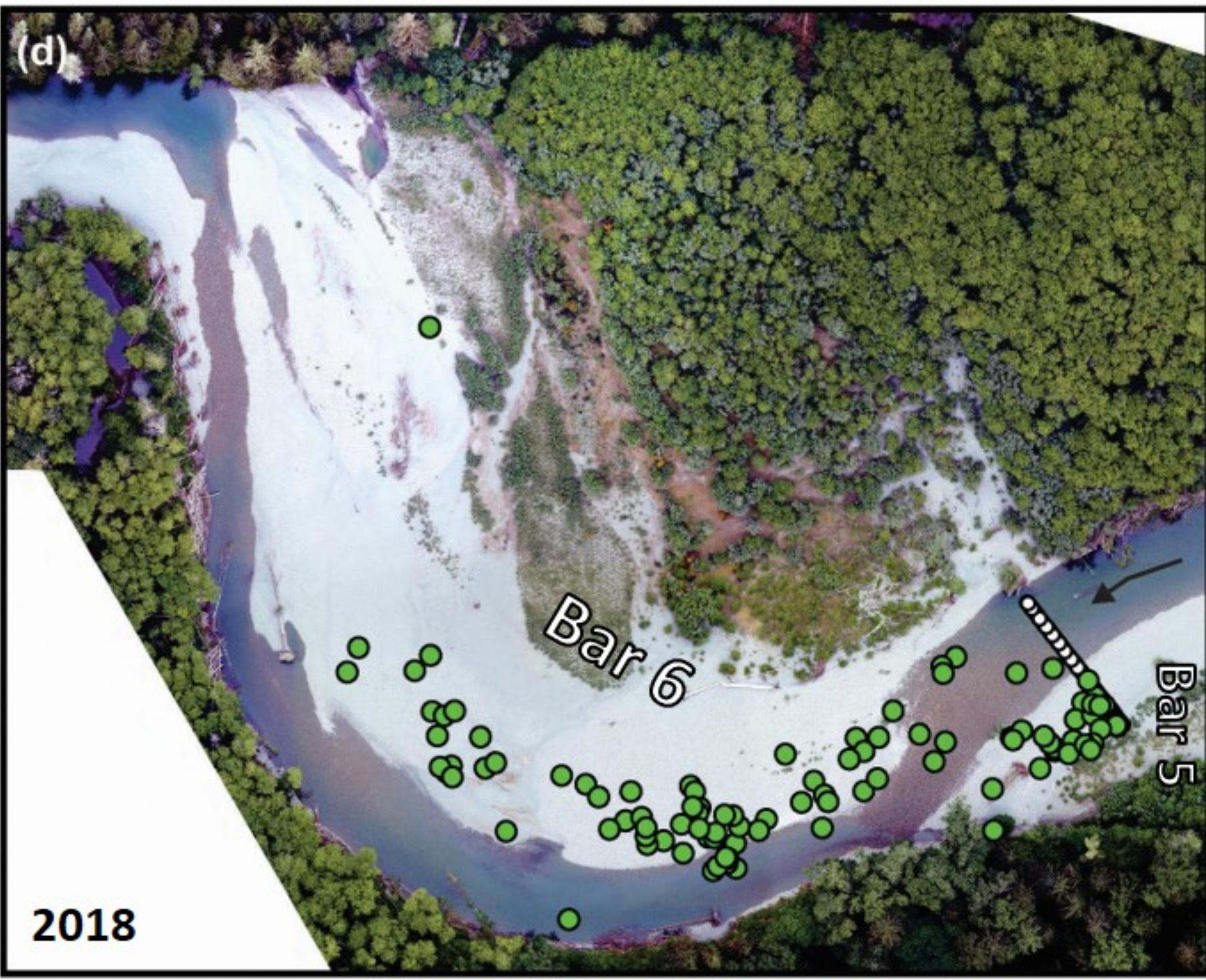
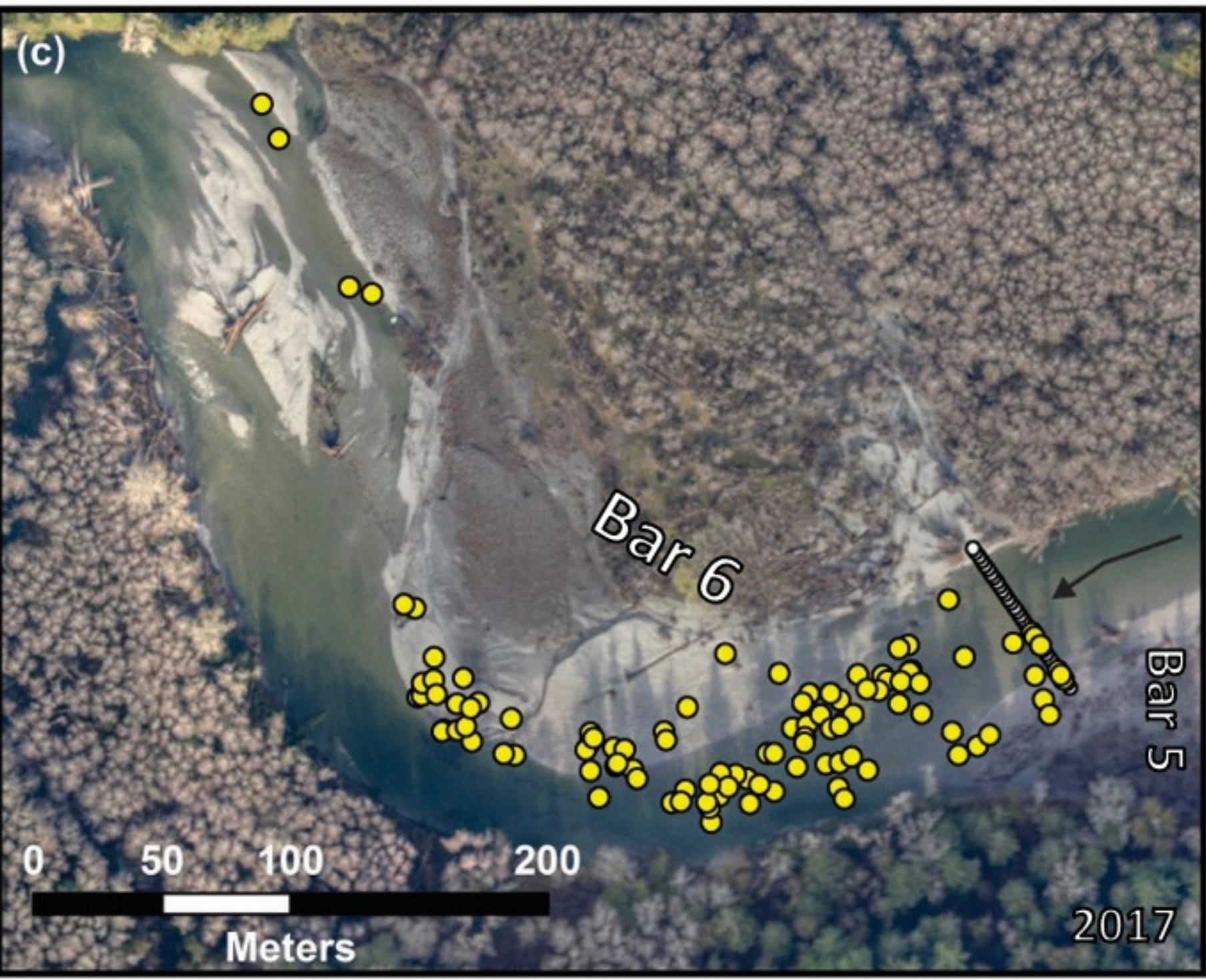
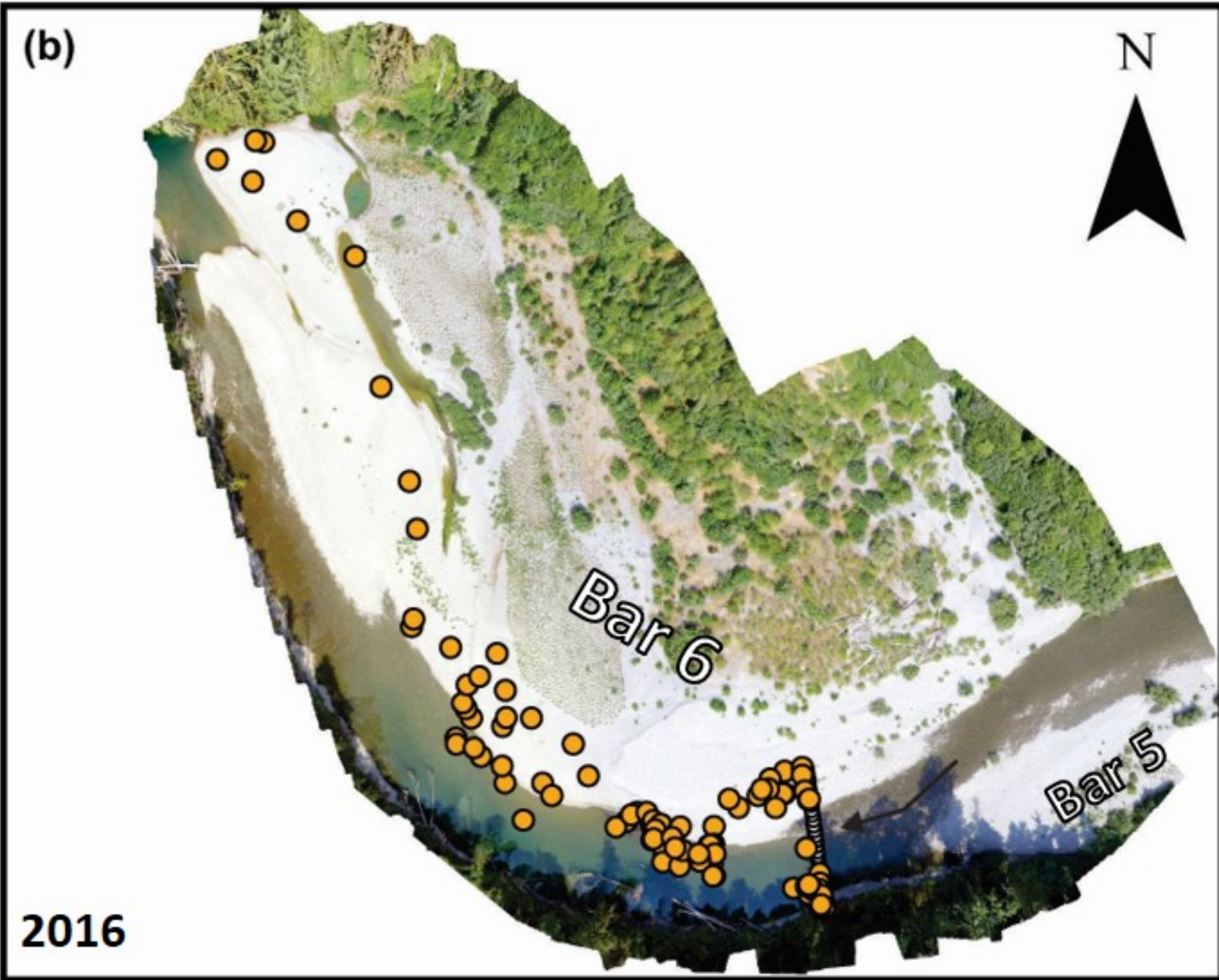
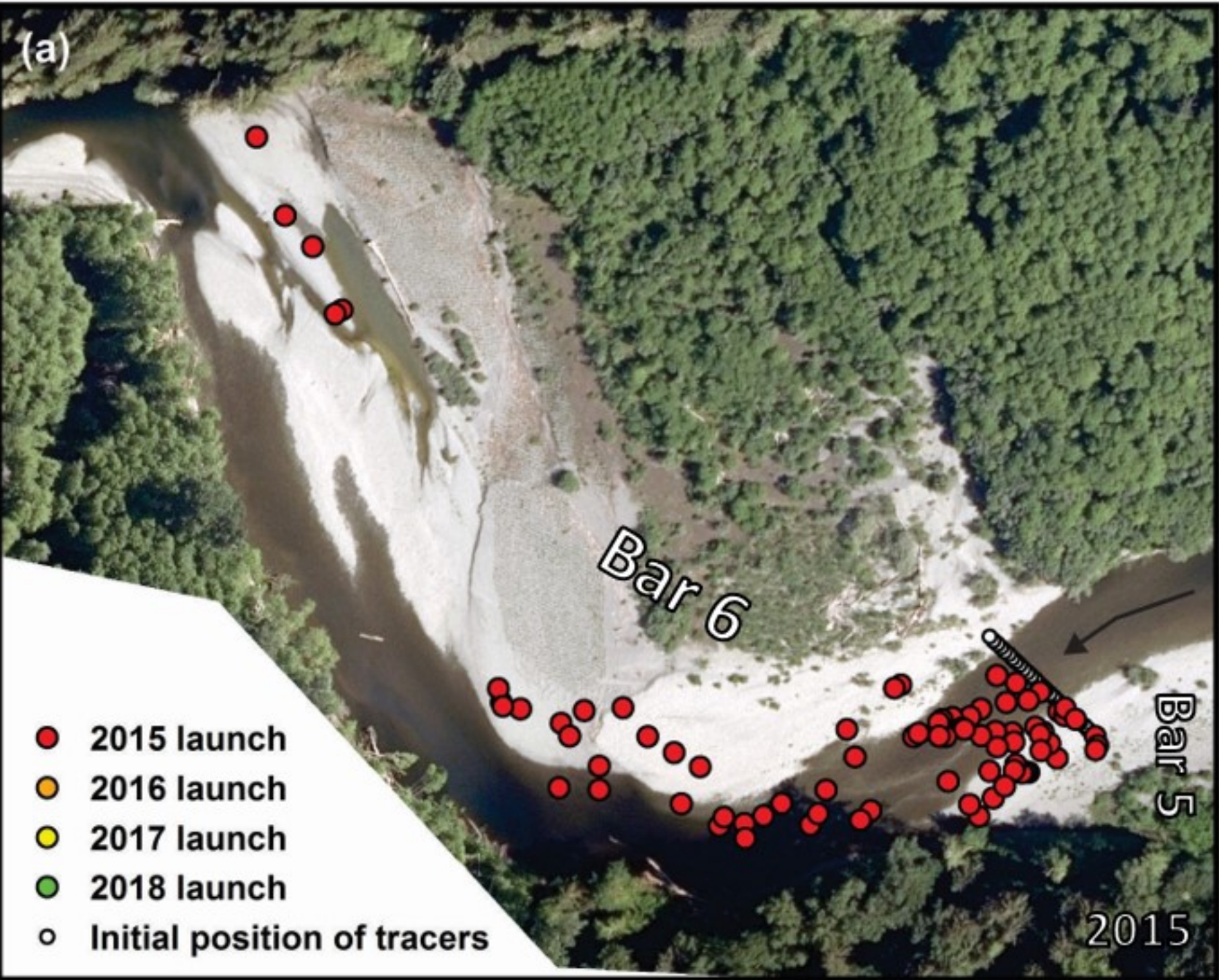


Figure 10.

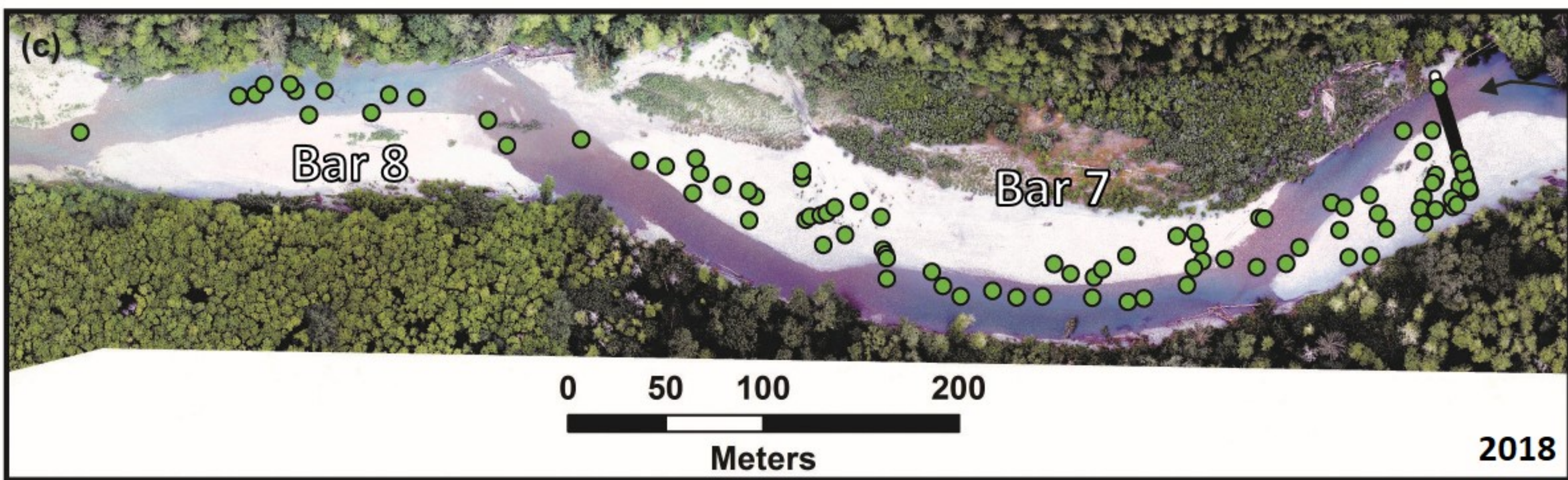


Figure 11.

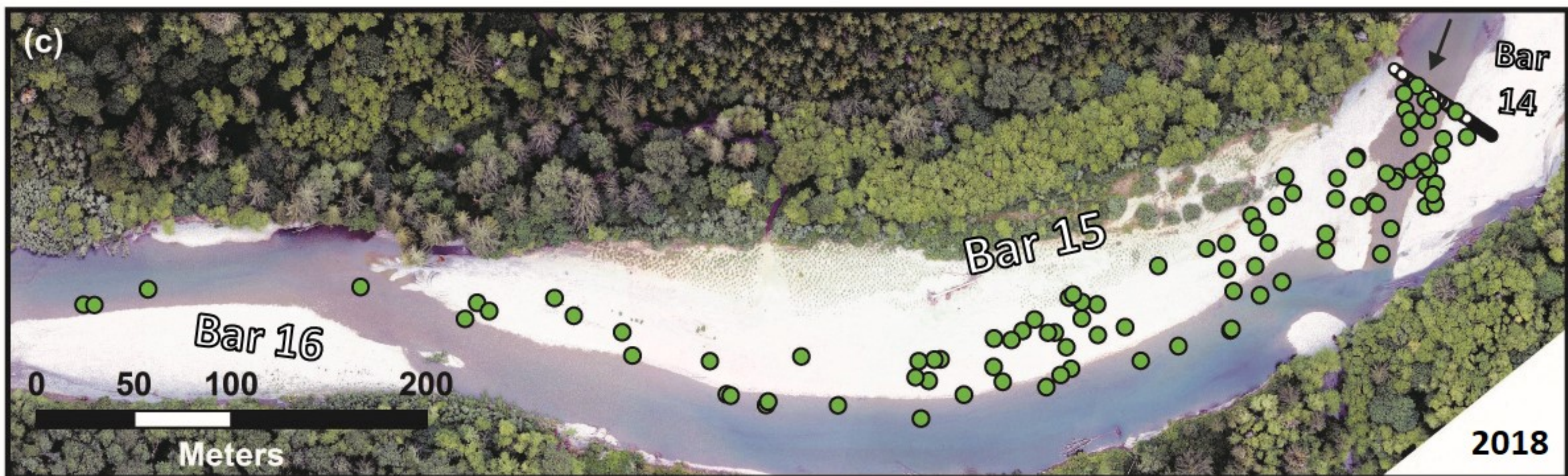
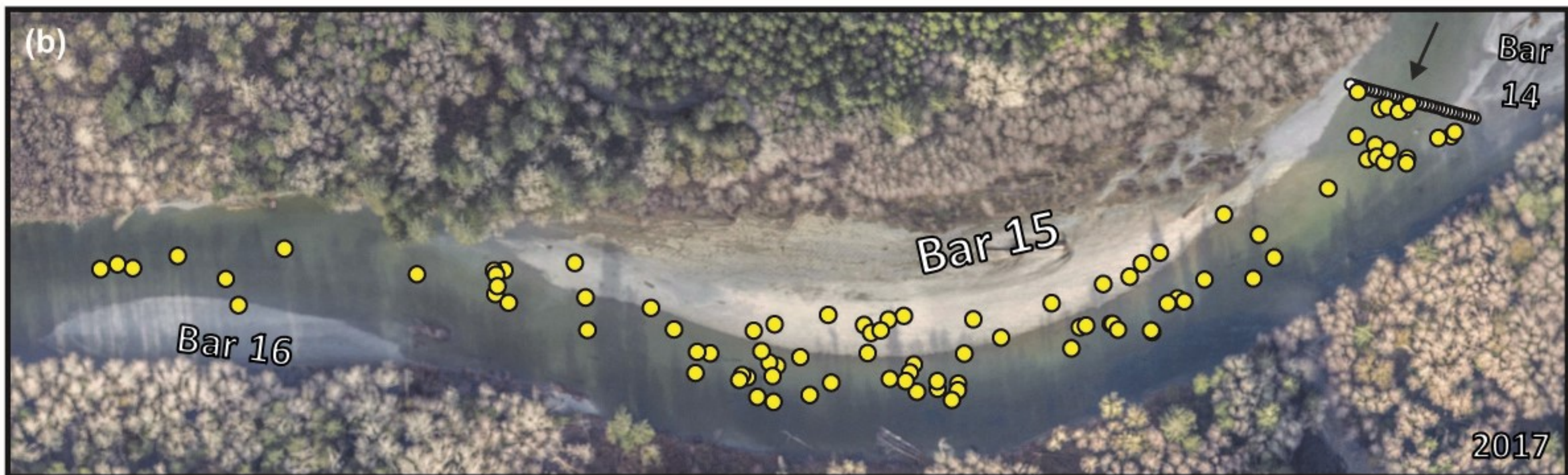
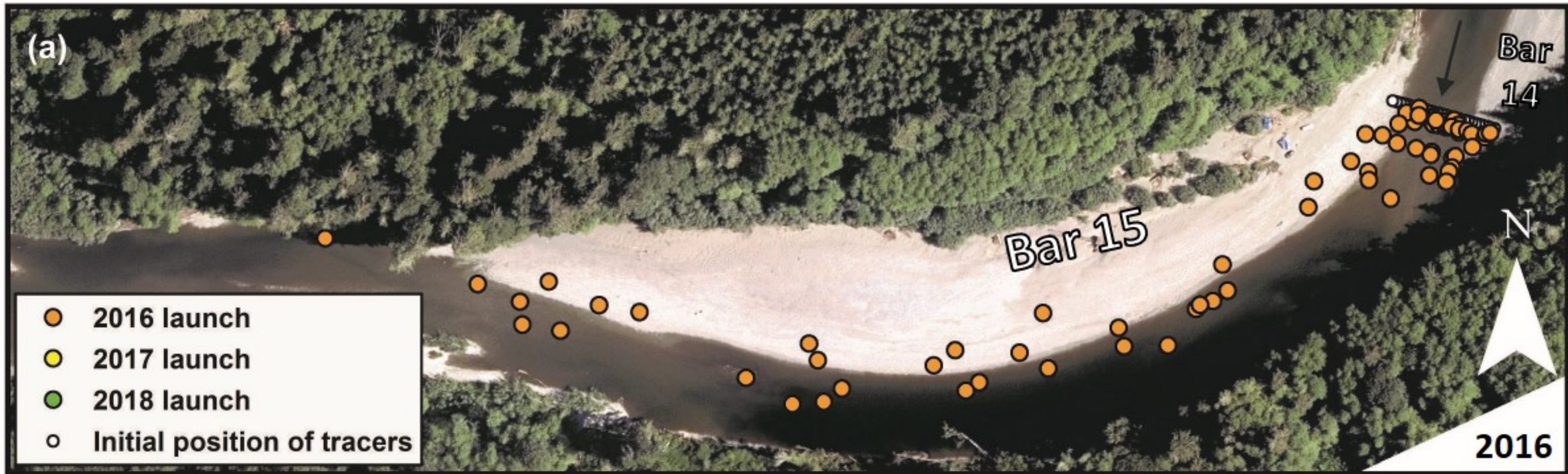


Figure 12.

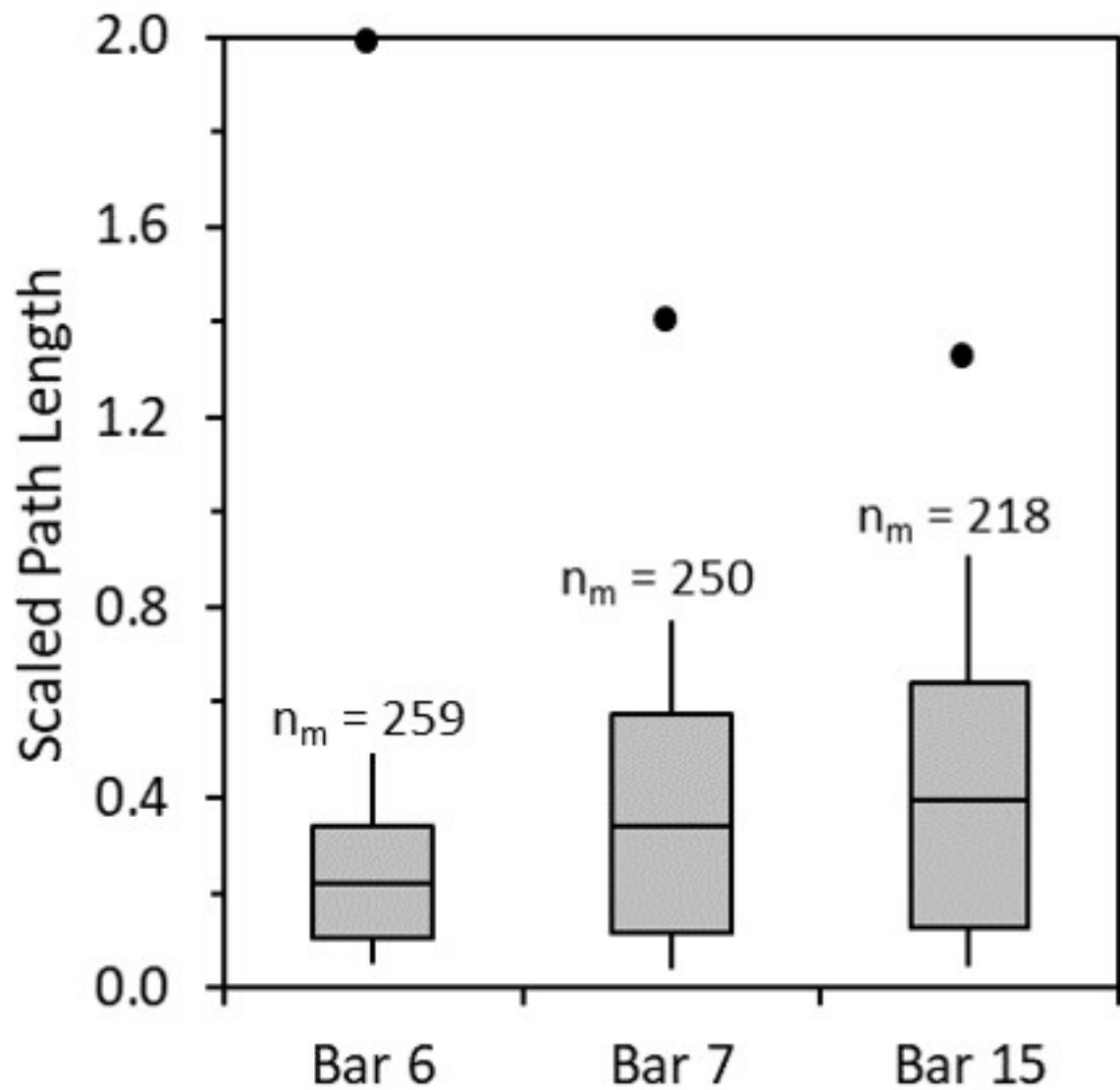


Figure 13.

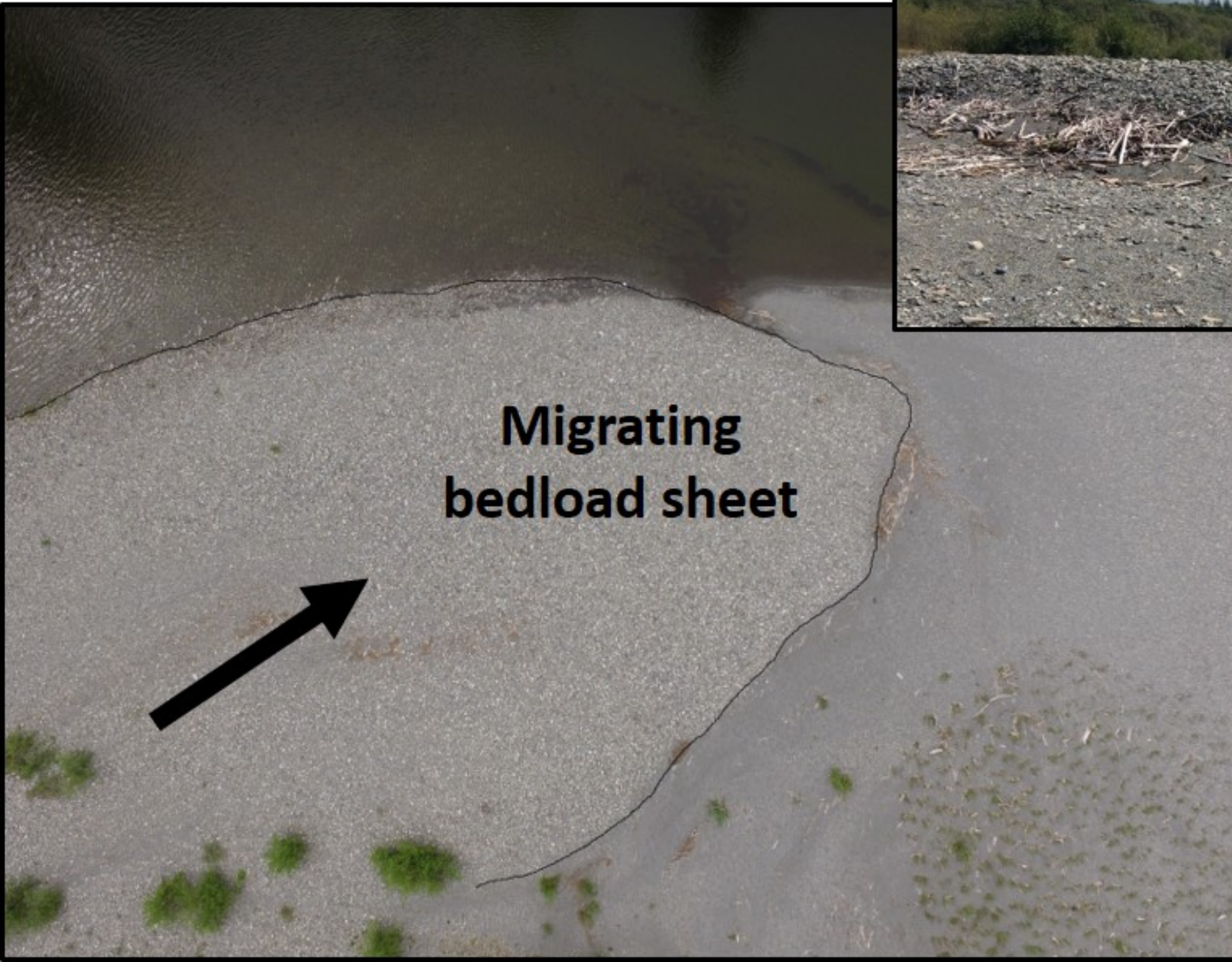


Figure 14.

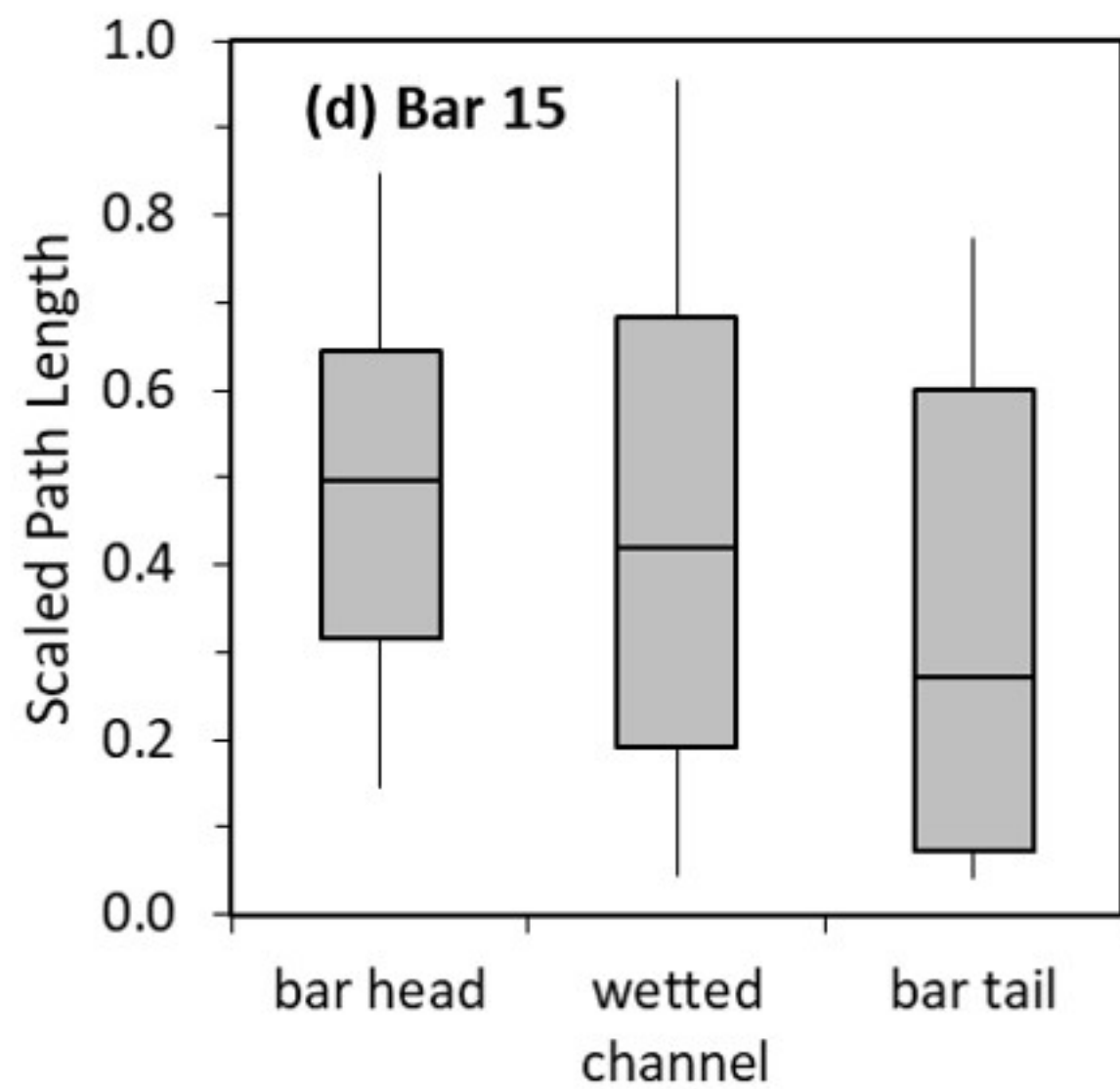
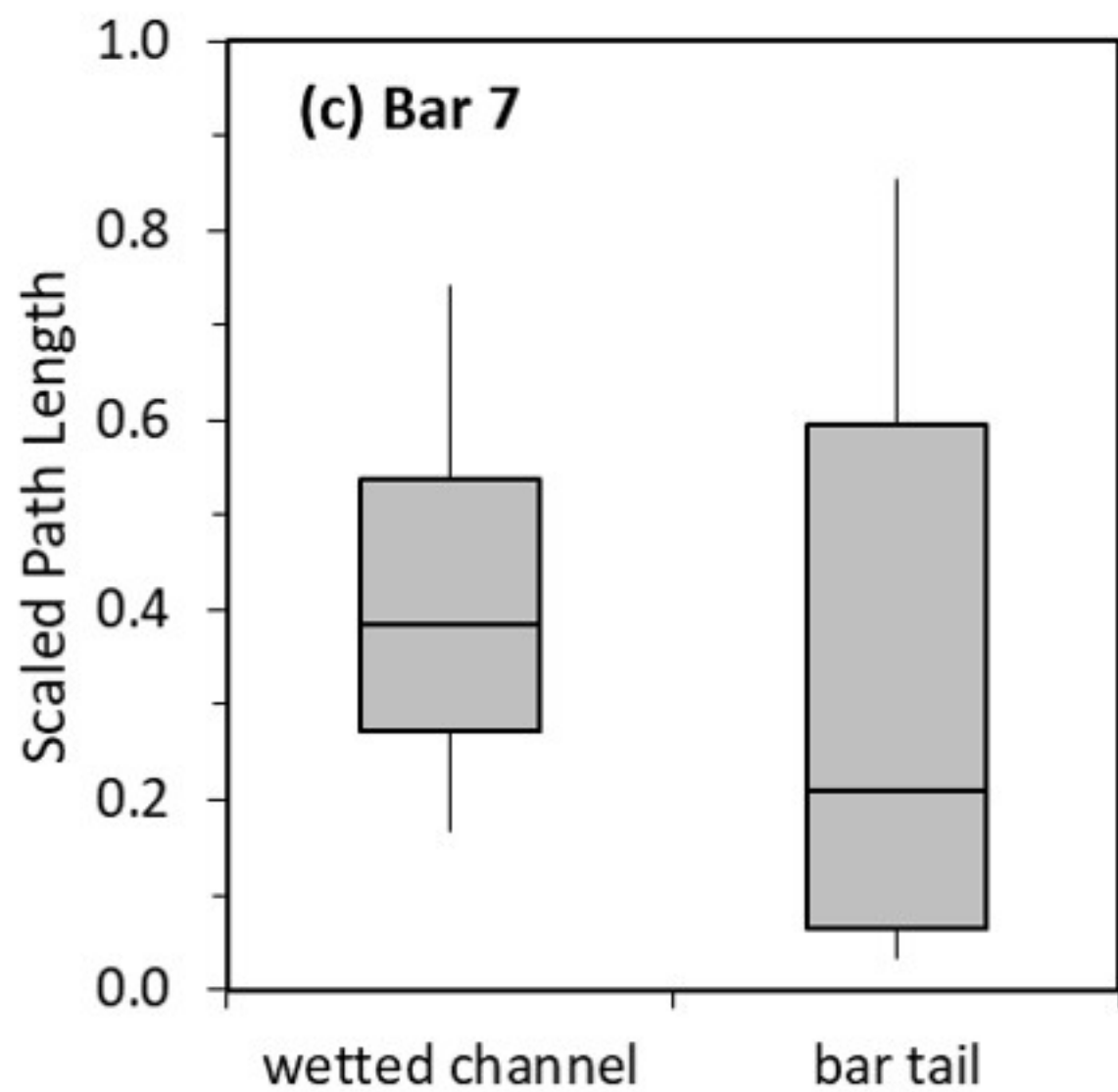
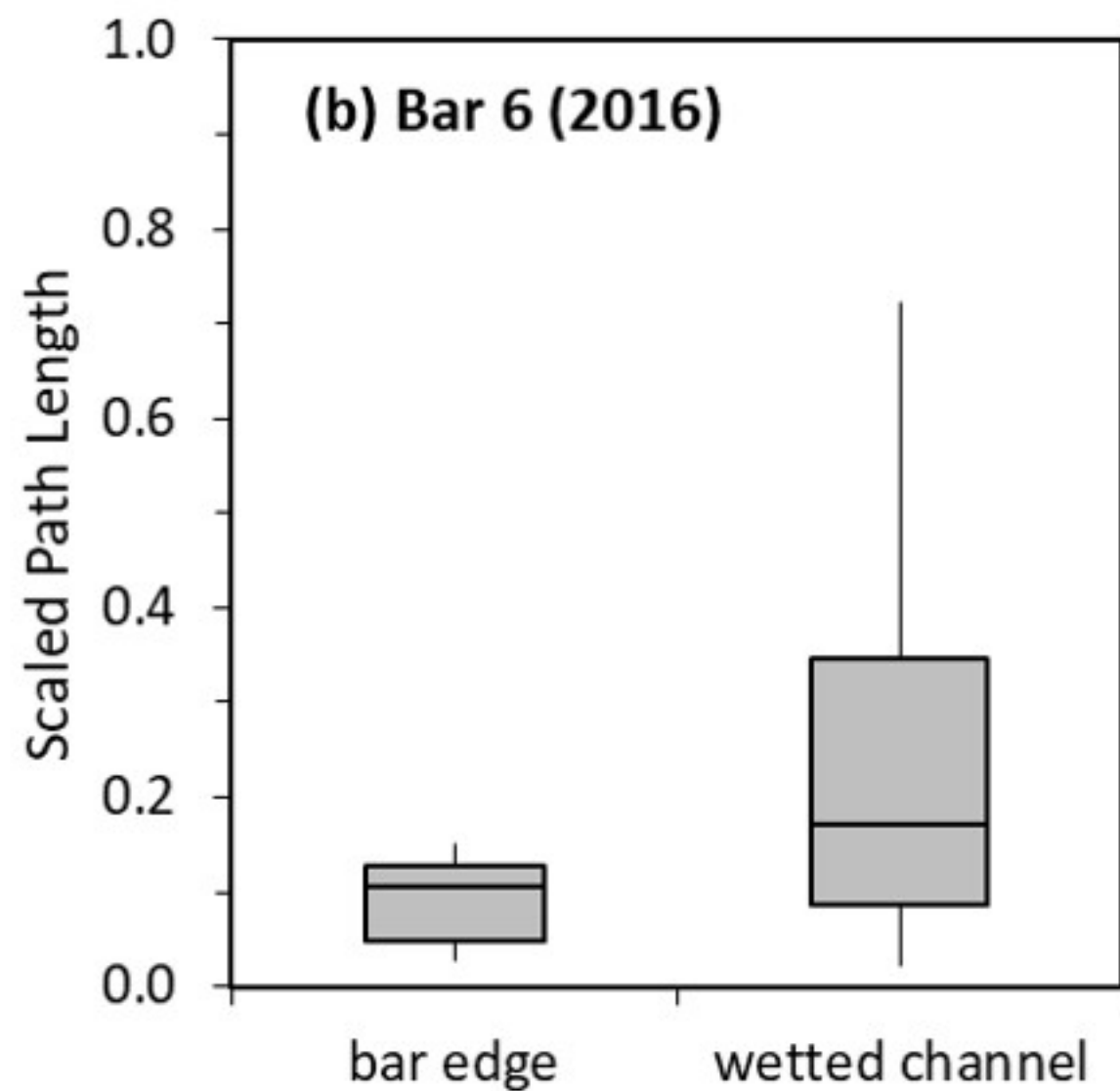
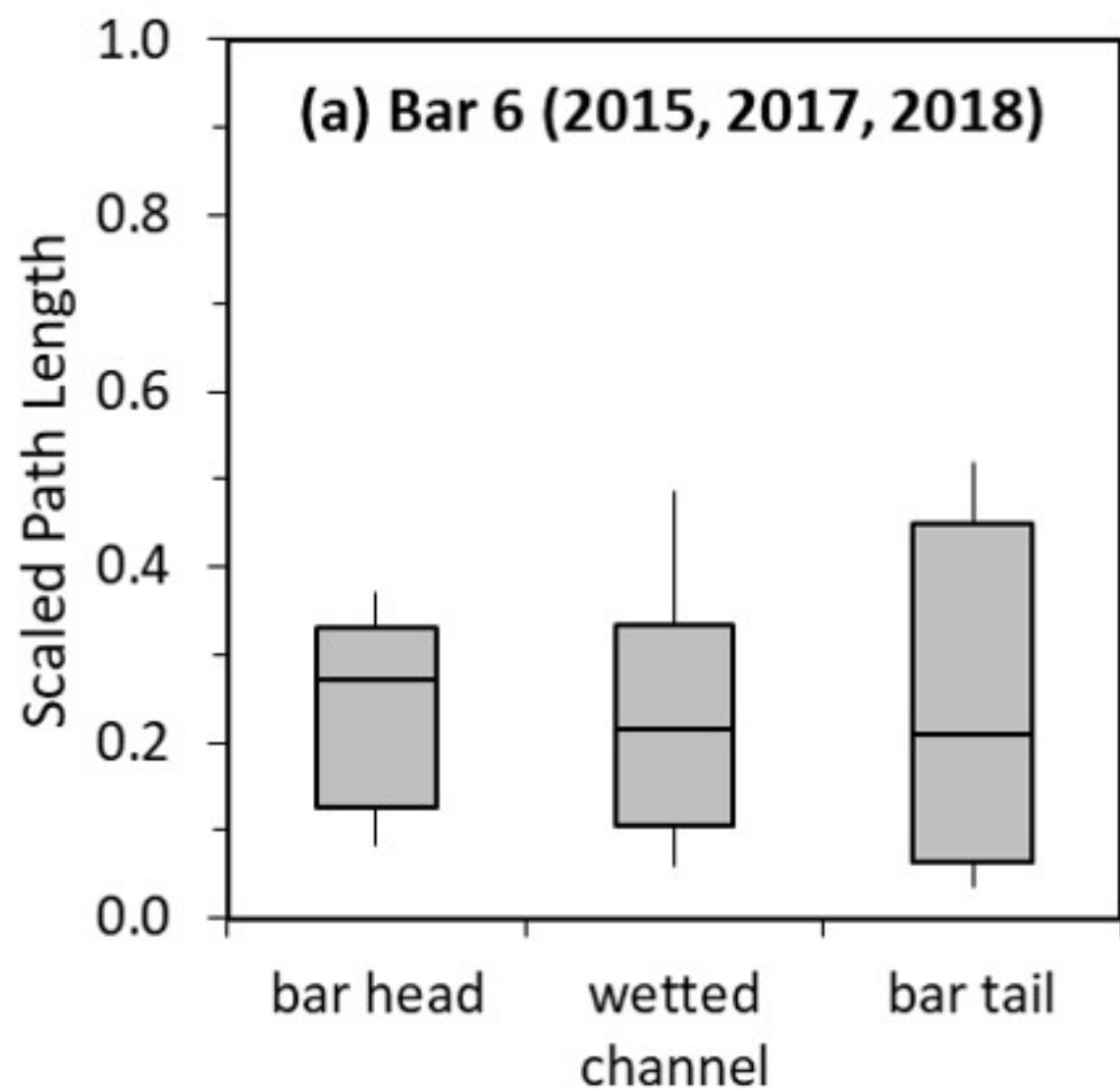
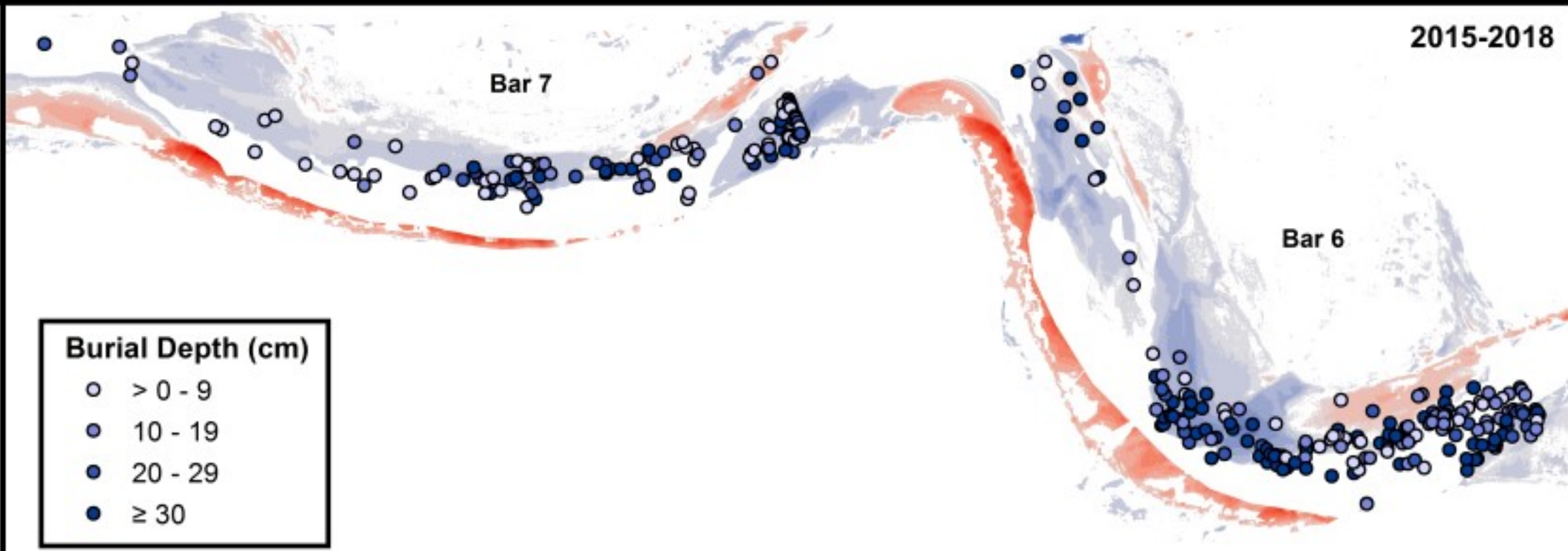
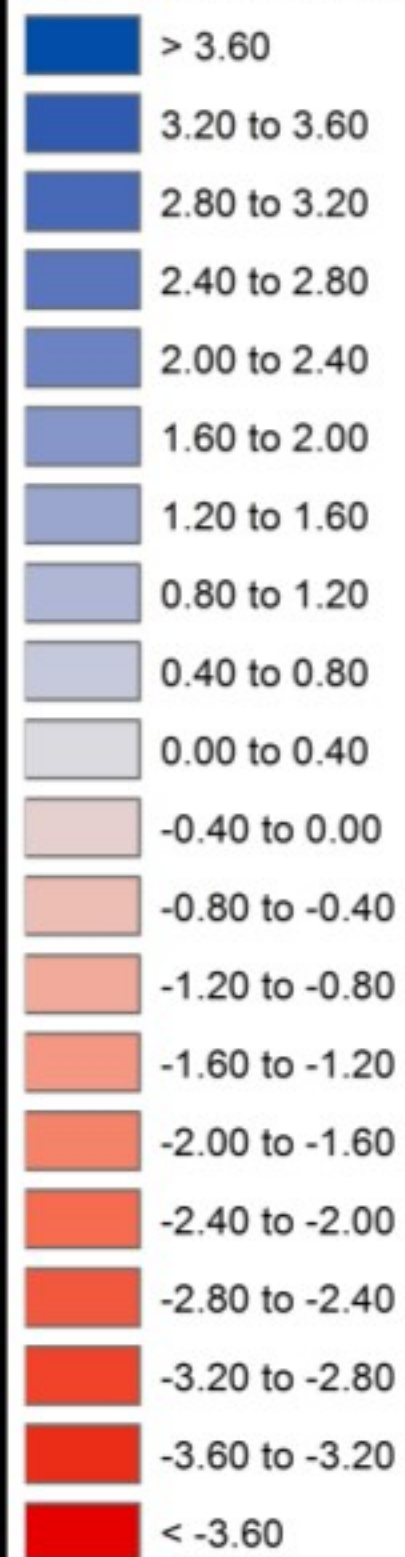
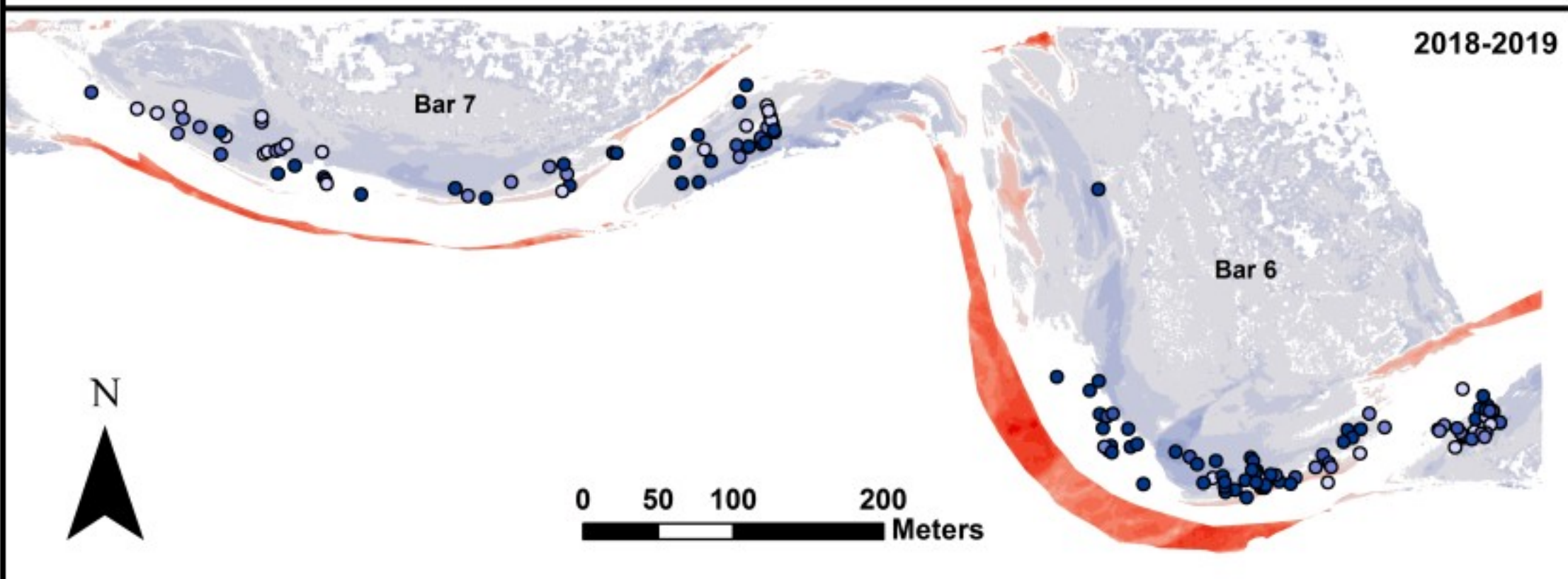


Figure 15.

Elevation Difference (m)



2015-2018



2018-2019

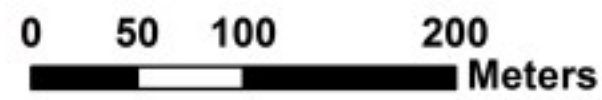
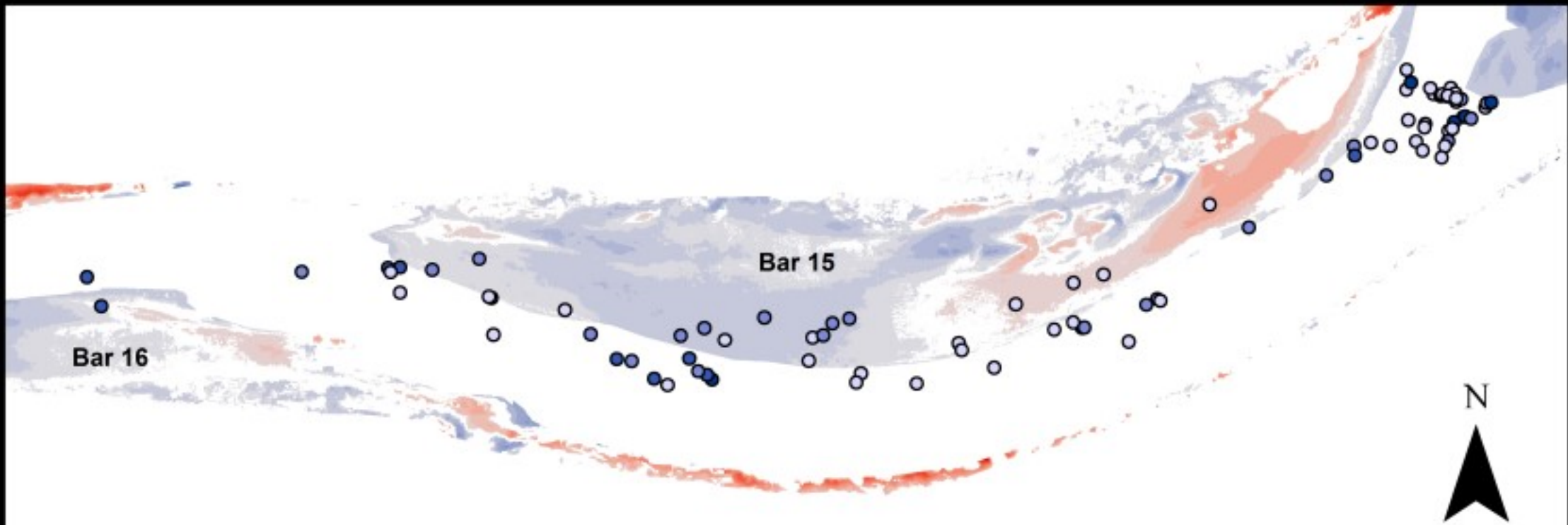


Figure 16.



2015-2018

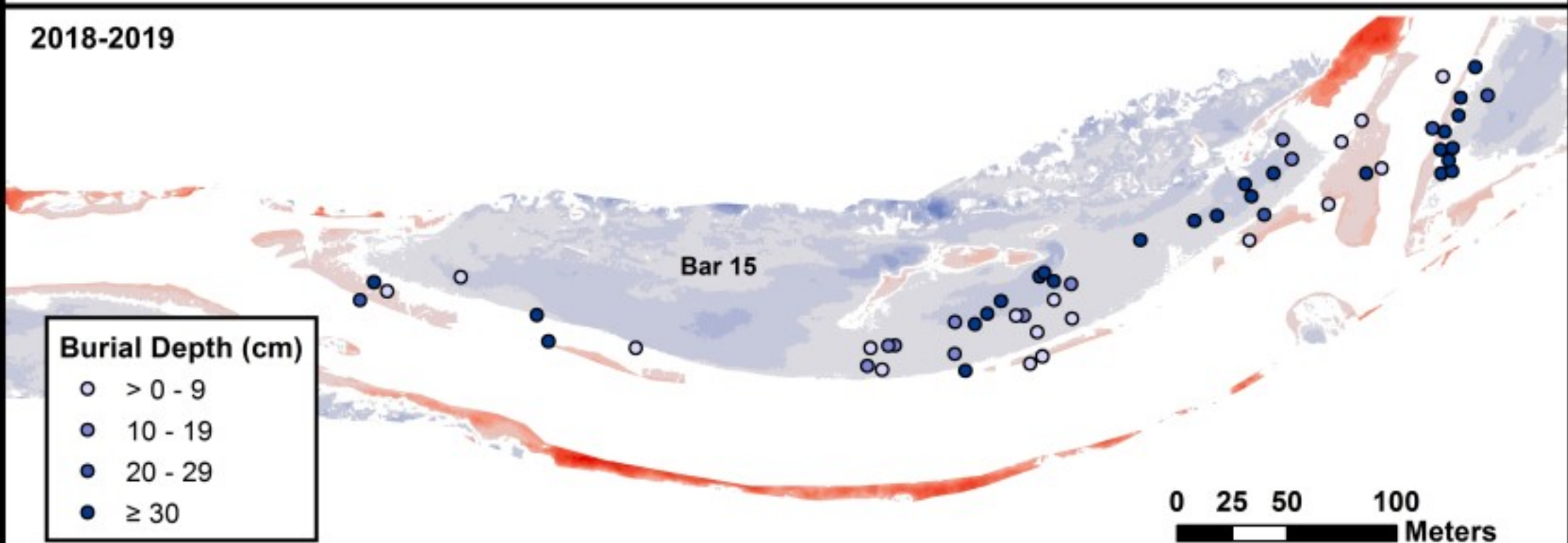
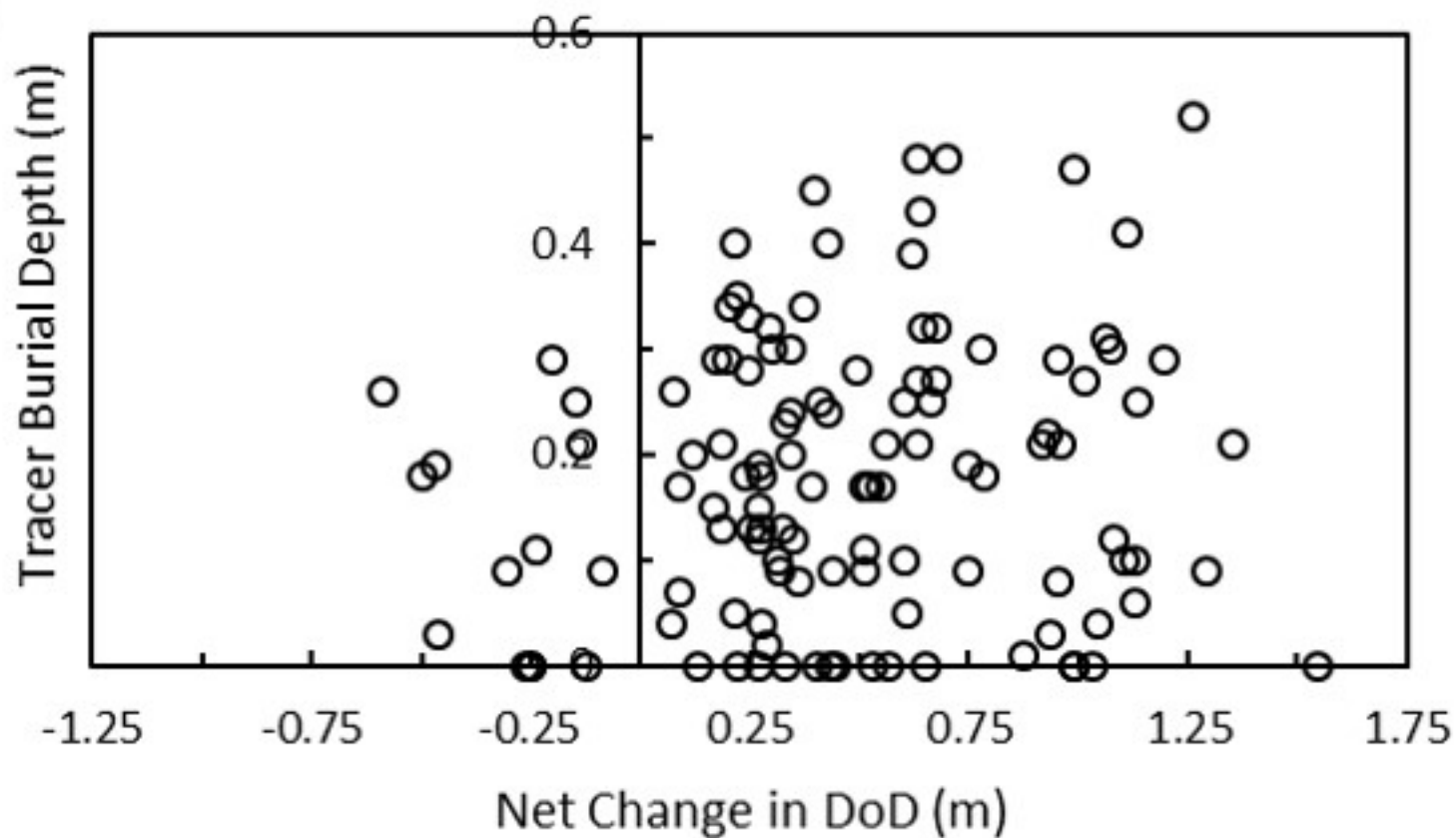
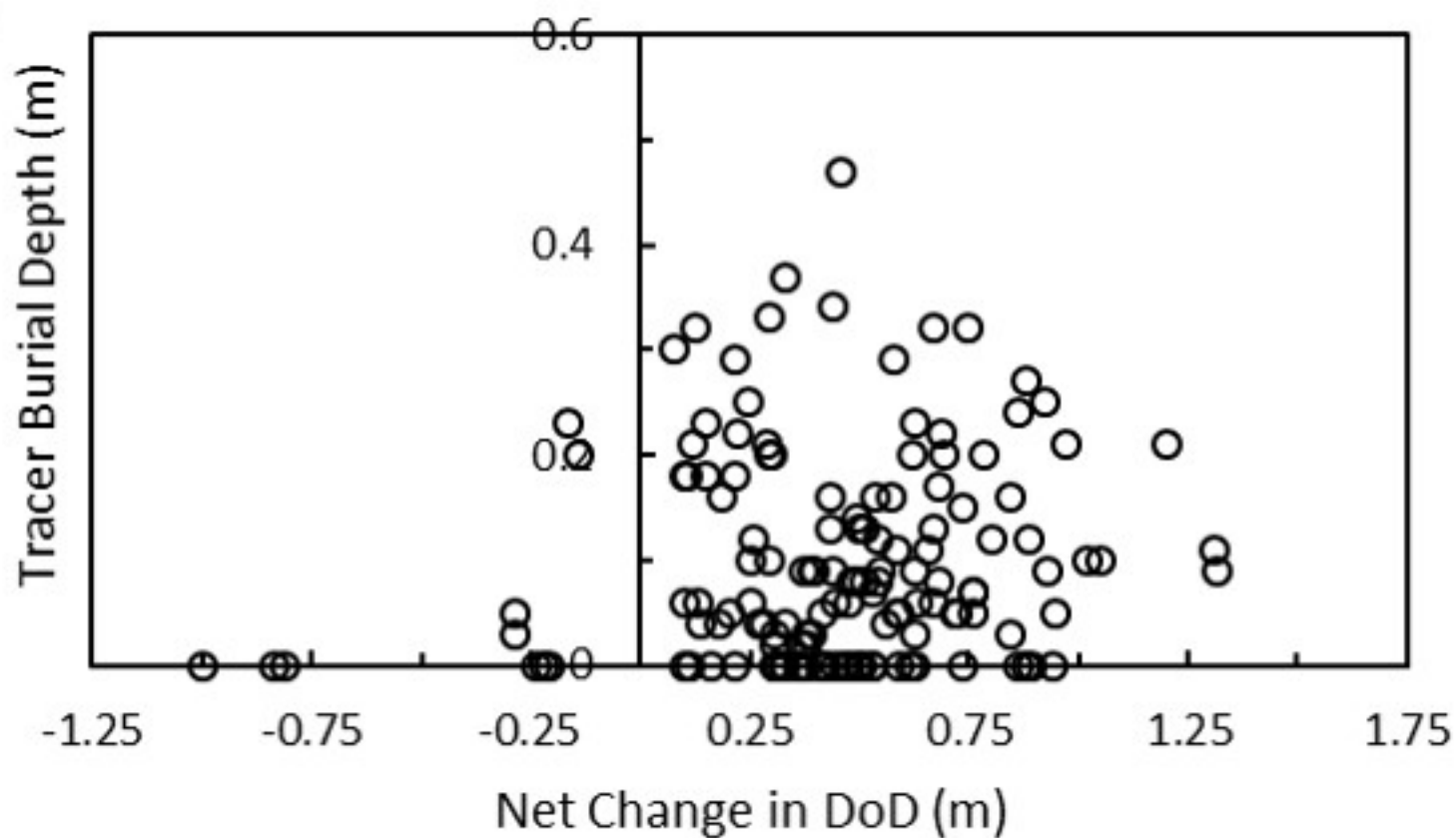


Figure 17.

(a) Bar 6



(b) Bar 7



(b) Bar 15

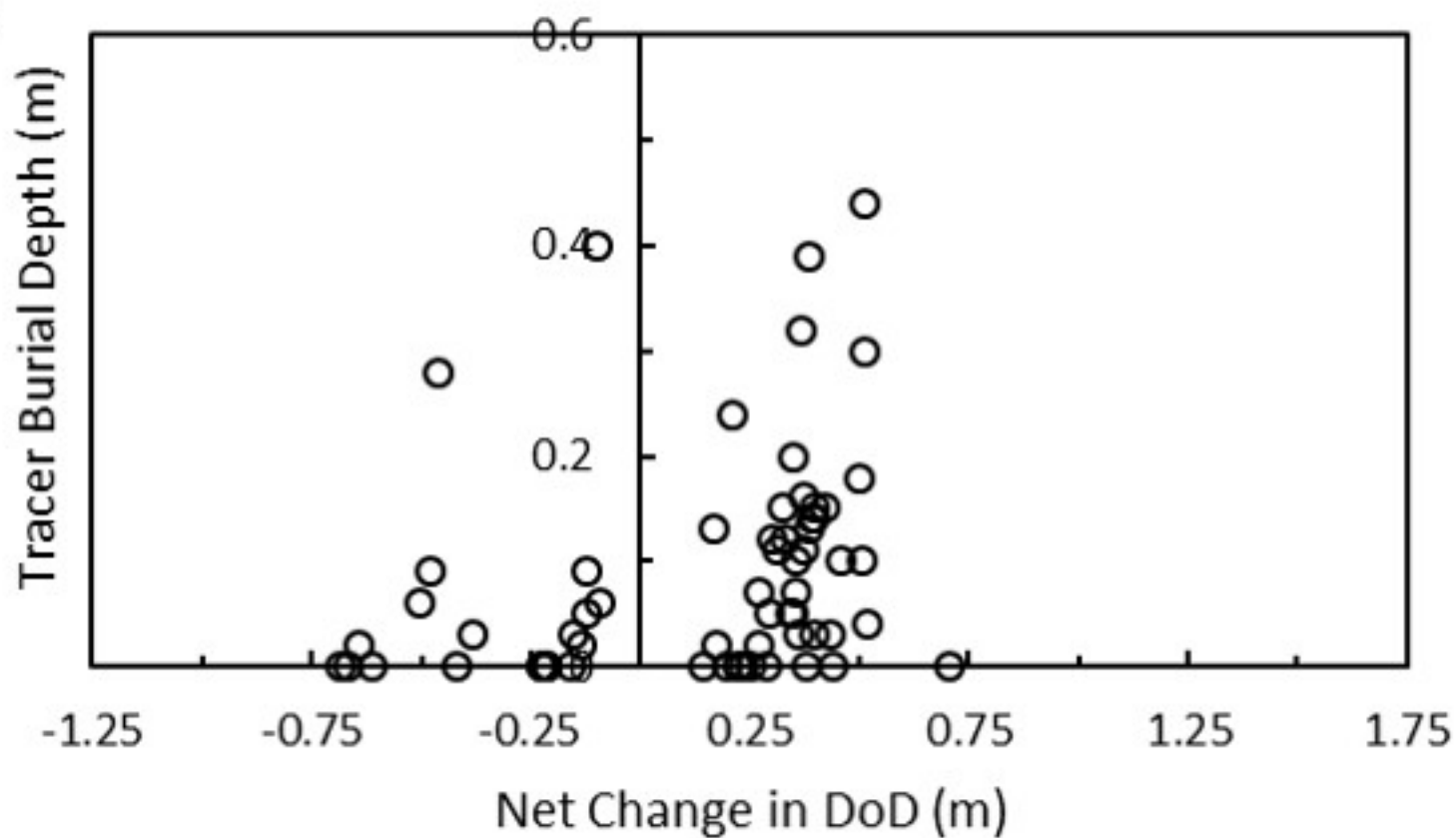


Figure 18.

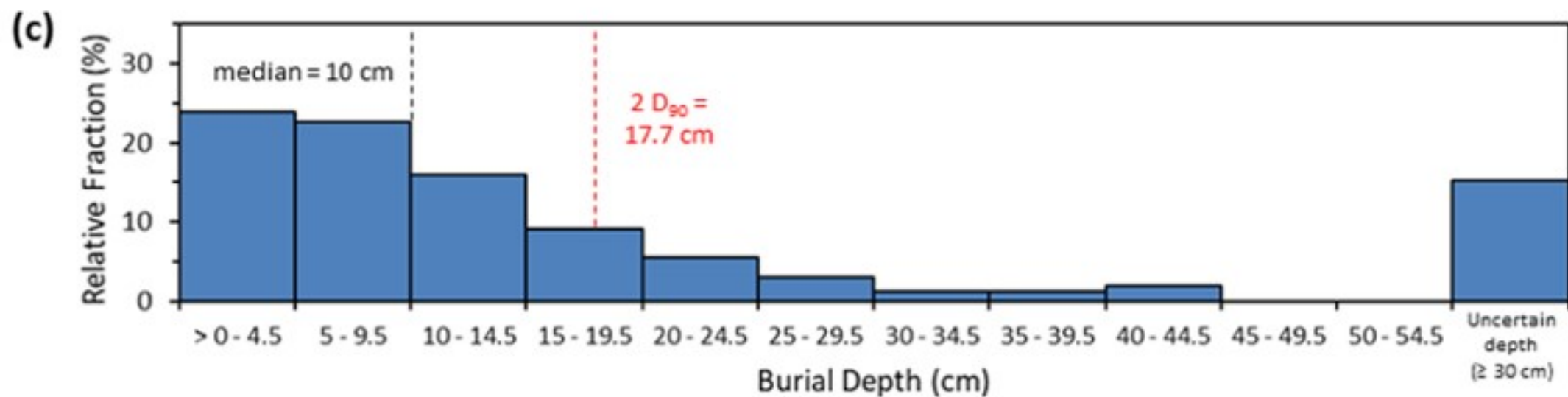
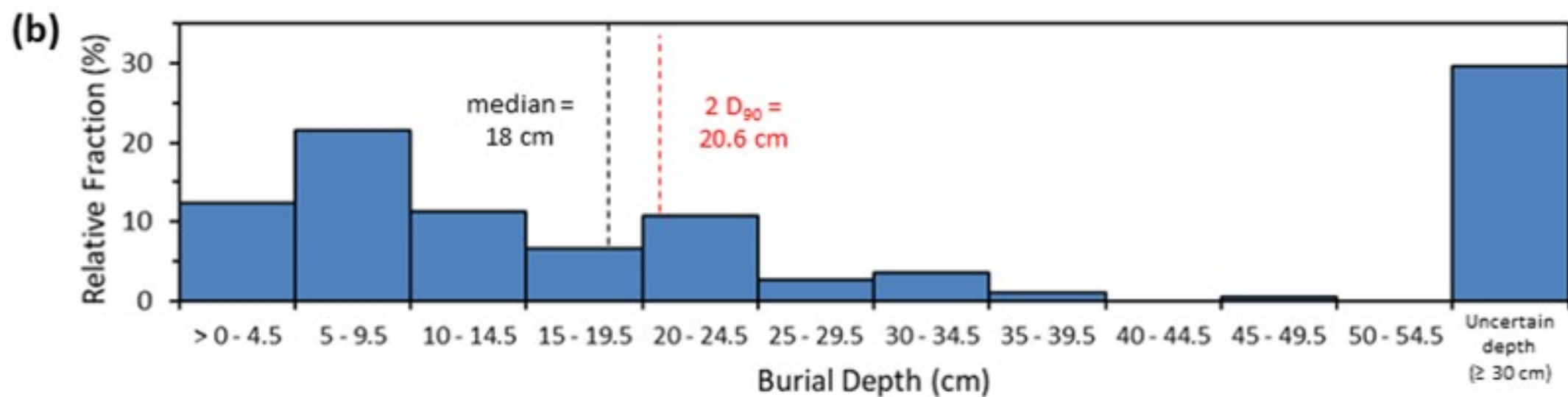
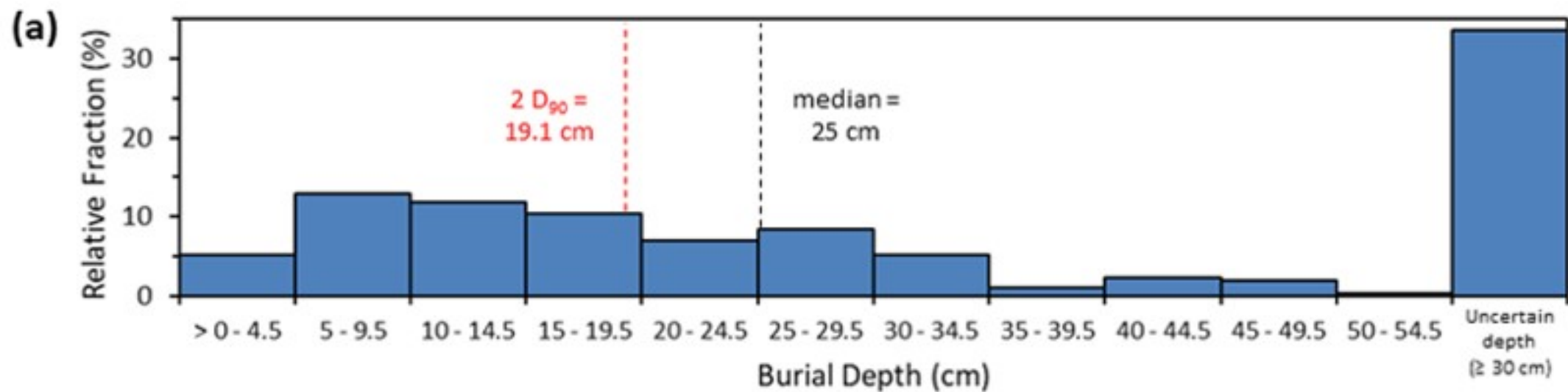


Figure 19.

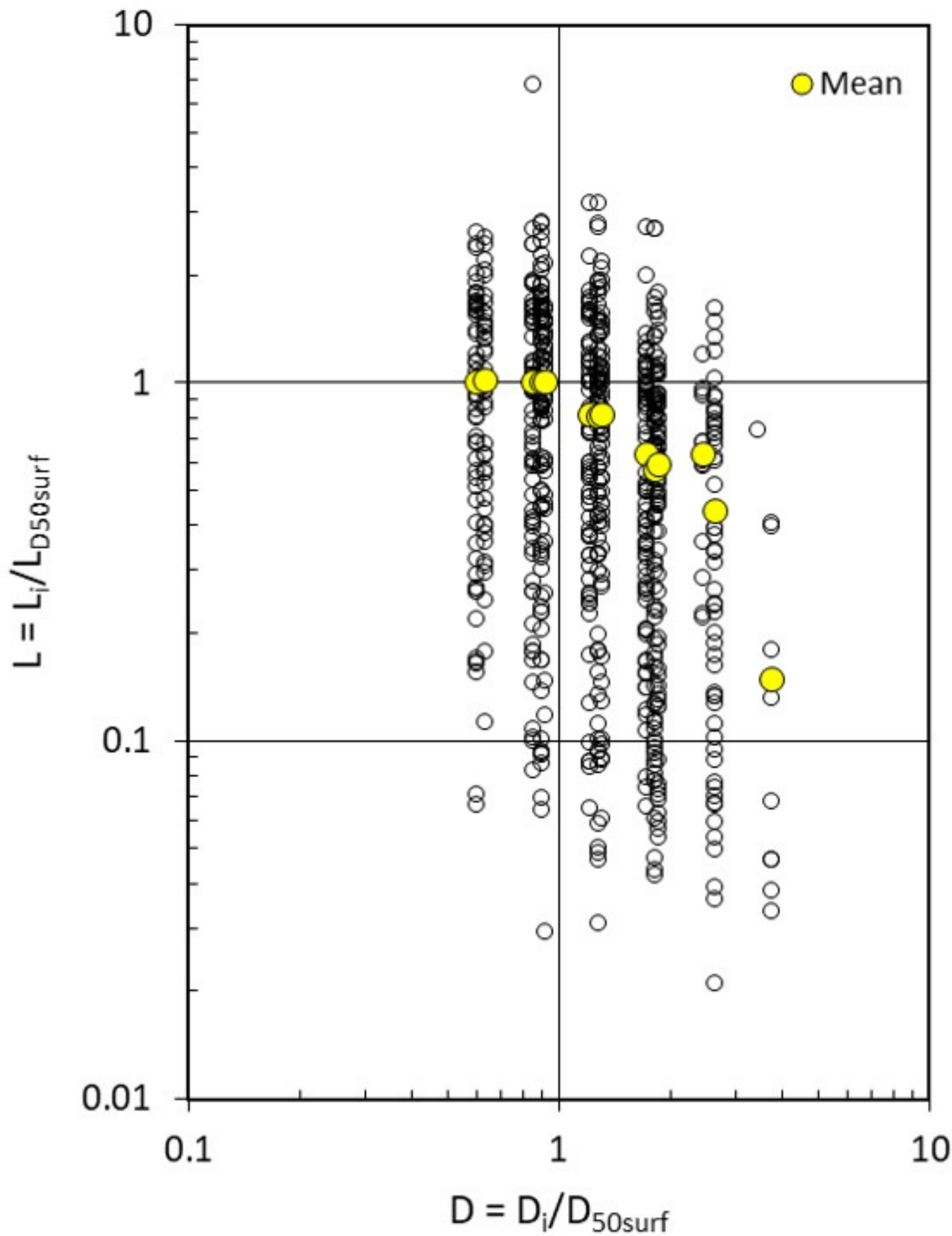


Figure 20.

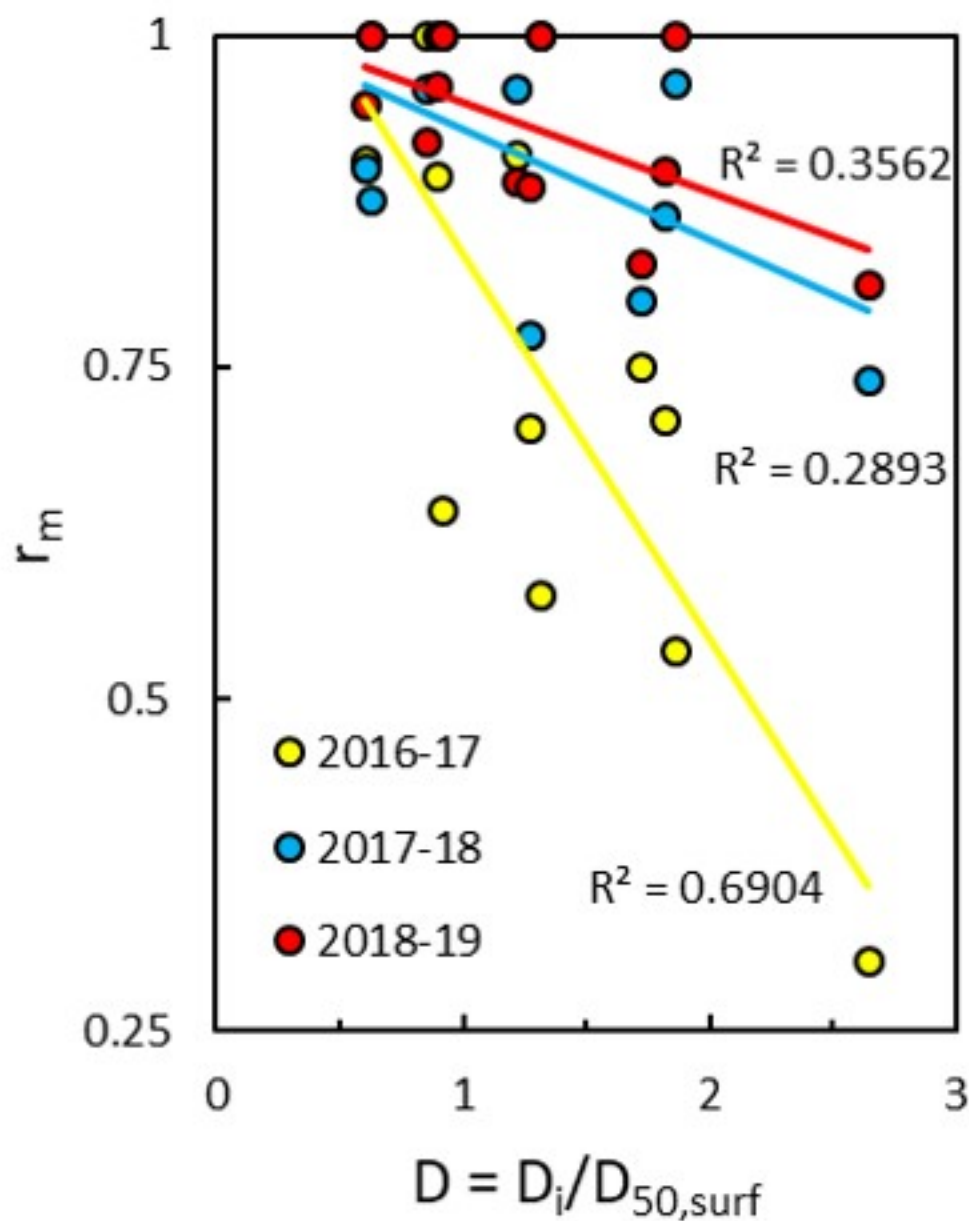


Figure 21.

1 | **Bed particle displacements and morphological development in a wandering gravel-**
2 **bed river**

3 **R. McQueen¹, P. Ashmore², T. Millard¹, and N. Goeller³**

4 ¹British Columbia Ministry of Forests, Lands, Natural Resource Operations and Rural
5 Development, Nanaimo, BC, Canada, ²Department of Geography, The University of Western
6 Ontario, London, Ontario, Canada, ³British Columbia Ministry of Environment and Climate
7 Change Strategy, Victoria, BC, Canada

8 Corresponding author: Ryan McQueen (rmcquee4@uwo.ca)

9 **Key Points:**

- 10 • Annual bed particle displacements reflect morphologic controls and differences in the
11 annual flow regime
- 12 • Bed particle transport and burial is directly tied to patterns of bar-scale erosion and
13 deposition
- 14 • Tracer deposition focused along bar margins, primarily at or downstream of the first
15 downstream bar apex
16

Formatted: Numbering: Continuous

17 **Abstract**

18 Bed particles were tracked using passive integrated transponder (PIT) tags in a wandering reach
19 of the San Juan River, British Columbia, Canada, to assess particle movement around three
20 major bars in the river. In-channel topographic changes were monitored through repeat LiDAR
21 surveys during this period and used in concert with the tracer dataset to assess the relationship
22 between particle displacements and changes in channel morphology, specifically, the
23 development and re-working of bars. This has direct implications for virtual velocity and
24 morphologic based estimates of bedload flux, which rely on accurate estimates of the variability
25 and magnitude of particle path lengths over time. Tracers were deployed in the river at three
26 separate locations in the Fall of 2015, 2016, 2017 and 2018, with recovery surveys conducted
27 during the summer low-flow season the year after tracer deployment and multiple mobilising
28 events. Tracers exhibited path length distributions reflective of both morphologic controls and
29 year to year differences related to the annual flow regime. Annual tracer transport was restricted
30 primarily to less than one riffle-pool-bar unit, even during years with a greater number of peak
31 floods and duration of competent flow. Tracer deposition and burial was focused along bar
32 margins, particularly at or downstream of the bar apex, reflecting the downstream migration and
33 lateral bar accretion observed on Digital Elevation Models (DEMs) of difference. This highlights
34 the fundamental importance of bar development and re-working underpinning bedload transport
35 processes in bar-dominated channels.

36 **1 Introduction**

37 In gravel-bed rivers there is a natural feedback between channel morphology and bedload
38 transport. The morphology of the channel is developed through the movement and deposition of
39 individual bed particles and in turn the spatial patterns of bed material transport are controlled at
40 least in part by the morphology of the channel (Church, 2006; Church and Ferguson, 2015).
41 Therefore, attempts at calculating bed material transport rates, or more generally in studying
42 bedload processes, need to consider morphologic controls on bed particle dynamics. This is
43 particularly relevant when employing the virtual velocity approach to estimating bedload flux
44 because it relies upon an accurate measure of the distribution and variability of particle path
45 lengths (travel distances), which may differ greatly in channels of different morphology
46 (Ashmore and Church, 1998; Vázquez-Tarrío et al., 2018). One idea suggested by Neill (1987),
47 is that bed particle path lengths may be related to, and inferred directly from, the channel
48 morphology. Depositional features such as bars are self-formed through individual particle
49 displacements, so it follows that over the long-term the predominant particle path lengths must
50 be related to the scale and spacing of the bars. This idea is appealing because with sufficient data
51 tying particle path length and burial with the morphological development of bars, it may
52 eventually allow path length to be estimated from morphology without the need for time-
53 consuming and resource intensive direct particle tracking. However, evidence from field-based
54 studies to support the link between bar morphology and particle path length is currently weak
55 (Hassan and Bradley, 2017).

56 Throughout the bedload tracking literature, the idea that hydraulic forcing is the primary
57 control on particle transport is prevalent, and functional relationships between average particle
58 travel distances and the combination of flow strength and/or grain size have been developed.
59 Hassan and Church (1992) demonstrated that mean tracer path length and excess stream power
60 are positively correlated for single discharge events. More recently, Phillips and Jerolmack

61 (2014) used an impulse framework to describe the effects of flow strength on particle transport.
62 Church and Hassan (1992) showed that there is a non-linear relationship between mean particle
63 path length and the size of the particle scaled by the median size of local subsurface bed material,
64 whereby travel distances of particles smaller than the median are relatively insensitive to
65 increasing grain size, but that there is a rapid decline in path length with increasing grain size for
66 particles larger than the median grain size of local subsurface bed material. These findings have
67 since been re-affirmed with data from studies across a range of channel types (Hassan and
68 Bradley, 2017; Vázquez-Tarrío et al., 2018), though data from larger, bar-dominated channels is
69 lacking. Milan (2013) demonstrated that this effect is, at least in part, caused by differences in
70 the duration of competent flow for different grain sizes. Many tracer studies, however, have
71 noted differences between path length distributions and theoretical models because of tracers
72 accumulating at distinct regions related to the river morphology (e.g. Bradley and Tucker, 2012).
73 One example of this is the tendency of tracers to be preferentially transported to and stored in
74 gravel bars in channels with riffle-pool-bar morphologies, especially over longer time-scales
75 (Ferguson et al, 2002; Haschenburger, 2013).

76 In a literature review and re-analysis of published tracer data, Pyrcce and Ashmore
77 (2003b) found that the positively skewed path length distributions consistently reported in the
78 literature occurred during moderate discharge events or in smaller channels lacking well-
79 developed sedimentary structures or bar morphology. However, they found that in bar-dominated
80 channels, high magnitude flows (i.e. those capable of altering or forming bars) lead to bi- or
81 multi-modal distribution related to the location of bars. Pyrcce and Ashmore's (2003b) flume
82 experiments of an alternate bar channel aligned with these findings, as the authors demonstrated
83 that during bar-forming flows most tracers were deposited on the first bar downstream from the
84 upstream pool in which particles were seeded. Only during lower flows at the critical discharge
85 for gravel entrainment, were positively skewed distributions, with path lengths shorter than bar
86 spacing, observed. Using the same tracer dataset, Pyrcce and Ashmore (2005) showed that during
87 bar formation and development bed particle path lengths are commensurate with the spacing of
88 erosion and depositional sites, and that deposition locations tied to bar development processes. In
89 another flume experiment, Kasprak et al. (2015) demonstrated that tracer path lengths were
90 closely related to erosional and depositional processes associated with bar development in a
91 braided channel, with average path lengths on the scale of confluence-difffluence spacing. Similar
92 results have been yielded from more recent modeling of braided channels (Peirce, 2017;
93 Middleton et al., 2019). The question remains however, as to whether these observations are seen
94 in full-scale rivers where conditions are less controlled.

95 In a synthesis and re-analysis of previously published field-based tracer data, Vázquez-
96 Tarrío et al. (2018) explored the influence of both hydraulic and morphologic controls on particle
97 transport for a range of channel types. They noted that there was a weak positive correlation
98 between stream power and average travel distance for the dataset. However, when travel distance
99 was scaled by a morphological length scale for each channel type (i.e. the spacing between
100 macroscale bedforms), the scatter in the relationship was reduced, indicating that tracer transport
101 has some dependence on channel morphology. Furthermore, analyses of empirical predictors of
102 path length have pointed toward channel width as the most significant control on travel distance
103 (Beechie, 2001; Vázquez-Tarrío and Batalla, 2019). For bar-dominated channels, this may imply
104 that bar spacing exerts a control on path length because the longitudinal spacing of bars is
105 proportional to channel width. These analyses are the starting point to investigating the
106 relationship between path length, bar development and channel scale, but currently this lacks

107 tracer-based data collected in larger bar-dominated channels where morphologic control is
108 expected to be most significant. Therefore, there remains uncertainty as to whether the principles
109 of bed particle dynamics and statistics of displacements, derived from smaller rivers, such as
110 step-pool, plane-bed and low amplitude pool-riffle channels (Montgomery and Buffington,
111 1997), are applicable to bar-dominated channels with more complex morphology and higher
112 rates of morphological change, and further, if spatial patterns of tracer deposition and burial are
113 tied to bar development.

114 The paucity of tracer data collected in larger rivers may be explained in part by logistical
115 challenges in searching such large areas of channel, and the potentially deep burial of tracers
116 resulting in low recovery rates. One solution that is increasingly being used to track bed particle
117 movement in larger channels, is the use of passive integrated transponder (PIT) tags (Hassan and
118 Bradley, 2017). PIT tags are small, glass, cylindrical capsules that operate using radio frequency
119 identification (RFID) technology. Several factors make PIT tags an effective technology for
120 bedload tracking including their long lifespan, resistance to abrasion and breakage (Cassel et al.,
121 2017a), and the ability to distinguish individual particles from one another using unique codes.
122 Furthermore, as smaller PIT tags are being developed, an increasingly wide range of sediment
123 sizes can be tracked (Hassan and Roy, 2016). Technological improvements in PIT tag
124 technology, such as the increased read range of antennas (Arnaud et al., 2015), innovative
125 surveying strategies (Arnaud et al., 2017) and the development of “wobblestones” (Papangelakis
126 et al., 2019; Cain and MacVicar, 2020), have made it more possible to track bed particle
127 movement in larger rivers. Active ultra high frequency (a-UHF) RFID tags have also been used
128 to explore active layer depths (Brousse et al., 2018) and particle paths (Misset et al., 2020) in
129 wandering/braided channels, providing the benefit of larger detection ranges than PIT tags. Due
130 to their large size however, aUHF tags can only be fit into natural particles with a b-axis of at
131 least 70 mm or molded into synthetic pebbles (Cassel et al. 2017b; Cassel et al., 2020).

132 The primary objective of this study was to explore the relationship between channel
133 morphology and particle path lengths in a large, wandering gravel bed river – the San Juan River,
134 British Columbia, Canada. Wandering channels are irregularly sinuous and can display aspects
135 of both meandering and braided channels. These channels are characterized by complex bar
136 development and some degree of lateral instability (O’Connor et al., 2003; Beechie et al. 2006).
137 Typically, the most common bar morphology is a lateral bar and the dominant mode of
138 deposition is lateral bar accretion (Desloges and Church, 1987; Rice et al., 2009). Church and
139 Rice (2009) describe a pattern of bar evolution whereby vertical growth is limited by the height
140 at which sediment can be elevated, and the longitudinal growth of bars is limited by the length-
141 scale of the channel, resulting in bars primarily growing laterally. This pattern of rapid lateral
142 accretion may persist for decades (Rice et al., 2009) and is accompanied by the erosion of the
143 opposite bank, producing a laterally unstable channel with less systematic migration than true
144 meandering channels (McLean et al., 1999; Fuller et al., 2003). We expect this pattern of bar and
145 channel evolution to be reflected in spatial patterns of tracer displacements for the San Juan
146 River, as bars are by definition an expression of the displacement, transport and deposition of
147 individual bed particles. If path lengths are tied to morphology in bar-dominated channels, then
148 particle displacements and burial should be tied to patterns of morphological change over a
149 defined period. To address this objective, PIT tags were used to track bed particle movements
150 and repeat LiDAR surveys were conducted to measure morphologic change and bar development
151 during the tracer monitoring period. Combining tracers with morphologic change captured at
152 high resolution is uncommon in the literature and allows a more comprehensive interpretation of

153 the process-form coupling of bedload transport and channel morphology than can be achieved
154 via either method separately (Vericat et al., 2017).

155 **2 Materials and Methods**

156 2.1 Study Site

157 The San Juan River, also known by its First Nations name, the Pacheedaht, is located on
158 southern Vancouver Island, British Columbia and drains an area of about 730 km² (Figure 1a).
159 The main channel is over 50 km long with a total relief of 690 m. The San Juan River valley
160 follows a major east-west fault with distinct topography and bedrock geology on the north and
161 south sides. Bedrock north of the river consists of a series of volcanic and intrusive units,
162 whereas the south side of the valley is underlain almost exclusively by metamorphic rocks of the
163 Leech River Complex (BCGS, 2019). The river outlets to the Strait of Juan de Fuca, near the
164 town of Port Renfrew (Figure 1a).

165 Forest harvesting in the San Juan River Watershed dates back to the early 1900s and has
166 been linked to changes in physical habitat and channel morphology in the mainstem and
167 tributaries (Ltd., 1994). This study was guided by watershed management objectives, to provide
168 detailed information on the current sediment dynamics and morphologic changes in the San Juan
169 River which will help inform future restoration decision making.

170 The study focused on the lower alluvial reach of the San Juan River beginning near Red Creek,
171 downstream of a canyon reach (Figure 1b). The alluvial channel exhibits a wandering
172 morphology, as defined by Mollard (1973) and Neill (1973), with an active width varying
173 between 50-150 m and a reach-averaged slope of 0.0011 m m⁻¹. During low-flows the river has a
174 single identifiable main channel though it displays a multi-channel pattern during higher-flows
175 when secondary channels are active. Riffle-pool-bar sequences are the primary macroscale
176 bedforms in the alluvial reach, with bars typically on the order of several hundred metres long
177 and up to 100 m wide. Bars are composed primarily of gravel, cobble and sand and there is a
178 general trend of downstream fining of surface sediment calibre both within and between bars.
179 For referencing purposes, mainstem bars were numbered, with Bar 1 being the farthest upstream
180 and subsequent bars numbered in ascending order downstream. Particle tracking focused on Bars
181 6, 7 and 15, the most accessible sites along the river (Figure 1b). These bars are representative of
182 the typical length and width, overall appearance, and grain sizes found in the alluvial reach.

183 The closest gauging station to the study sites is the Water Survey of Canada hydrometric
184 station 08HA010, which is installed on the lower San Juan River, approximately 2.5 km
185 downstream from Bar 15 and 7.5 km from Bar 6 (Figure 1b). The 2-, 10-, and 100-year floods
186 are approximately 800, 1050 and 1200 m³/s respectively, though the upper end of the rating
187 curve is uncertain due to the difficulty of obtaining discharge measurements during peak floods
188 (Figure 2). Mean monthly discharge varies from a high of 97 m³/s in January to a low of 4.5 m³/s
189 in August, with a mean annual discharge of 49 m³/s (WSC, 2019). The discharge regime closely
190 follows the seasonal trend in rainfall because 99 % of annual precipitation at low elevations falls
191 as rain (ECCC, 2019), with only transient snow accumulations (no seasonal snowpack) at higher
192 elevations within the watershed.

193 2.2 Tracer stone deployment and tracking

194 Half duplex low-frequency (134.2 kHz) PIT tags were inserted into individual gravel bed
195 particles to track annual particle movements around three major bars in the San Juan River. Low-

196 frequency tags are ideal for tracking in coastal and fluvial environments because their signal can
197 pass through water and can penetrate most non-metallic objects (sediment, wood, etc.) better
198 than high and ultra-high frequency tags (Chapuis et al., 2014; Schneider et al., 2010). In 2015,
199 100 tracers were installed along a cross-section at the head of Bar 6, while between 2016-2018 a
200 further 1199 tracers were installed across the three study sites (Bars 6, 7, and 15) with between
201 125-142 tracers per site annually. A combination of 12, 23, and 32 mm long PIT tags were used
202 in the original 2015 deployment. However, by 2017 only the 32 mm tags were used because of
203 their larger read range (Chapuis et al., 2014) and higher recovery rates during the first recovery
204 survey.

205 Wolman particle size counts were conducted at each site to characterize the size
206 distribution of surficial bed material (Table 1) (Wolman, 1954). Native stones were then
207 collected from the San Juan River and brought back to the lab for preparation, which included
208 drilling a cavity in each particle, inserting and epoxying an RFID tag in place, and painting the
209 stone (similar to methods to described in Eaton et al., 2008). Particles were selectively chosen to
210 reflect the size distribution of bed surface material in the channel as best as possible (Figure 3).
211 However, PIT tags did not fit into particles smaller than 22 mm, thus the fine end of the bed
212 material distribution was not well represented. Differences between the size distribution of bed
213 material and tracers was greatest for Bar 15, which had the finest material of the three study bars
214 (Table 1). However, the Bar 15 tracer distribution does reflect well the size distribution of local
215 surface bed material greater than 22 mm (Figure 3c). The use of 32 mm tags in 22-32 mm tracers
216 biased this size class towards particles with an a-axis longer than 35 mm.

217 Tracers were deployed annually in the fall, prior to winter flooding, along launch lines
218 perpendicular to the direction of flow. Each launch line spanned the bar head, riffle, and tail of
219 the opposite (upstream) bar, providing the opportunity to observe tracer dispersion around major
220 bars, and to observe differences in particle mobility and path lengths across different
221 morphologic units. While particle path lengths are unlikely to be influenced by seeding position
222 across the channel cross-section in smaller, plane-bed type streams, it has been shown to play a
223 significant role in particle movement in riffle-pool channels with well-developed bar
224 morphology (Liébault et al., 2012). Clusters of tracers were deployed at one to two metre
225 intervals along the launch line by replacing particles on the surface of the riverbed with tracer
226 stones to mimic natural positions and local bed texture. Tracers starting on the surface of the
227 riverbed are more exposed to flow than buried or locked particles, and therefore, observed travel
228 distances in this study are likely to be over-estimates of annual transport distances for the bed as
229 a whole.

230 Tracer recovery surveys were conducted annually during the low-flow seasons at the end
231 of July through August for 2016 to 2019. All recovered tracers were removed from the channel
232 and redeployed at their original launch line the following fall so that each year the deployment
233 strategy was a repeat of the previous one. The winter storm season with several mobilizing flows
234 is treated as an annual event producing annual particle displacements in relation to morphology.
235 This allowed us to assess the morphologic influence on tracer displacements through repeat tests.
236 This decision was also influenced by the practicalities of tracking sediment in a large river
237 because tracking after every event would be onerous and leaving tracers in the channel would
238 likely necessitate increasing the downstream extent surveyed every year, which would quickly
239 become untenable in a river of this size. Furthermore, excavating and removing tracers from the
240 channel allowed us to directly measure tracer burial depths which provides valuable information

241 on active layer dimensions and gives context to particle deposition in relation to morphological
242 development. The maximum downstream extent of survey differed for each location, though
243 generally the first two bars downstream of each seeding site were searched. The deepest portions
244 of pools were omitted from the searching process because they were not wadable, even at low-
245 flow.

246 Two antennas were used to search for tracer stones. A small handheld wand antenna, the
247 ‘BP Plus Portable’, and a larger ‘Cord Antenna System’, both were purchased from BioMark®
248 (Figure 4). Based on testing in the lab, the wand antenna had a maximum read range around 40-
249 50 cm for the 32 mm PIT tags, though the tag signals are anisotropic, and the read range was as
250 low as 10 cm for certain orientations. The wand antenna was used as the sole antenna for tracer
251 recovery in 2016, resulting in a low recovery rate (33 %), and was used only as a supplementary
252 tool to the larger antenna for subsequent years. Since PIT tag signals interfere with one another
253 when in close proximity (Lamarre et al., 2005; Chapuis et al. 2014), the wand antenna was still a
254 useful tool for distinguishing between PIT tags in areas where tracers were densely concentrated
255 - typically the launch line, as a fraction of the tracer population remained immobile. The wand
256 antenna was also effective for refining the position of tracers after detection with the cord
257 antenna.

258 The cord antenna system consisted of the cord antenna cable, secured to a 15’ x 5’ (5 m x
259 1.5 m) rectangular PVC pipe frame, mounted to a backpack frame using a series of ropes, pulleys
260 and cams (Figure 4b). The frame held the cable in a (semi-) rigid structure, stabilising the
261 antenna and allowing it to keep a high current. The operator stood in the centre of the rectangle
262 wearing the backpack and could manipulate the height of each corner of the antenna to help
263 navigate obstacles and changing topography in the field (Figure 4b). The cord antenna covered a
264 much larger surface area than the wand antenna, making it an ideal tool for searching large areas
265 efficiently. It also had a much larger range of detection than the wand antenna, with a maximum
266 read range around 1.75 m, and thus could detect tracer stones buried at greater depths.

267 Once detected, tracer positions were recorded using one of two methods, and dug up
268 (where possible) to determine a burial depth. For tracers that moved only a short distance (less
269 than 20 m or so), a measuring tape was used to directly measure transport distances from the
270 launch line. For tracers moving larger distances, a handheld Garmin GPS unit was used to record
271 tracer locations. GPS waypoint errors were on the order of two to three metres, which was
272 considered acceptable for the purpose of determining typical particle path lengths, since average
273 path lengths were generally around 100 m, resulting in less than five percent error.

274 2.3 Geomorphic change detection

275 2.3.1 Topographic surveying

276 In addition to particle tracking, repeat aerial LiDAR surveys, flown by Terra Remote
277 Sensing Inc. in 2015, 2018, and 2019, were contracted for the study and other projects related to
278 management of the river. Each LiDAR survey was conducted using the Reigl LMS-1780 sensor
279 from an airborne platform. Ground accuracy tests, performed by Terra Remote Sensing Inc.,
280 involved both internal and external horizontal and vertical checks (TRS Inc., 2018a,b, 2019).
281 Internal checks were conducted via comparison of intra- and inter-flight areas of overlap.
282 External checks consisted of two components: comparison of the LiDAR ground surface with
283 control stations not used in the calibration process, and with a series of check points collected on

284 open surfaces using Post Processed Kinematic (PPK) GPS. A root mean square error for vertical
285 precision (RMSE_v) of less than ten centimeters was reported for all surveys (Table 2) (TRS Inc.,
286 2018a,b, 2019). Survey point densities were spatially variable across the study sites. Average
287 point densities ranged from 12 to 38 points per square meter with differences based largely on
288 ground cover and topography (Table 2). LiDAR point clouds were filtered by ground and non-
289 ground classes by Terra Remote Sensing Inc. (TRS Inc., 2018a,b, 2019). LiDAR point clouds
290 were used to generate a series of raster-based digital elevation models (DEMs) of the study sites.
291 Topographic changes between survey dates were then calculated by processing the LiDAR
292 DEMs using the Geomorphic Change Detection (GCD) software (Wheaton et al., 2010) to
293 produce DEMs of difference (DoDs). LiDAR DEMs were produced for each survey at a 10 cm
294 spatial resolution by converting point clouds to a Triangulated Irregular Network (TIN), from
295 which concurrent raster DEMs were generated using linear interpolation. In-channel areas that
296 were inundated in both the old and new DEMs, where point cloud returns were either non-
297 existent or affected by refraction were not used in building DEMs, restricting change detection
298 analysis to above-water areas. To capture bank erosion, a minimum level of detection of one
299 metre was used in change detection analysis for areas that were wet in the new DEM but were
300 vegetated banks in the old DEM. This threshold allowed us to observe changes in bank position,
301 as the riverbanks are two metres or taller throughout the alluvial reach).

302 The LiDAR-derived DoDs (Difference of DEMs between successive surveys) were used
303 to interpret patterns of tracer displacement and burial depths, and to provide information on
304 morphological development of the bars during the study period. They were not used to calculate
305 complete reach-scale sediment budgets due to the lack of in-channel topographic data and stage
306 differences during each LiDAR survey affecting the relative portion of the river bed that was
307 exposed. Currently, collecting reach-scale bathymetric data in large channels is challenging and
308 relies on either boat-based multibeam echo sounding (MBES) systems or green wavelength
309 LiDAR sensors (Tomsett and Leyland, 2019).

310 2.3.2 DEM analysis

311 To account for uncertainty in the DEMs, a spatially variable uncertainty analysis was
312 conducted using the GCD ArcMap extension. This involves three main steps: 1) an estimate of
313 uncertainty for each individual DEM; 2) propagation of these errors through the DoD; and 3) an
314 assessment of the statistical significance of these uncertainties in distinguishing real geomorphic
315 change from noise (Wheaton et al., 2010). A major appeal of this method is that it requires little
316 to no additional survey error information other than the survey data itself. Further, accounting for
317 spatially-variable error allows for recovery of information in areas with low elevation
318 uncertainties that would otherwise be lost.

319 For each DEM, two surfaces were generated for uncertainty analysis using the built-in
320 tools in the GCD software: a point density raster and a slope raster. The rationale behind using
321 these surfaces was that steep areas with low point density have high elevation uncertainty,
322 whereas flat areas with high survey point density will generally have lower elevation uncertainty
323 (Wheaton et al., 2010). These surfaces were then combined on a cell-by-cell basis, using a fuzzy
324 inference system (FIS), to produce an elevation uncertainty surface. Uncertainty surfaces
325 associated with individual DEMs were then combined using simple error propagation
326 (Brasington et al., 2003) to produce a single propagated error surface for the DoD. The GCD
327 software then uses probabilistic thresholding to determine the statistical significance of these

328 uncertainties. The probability that the elevation change associated with each individual cell of
 329 the DoD is then assessed at a user-defined confidence interval, in this case 80 %. Originally, 95
 330 % was chosen, however upon examination of output thresholded DoDs, this limit appeared too
 331 restrictive, with real change being removed from areas of eroding banks and in obvious areas of
 332 deposition.

333 2.4 Hydrological Analysis

334 Discharge data from the WSC hydrometric station were used to characterize differences
 335 in the hydrologic conditions between study years. A bankfull discharge (Q_{bf}) of $500 \text{ m}^3 \text{ s}^{-1}$ was
 336 estimated from time-lapse imagery, roughly the one year return interval flood (Figure 5), with
 337 Q_{bf} being defined as the discharge at which the entire active width of the channel was inundated.
 338 This was used as a reference discharge to approximate the number of mobilising flow events per
 339 year. While previous research indicates that flows less than bankfull may mobilise coarse bed
 340 sediment (Ryan et al., 2002; Pfeiffer et al., 2017; Phillips and Jerolmack, 2019), a threshold
 341 discharge for gravel entrainment could not be accurately established for this study because
 342 tracers were exposed to multiple potentially mobilising events each year, rendering it impossible
 343 to determine which specific events caused tracer movement. Further, the complexity of channel
 344 morphology and variability in tracer grain size makes a single threshold discharge difficult to
 345 define for this study. Despite this, Q_{bf} still provides a relative basis for the number of potential
 346 mobilising flows, and the hydrograph for the period of the tracer study illustrates that even if the
 347 reference discharge were shifted substantially, say $100 \text{ m}^3 \text{ s}^{-1}$, the number of mobilising events
 348 would change very little (Figure 6).

349 Previous tracer studies have used the total excess flow energy (Ω_T) as a metric to capture
 350 the intensity and duration of competent flow for multiple flood events (Haschenburger, 2013;
 351 Papangelakis and Hassan, 2016). However, this requires knowledge of the critical discharge,
 352 which was unknown for this study. Instead, a modified Ω_T was used in analysis for this study,
 353 whereby the total flow above estimated bankfull was integrated over the period between tracer
 354 deployment (t_d) and recovery (t_r):

$$\Omega_T = \rho g S \int_{t_d}^{t_r} (Q - Q_{bf}) dt$$

355 where ρ is the density of water ($1,000 \text{ kg m}^{-3}$), g is the acceleration due to gravity (9.81 m
 356 s^{-2}), and S is the reach-average slope. Discharge data was integrated at five minute intervals (as
 357 collected at the WSC hydrometric station). The modified Ω_T , along with annual peak
 358 instantaneous discharge (Q_{max}), and number of potentially mobilising events ($Q > Q_{bf}$) were
 359 recorded for each study year to give context to differences in tracer mobility, path lengths, and
 360 burial data that might be the result of different hydrologic conditions between years. The primary
 361 purpose of this analysis is to identify any differences in annual path lengths that can be attributed
 362 to differences in the annual flow regime, and to then compare any observed differences with
 363 morphologic constraints on path lengths that may occur over the longer term related to, for
 364 example, deposition in bars.

365 3 Results

366 Tracer recovery rates were generally high for a river of the size and scale of the San Juan
 367 River (see Table 1 in Chapuis et al., 2015), with annual recovery rates exceeding 65 % for all but

368 one of the deployments (Table 3). The low recovery rate (33%) of tracers from the original 2015
369 deployment was a result of the surveying approach used in searching for tracers, as only the
370 smaller handheld wand antenna was used in the initial recovery survey in 2016. The low
371 recovery rate from this deployment limited interpretation and analysis of the data from this year,
372 and as such was removed from analyses presented in this section unless specifically noted.

373 3.1 Discharge effects on particle dynamics

374 A total of 21 events with peak greater than $500 \text{ m}^3 \text{ s}^{-1}$ occurred from 2015 to 2019,
375 ranging from four to six events per study year (Table 3). The annual instantaneous Q_{\max} during
376 the tracer study ranged from $749 \text{ m}^3 \text{ s}^{-1}$ (2016-17) to $1,022 \text{ m}^3 \text{ s}^{-1}$ (2015-16) corresponding to
377 roughly 2-yr and 6-yr return interval floods (Table 3; Figure 2). Using the modified Ω_T as a
378 metric, the ‘wettest’ year (i.e. greatest amount of flow exceeding Q_{bf}) was 2017-18, the ‘driest’
379 year was 2016-17, while 2015-16 and 2018-19 had Ω_T values in between (Table 3). The
380 sensitivity of Ω_T to the defined Q_{bf} was tested, and shifting Q_{bf} to $400 \text{ m}^3 \text{ s}^{-1}$ or $600 \text{ m}^3 \text{ s}^{-1}$ made
381 no difference to the relative ranking of Ω_T between study years, and made little difference to
382 proportional differences between years.

383 To assess annual differences in tracer movement related to discharge, Ω_T was plotted
384 against the mobility rate, median path length, and mean burial depth for each site and study year
385 (Figure 7). The relative mobility of tracers (r_m) appeared insensitive to differences in Ω_T . For
386 each bar, more than 80 % of tracers were mobilized each year, with the exception of 2016-17 Bar
387 15 tracers (48 % mobile) (Figure 7a). The low mobility of these tracers relative to other
388 deployments may be a result of both low Ω_T and also local morphodynamics (see section 3.3).

389 The median path length of tracers (L_{50}), scaled by the local bar length, showed a general
390 positive relationship with Ω_T , though this was not statistically significant when pooling the data
391 between sites ($R^2 < 0.05$) (Figure 7b). Tracers seeded at each bar tended to show different
392 responses to increasing Ω_T . The influence of Ω_T on Bar 6 and Bar 7 tracers was unclear, as the
393 wettest year of the study, 2017-18, did not produce the highest L_{50} for either site (both had
394 greater L_{50} ’s in 2018-19). However, the path length of Bar 15 tracers sharply increased with Ω_T
395 for the three years of study (Figure 7b). Despite any increases in annual path length associated
396 with Ω_T , most tracers were limited to transport distances less than one bar-length. This implies
397 that any longer-term morphologic constraints on path length, such as deposition within bars, is
398 unlikely to be substantially affected by differences in the typical annual flow regime. However,
399 this may not hold true for extreme events capable of major morphologic change in the bars and
400 river morphology.

401 Overall, there was an increase in burial depth with increasing Ω_T when pooling the data
402 across all sites ($R^2 = 0.4947$) (Figure 7c). The largest deviation from the general linear trend was
403 the 2018-19 deployment of tracers at Bar 6 ($B_{\text{avg}} = 20 \text{ cm}$). Bar 15 exhibited the lowest average
404 burial depths, while Bar 6 and 7 tracers were typically buried deeper (Figure 7c). Tracer burial is
405 explored in more detail in section 3.3 with respect to morphologic changes observed on DoDs.

406 Path length frequency distributions for tracers deployed at Bars 6, 7, and 15 are presented
407 in Figure 8 and maps illustrating the final position of recovered tracers are presented in Figures
408 9, 10, and 11 respectively. The path length distributions for 2016-17, the ‘driest’ year, were
409 positively skewed for all three sites (Figure 8) with the lowest median path lengths (L_{50}) of any
410 of the years of study (Table 3). The following year, 2017-2018, was the ‘wettest’ of the study

411 period. The Bar 6 path length distribution was also positively skewed this year, though the L_{50}
412 increased from 69 m to 130 m downstream reflective of the increased hydrologic conditions
413 (Table 3). The 2017-18 Bar 7 and Bar 15 path length distributions followed roughly symmetrical
414 distributions, with the primary mode of tracer deposition occurring at the bend apex next to Bar 7
415 (Figure 10b), and just downstream of the apex at Bar 15 (Figure 11b). In 2018-19, the year with
416 moderate Ω_T , Bar 6 tracers exhibited a bi-modal distribution with the primary mode of deposition
417 occurring just upstream of the bend apex and a secondary mode reflecting short-transport
418 distances (Figure 9b). Bar 7 and Bar 15 path length distributions for 2018-19 were positively
419 skewed, though there was a minor peak in the Bar 7 distribution, reflecting tracers accumulating
420 on the bar tail (Figure 8b, 10c). Overall, the shape of path length distributions generally reflected
421 discharge conditions, whereby positively skewed distributions were observed for the driest year,
422 bi-modal distributions were observed for two of the three sites for intermediate hydrologic
423 conditions, and roughly symmetrical distributions, centered around the bend apex at each bar
424 were observed for two of the three sites during the wettest year.

425 3.2 Morphologic effects on particle displacements

426 Tracer path lengths were scaled by the length of the bar at which they were seeded to
427 better compare particle displacements between the three bars (Figure 12). The distribution of
428 scaled path lengths were significantly different (Kruskall-Wallis test, $p < 0.05$) among all three
429 sites whereby Bar 6, Bar 7 and Bar 15 had median scaled path lengths (L_{50}) of 0.20, 0.34 and
430 0.41 ‘bar-lengths’ respectively (Table 4). Bar 6 tracers, while having the highest mobility rate
431 (89 % mobilised), had the lowest L_{50} , with 90 % of tracers depositing upstream of the bar apex
432 (which is at approximately $L = 0.50$) (Figures 9 and 12). For both 2016 and 2018 Bar 6
433 deployments, there was a clustering of tracers just upstream of the bend apex that appears to be
434 related to the growth of a coarse gravel sheet with a slip face roughly one metre high, which
435 migrated downstream from the bar head between 2015 and 2019 (Figure 13). While transport
436 past the apex was more common for Bars 7 and 15, these tracers still tended to be deposited
437 within the initial bar in which they were seeded, with deposition focused along bar margins
438 (Figures 10 and 11). This is also highlighted by the tracer escape rates, that is the fraction of
439 mobile tracers recovered downstream of the initial bar in which they were seeded. Less than one
440 percent of tracers escaped Bar 6 annually, five percent escaped Bar 7, and four percent escaped
441 Bar 15 (Table 4) indicating that annual particle displacements on the San Juan River tend to be
442 within one riffle-pool-bar unit.

443 Tracers recovered in the wetted channel, closer to the thalweg, may be more likely to be
444 remobilised by future events, and as such represent potential future frontrunners, while those
445 stored on gravel bars are less likely to be remobilized, and may become trapped in the bars with
446 future transport limited by bar development and re-working. For Bar 6, 66 % of tracers were
447 deposited in or on bars, while 34 % were recovered in the wetted channel. Similarly, 71 % of Bar
448 7 tracers were recovered on bars versus 29 % in the wetted channel. Bar 15 appears to trap less
449 sediment than the other sites, as only 46 % of tracers were recovered on gravel bars versus 54 %
450 in the wetted channel, as Bar 15 is less-developed laterally than the other study bars. For each of
451 the sites however, the proportion of tracers recovered on gravel bars reflects more than just those
452 transported to and deposited on bars, it also reflects tracers that were originally seeded on bar
453 tails and remained there. The role of initial seeding morphology was explored by partitioning the
454 data by the morphologic unit in which tracers were originally deployed (Table 5). The Bar 6
455 2016 launch was treated separately from the rest of the Bar 6 data as the launch line was located

456 120 m downstream of the other years, with tracers seeded across the bar edge and adjacent pool.
457 In general, tracers seeded on bar tails tended to have lower relative mobility than those seeded on
458 the bar heads or the in the wetted channel (Table 5). The exception to this was that 80 % of bar
459 tail tracers were mobilised for Bar 15 versus 73 % mobility in the wetted channel (Table 5).
460 When breaking this data down further however, 92 and 93 % of wetted channel tracers were
461 mobilized at Bar 15 during 2017 and 2018 deployments respectively, and only the 2016 tracers
462 exhibited low mobility in the wetted channel (40 % mobile). Tracers deployed on bar heads were
463 almost always mobilized (100 % mobile for Bar 6, and 98 % for Bar 15), suggesting that these
464 areas are active erosional sites. These differences highlight the importance that deployment
465 strategy and channel morphology can have on tracer dispersion, as recently shown by McDowell
466 and Hassan (2020).

467 Box plots of tracer scaled path lengths for each seeding morphologic unit for each study
468 site is presented in Figure 14. For Bar 6 (2015, 2017, 2018 deployments), tracers seeded on the
469 bar tail had a lower median scaled path length than those seeded on the bar head or in the wetted
470 channel (Table 5). However, differences in the distributions between seeding morphologies was
471 not statistically significant (Kruskall Wallis test, $p > 0.05$). Bar 6 tracers tended to be deposited
472 upstream of the bar apex regardless of where they were initially seeded, with clustering
473 coincident with the development of the migrating gravel sheet terminating at the bar apex (Figure
474 13). For the 2016 Bar 6 deployment, there was a statistically significant difference (Mann
475 Whitney U test, $p < 0.001$) between the path length distribution of tracers seeded in the wetted
476 channel (specifically a pool in this case) and those seeded on the bar edge. Bar edge tracers were
477 restricted to path lengths less than 0.3 bar lengths downstream, while those seeded in the pool
478 more frequently travelled farther downstream, with a maximum observed path length of 0.78 bar
479 lengths (Table 5). Again, bar edge tracers appear to become incorporated into the migrating
480 gravel sheet at this location. The scaled path length distributions were significantly different
481 (Mann Whitney U test, $p < 0.001$) for Bar 7 tracers seeded in the wetted channel relative to those
482 seeded on the adjacent bar tail, with median path lengths of 0.39 and 0.21 bar lengths for wetted
483 channel and bar tail tracers respectively. Similarly, Bar 15 tracers seeded on the bar tail had a
484 significantly different path length distribution than either those seeded on the bar head ($p < 0.001$)
485 or bar tail ($p < 0.05$) based on a Kruskal Wallis test and Dunn's post hoc comparison. Overall,
486 tracers seeded on bar tails tended to be both less mobile and were displaced shorter distances on
487 average than those seeded either in the wetted channel or on bar heads, underlining the spatially
488 variable nature of bed-material transport in bar-dominated channels.

489 3.3 Morphologic change and particle burial

490 Path length data demonstrated a relation with channel morphology which can be further
491 explored in relation to the geomorphic change detection analysis and by incorporating tracer
492 burial depth data. DoDs are presented for 2015-2018 and 2018-2019 for the Bars 6-7 reach in
493 Figure 15 with tracer burial depths and locations overlaid on top. Bar 15 DoDs with buried
494 tracers for the same periods are presented in Figure 16. Tracers that were located using the cord
495 antenna system but were too deep to be detected by the wand antenna (or physically recovered),
496 were estimated to be deeper than 30 cm (a conservative estimate of the maximum detection
497 range of the wand antenna). Tracers recovered in pools were not physically recovered so burial
498 depth was unknown and they were not included in burial depth analyses.

499 For the Bar 6-7 reach, a general pattern of downstream bar migration was observed over
500 the period of study. Primary areas of erosion include the heads of Bars 6, 7, the small point bar
501 between Bars 6 and 7, and erosion of the banks opposite the bars. Scour pools also developed
502 along the tail of Bar 6 between 2015 and 2018 (Figure 15). Bar surfaces were net depositional
503 across the Bars 6 and 7 DoDs, with maximum deposition focused at the bar apexes and bar tails,
504 resulting in lateral accretion and downstream migration of bars. Areas of indeterminate change
505 were mostly in-channel areas such as riffles and pools. The Bar 15 DoDs exhibited a similar
506 pattern of morphologic change, with erosion focused at the head of Bar 15 and bank retreat
507 opposite the downstream portion of Bars 15 and 16 (Figure 16), leading to a pattern of
508 downstream bar and bend migration. The downstream portion of Bars 15 and 16 were net
509 depositional, with maximum deposition focused downstream of the bar apexes (Figure 16).

510 In general, the spatial pattern of tracer deposition was well-reflected in the DoDs. For Bar
511 6, 49 % of tracers were recovered in areas corresponding to known geomorphic change on the
512 DoDs (Table 6). Of these tracers 88 % resided in depositional cells and 12 % in erosional cells.
513 The deepest buried tracers (> 30 cm) tended to be deposited near the apex of Bar 6, which aligns
514 with the downstream extent of the migrating gravel sheet in this area (Figure 13). For Bar 7, 65
515 % of recovered tracers were located in areas of known geomorphic change, with 91 % in
516 depositional cells and 9 % in erosional cells (Table 6). The deepest buried Bar 7 tracers were
517 recovered either near the bar apex or on the bar at the launch line (Figure 15). Due to the lack of
518 topographic data captured in the wetted channel, only 23 % of tracers from Bar 15 were
519 recovered in areas of known geomorphic change, in large part due the high proportion of Bar 15
520 tracers that remained in the initial riffle in which they were seeded. For those located in areas of
521 known change, 70 % were located in depositional cells and 30 % in erosional cells (Table 6).
522 Across all three study sites, tracers tended to be recovered in areas of deposition on DoDs when
523 there was known geomorphic change, which supports the idea that particle transport and
524 deposition is tied to overall channel morphodynamics. For the portion of tracers recovered in
525 areas of indeterminate change on DoDs the link between particle deposition and morphologic
526 change cannot be established. However, these areas were most commonly bar margins and riffles
527 (Figure 15 and 16), areas that are likely to be depositional environments.

528 There was no correlation observed between tracer burial depth and the corresponding
529 elevation change from DoDs for any of the three sites (Figure 17). This is perhaps not surprising
530 since the timing between tracer deployments and recoveries does not match the time between
531 topographic surveys used to produce the DoDs and because tracers could only be recovered
532 within approximately 50 cm of the bed surface whereas scour and fill occurred at depths beyond
533 this. Overall, the mean burial depth of tracers recovered in depositional cells was greater than
534 those in recovered in erosional cells for each site, though the low number of tracers recovered in
535 erosional cells prevents the results from being statistically significant (Table 6).

536 The distribution of tracer burial depths for Bar 6, 7 and 15 are presented in Figure 18.
537 The maximum burial depth for Bar 6 tracers was 52 cm, although 34 % of tracers were not
538 physically recovered, and we suspect that they are buried deeper than 30 cm (because they were
539 not detected with the wand antenna) (Figure 18a). Assuming that these tracers were buried
540 beyond this depth, the median burial depth for Bar 6 tracers was 25 cm. A maximum burial depth
541 of 47 cm was recorded for Bar 7 tracers, with 30 % of tracers not physically recovered, likely
542 due to deep burial, resulting in an overall median burial depth of 18 cm (Figure 18b). For both
543 locations, more than 40 % of tracers were recovered at depths exceeding the commonly quoted

544 assumed active layer depth of $\sim 2 D_{90}$ of the surface (Wilcock and McArdell, 1997; Hassan and
545 Bradley, 2017). Tracer burial data from Bars 6 and 7 suggests that maximum active layer
546 thickness may be 50 cm or greater locally. This indicates that in this type of channel the particle
547 exchange during bed material transport may operate at depths beyond a surface layer a few
548 grains thick for at least a portion of the bed and active layer depth is governed by the distribution
549 of bar-scale erosion and deposition. The median burial depth of 10 cm for Bar 15 tracers was the
550 lowest of the three study sites (Figure 18c). The lower tracer burial on Bar 15 relative to the
551 other sites aligns with the lower magnitudes of morphologic change observed on DoDs relative
552 to the Bar 6 and Bar 7 reach. Because morphologic change drives burial depth, and local bar
553 dynamics and morphology differ between sites, this produces differences in tracer dispersion and
554 burial between sites.

555 3.4 Grain size effects on tracer mobility and path length

556 The path length of San Juan River tracers exhibited a similar relationship with grain size
557 as described previously in the literature (Church and Hassan, 1992; Hassan and Bradley, 2017),
558 with particles larger than the local D_{50} exhibiting a steep decline in mean path length with
559 increasing grain size, and particles smaller than the local D_{50} showing less variation in mean path
560 length with increasing grain size (Figure 19). However, while the mean travel distance of each
561 tracer size fraction follow this non-linear trend, there is a large amount of scatter in the data
562 suggesting that other factors, such as channel morphology and hydrologic conditions, play an
563 important role on particle transport. The relative mobility of each tracer size fraction is presented
564 in Figure 20, where the tracer size class is scaled by the local surface D_{50} . In general, relative
565 mobility decreased with increasing relative grain size. This trend was moderately strong for the
566 2016-17 tracer displacements ($R^2 = 0.6904$) and weak for the 2017-18 and 2018-19
567 displacements ($R^2 = 0.2893$ and 0.3562 respectively). The 2016-17 season was the ‘driest’ year
568 during the study period, in terms of both Q_{max} and the total duration of competent flow,
569 suggesting that hydrologic conditions limited mobility of larger sizes compared to the ‘wetter’
570 years when most of the bed was mobilised regardless of grain size.

571 4 Discussion

572 The results from particle tracking in the San Juan River reveal insights into bed particle
573 dynamics in a wandering-style gravel-bed river, which has seldom been a focus in previous
574 studies. The recovery rate of tracers in this study combined with morphologic change data is
575 unique for a channel of this size and as such provides important information on the nature of
576 bedload transport in these systems. This data can also help to develop tracer displacement
577 statistics and models for this type of river with respect to morphologic change and bar
578 development.

579 The intrabedform, or intrabar, transport that was observed on the San Juan River, aligns
580 with results from the few previous bedload tracking results on larger, bar-dominated channels.
581 On a meandering section of the Ain River, France, Rollet et al. (2008) conducted a PIT tag tracer
582 study, recovering 36 % of tracers after one year, with an average travel distance of 50 m, less
583 than one bar length downstream. While interpretation of particle transport was limited by the low
584 recovery rate, the authors noted that over the tracer monitoring period, a thick sedimentary layer
585 had accreted on the edge of the gravel bar immediately downstream of the tracer injection site
586 and posited that lost tracers were likely buried at this location, beyond their antenna’s maximum

587 range of detection. This description of bar growth is similar to changes observed on Bar 6 of the
588 San Juan River, where tracer clustering and lateral accretion was focused at the bar apex. In
589 another PIT tag study, conducted on a wandering riffle-pool reach of the Durance River, France,
590 Chapuis et al. (2015) recovered 40 % of tracers after four months, with an average particle path
591 length of 83 m, again indicative of transport within one riffle-pool unit. As observed on the San
592 Juan River, the authors noted that particles deployed on bar tails were either immobile or only
593 displaced short distances, while those seeded closer to the thalweg were transport farther
594 downstream. Similar variations in transport conditions between morphologic units were reported
595 from PIT tag and painted tracer data collect from a wandering reach of the Parma River, Italy
596 (Brenna et al., 2019). The spatial variability in bedload transport, intrinsic to the riffle-pool
597 morphology, means that deployment strategy has a strong influence on tracer mobility and
598 resultant path length distributions. In the cases of the Ain, Durance, and San Juan Rivers, tracers
599 tended to remain within one morphological unit, with minimal transport downstream. This
600 provides direct evidence that in addition to hydraulic controls, channel morphology influences
601 particle dynamics in these systems. Particle trapping and burial in association with bar
602 development appears to be an important consideration in modeling sediment behaviour in this
603 type of river, and therefore in the bedload transport process more generally. This emphasizes the
604 morphologic control on bed particle transport, a point that was also raised in a re-analysis of
605 bedload tracking data by both Vázquez-Tarrío et al. (2018) and McDowell and Hassan (2020).

606 The pattern of particle displacement and deposition on the San Juan River reflected a
607 combination of morphologic controls and seasonal variations in the flow regime. During the
608 2017-18 winter, the wettest study year, bedload deposition focused at the apex of the first bar
609 downstream for Bars 7 and 15, and either slightly positive or symmetrical distributions around
610 the bar apex were observed. However, during years with more moderate floods and lower
611 competent flow volume, path length distributions tended to be positively skewed, with lower
612 tracer mobility. It should be noted here that these results specifically pertain to particles seeded
613 on the bed surface near the bar head. At least this is the case for the first movement of tracers,
614 while subsequent events in the same year could be acting on both surficial and buried tracers.
615 Differences in the spatial distribution of tracers between sites also appears related to channel
616 shape and bar morphology. At Bar 6, the high-amplitude bend, and migration of a coarse bedload
617 sheet, appear to restrict transport to the bar tail. Whereas tracer deposition on the bar tail was
618 more common for Bars 7 and 15, bars that are less well-developed laterally. Overall, the results
619 from this study provide some validation to the findings from Pyrcce and Ashmore's flume
620 experiments (2003a; 2005) whereby they observed bi- and multi-modal path length distributions
621 during bar-forming discharges, with modes coincident with bar apexes, and spatial patterns of
622 tracer deposition related to bar-scale patterns of erosion and deposition.

623 To further compare tracer transport on the San Juan River with results from the literature,
624 Figure 4 from Vázquez-Tarrío et al. (2018), has been re-created in Figure 21 with data from Bars
625 6, 7, and 15 on the San Juan River. The original figure contains travel distances of tracers
626 starting from both unconstrained (i.e. initial movement after seeding, as done in this study) and
627 constrained (movement after tracers have been incorporated into the bed) positions. In this graph,
628 dimensionless stream power (ω^*) was calculated as in Eaton and Church (2011), to compare
629 flow strength and particle transport across rivers of different scales. Mean scaled travel distances
630 were scaled using a morphologic length scale (i.e. the spacing of macroscale bedforms), which
631 for the San Juan River meant the riffle-riffle spacing. Data from the 2015-16 deployment on Bar
632 6 were not plotted on this graph due to the low recovery rate (33 %) and uncertainty in the

633 statistics of particle displacement for this year. The San Juan River data appear in line with
634 results from riffle-pool channels, showing a positive relationship between dimensionless stream
635 power and mean scaled travel distance, though travel distances on the San Juan River were
636 relatively low (Figure 21). What is more interesting though, and as noted by Vázquez-Tarrío et
637 al. (2018), is that riffle-pool channels share a common trait in that they rarely exhibit average
638 travel distances beyond 1-2 length-scale units (regardless of constrained or unconstrained
639 starting position), generally at the lower end of the range for other channel types. It appears that
640 riffle-pool channels have limited transport distances compared with other channels, presumably a
641 result of bars and riffles constraining particle movement. Over the long-term, path lengths are
642 therefore likely to be limited by the rate of bar development and re-working, which in turn plays
643 an important role in overall channel evolution and stability (Rice et al., 2009; Reid et al., 2019).

644 The path length distributions presented in this study reflect annual particle transport over
645 a four year period. The annual displacements occur from multiple events in the well-defined
646 high-flow season from October to March. This is consistent each year although exact magnitudes
647 vary. Particles are ‘slaved’ to the bar development and few move through to the next bar any
648 given year. The preferential deposition and incorporation of tracers in bars has been previously
649 demonstrated to hold true over longer time-scales in gravel-bed rivers in general (e.g. Ferguson
650 et al., 2002; Haschenburger, 2013). Therefore, we expect that these annual path lengths are
651 representative of the normal bar development except in the case of a high magnitude flood
652 sufficient to disrupt the existing bar and channel configuration, in which case displacements
653 would be expected to reflect that larger scale morphological change. For morphological flux
654 calculation this would produce an annual flux based on net morphological change and tracer
655 distances scaled to the bars.

656 The tracer burial data provide context to the path length analysis and revealed insights
657 into patterns of sediment transfer and storage. Burial depths up to, and likely exceeding, 50 cm
658 were recorded at each of the three sites, although the absolute magnitude of maximum particle
659 burial depth was not obtained in this study due to methodological constraints. However, the
660 development of “wobblestone” technology looks to provide a promising solution to estimating
661 particle burial without the need to physically recover the particles and disturb the bed
662 (Papangelakis et al., 2019). Overall, tracer burial aligned with the patterns of bar-scale deposition
663 observed on DoDs, which raises two important points. First, this suggests that as individual
664 particles are transported to and buried in local areas of deposition, they become incorporated into
665 the channel morphology, and future movement will be limited by the rate of bedform (or bar)
666 migration. This relates back to Neill’s (1987) original speculation that over the long term,
667 average particle path lengths may be inferred from the channel morphology. Secondly, the fact
668 that more than 30 % of buried tracers were recovered at depths beyond twice the local D_{90} for
669 each site suggests that the concept of a shallow active layer less than two particles deep does not
670 reflect the nature of bedload processes occurring in this type of channel. It should be noted
671 however, that the winter storm season was treated as a single event for this study, and that there
672 were multiple events each year that may have produced the reported burial depths. As described
673 by Ashmore et al. (2018), it appears that bed particle deposition and burial in larger, more
674 dynamic rivers is controlled by bar-scale patterns of deposition, whereby the active layer is
675 spatially non-uniform and maximum burial depths occur on the scale of vertical changes in bed
676 level associated with those dominant morphological processes. This is important because the
677 dimensions of the active layer, when combined with the virtual velocity of bed particles, gives
678 the morphological bedload transport rate (Haschenburger and Church, 1998; Liébault and

679 Laronne, 2008; Vázquez-Tarrío and Menéndez-Duarte, 2014; Mao et al. 2017; Vericat et al.,
680 2017).

681 **5 Conclusion**

682 The primary goal of this study was to investigate the interplay between channel
683 morphology and bed particle displacements in a wandering gravel-bed river channel, and more
684 specifically, to assess whether displacement is tied to bar scale and patterns of bar development
685 and accretion. This has implications for path length when applied to virtual velocity and
686 morphological estimates of bedload and possible differences among rivers of different
687 morphology and size.

688 Tracers exhibited path length distributions related to morphologic controls (deposition
689 near the bar apex) and differences year to year related to the annual flow regime, with greater
690 dispersion observed during years with greater number of peak floods and flow volume above the
691 threshold discharge for bed mobility. Additionally, tracer deposition and burial were reflected by
692 areas of deposition on DEMs of difference (DoDs). Tracers tended to be deposited along bar
693 margins and to a lesser extent, the surface of the downstream portion of the bars, reflecting the
694 downstream bar migration and lateral bar accretion observed on DoDs and active layer depths
695 greater than that typically assumed in bedload analysis and modeling. This highlights the
696 fundamental importance of bar development and re-working underpinning bedload transport
697 processes in bar-dominated channels and supports recent analyses of morphological effects in
698 tracer dispersion (Vázquez-Tarrío et al., 2018). Ultimately, short-term particle displacements in
699 bar-dominated channels are linked with the morphological style of channel evolution and
700 therefore differs from bedload processes in small, plane-bed channels, for which much previous
701 analysis and theory have been developed.

702 **Acknowledgments, Samples, and Data**

703 This work was funded by the British Columbia Ministry of Forests, Lands, Natural
704 Resource Operations and Rural Development (FLNRORD) and the Pacheedaht First Nation. The
705 data used in this study can be found in the Scholars Portal Dataverse
706 (<https://doi.org/10.5683/SP2/UQGZCG>). We are thankful to Jesse Schafer for preparation of GIS
707 data, and the following persons for their field support: Andrew Boxwell, Spencer Ranson, David
708 Waine, Kyle Fukui, Dave Johnson, Ali Jones, Rachel Dugas, and several FLNRORD employees.
709 We also thank BioMark for their feedback on optimising the RFID antenna setup. Finally, we
710 would like to thank three anonymous reviewers for their thoughtful and constructive comments
711 on the original manuscript, as it has vastly improved the quality of the paper.

712 **References**

- 713 Arnaud, F., Piégay, H., Vaudor, L., Bultingaire, L., and Fantino, G. (2015). Technical
714 specifications of low-frequency radio identification bedload tracking from field experiments:
715 Differences in antennas, tags and operators. *Geomorphology*, 238, pp. 37-46.
- 716 Arnaud, F., Piégay, H., Béal, D., Collery, P., Vaudor, L., and Rollet, A. (2017). Monitoring
717 gravel augmentation in a large regulated river and implications for process-based restoration.
718 *Earth Surface Processes*, 42, pp. 2147-2166.

- 719 Ashmore, P.E., and Church, M. (1998). Sediment transport and river morphology: A paradigm
720 for study. In P.C. Klingeman, R.L. Beschta, P.D. Komar, and J.B. Bradley (Eds.) *Gravel-Bed*
721 *Rivers in the Environment* (pp. 115-148). Water Resources Publications, LLC, Highland Ranch,
722 Colorado.
- 723 Ashmore, P., Peirce, S., and Leduc, P. (2018). Expanding the “active layer”: Discussion of
724 Church and Haschenburger (2017) What is the “active layer?” *Water Resources Research* 53, 5-
725 10, Doi:10.1002/2016WR019675. *Water Resources Research*, 54, pp. 1-3.
- 726 BC Geological Survey (2018). Bedrock geology [Shapefile]. Retrieved from:
727 [https://catalogue.data.gov.bc.ca/dataset/bedrock-geology/resource/aa3a15f8-02fe-49c6-836c-](https://catalogue.data.gov.bc.ca/dataset/bedrock-geology/resource/aa3a15f8-02fe-49c6-836c-6866c326203d?inner_span=True)
728 [6866c326203d?inner_span=True](https://catalogue.data.gov.bc.ca/dataset/bedrock-geology/resource/aa3a15f8-02fe-49c6-836c-6866c326203d?inner_span=True)
- 729 Beechie, T.J. (2001). Empirical predictors of annual bed load travel distance, and implications
730 for salmonid habitat restoration and protection. *Earth Surface Processes and Landforms*, 26, pp.
731 1025-1034.
- 732 Beechie, T.J., Liermann, M., Pollock, M.M., Baker, S., and Davies, J. (2006). Channel pattern
733 and river-floodplain dynamics in forested mountain river systems. *Geomorphology*, 78, pp. 124-
734 141.
- 735 Bradley, D.N., and Tucker, G.E. (2012). Measuring gravel transport and dispersion in a
736 mountain river using passive radio tracers. *Earth Surface Processes and Landforms*, 37, pp.
737 1034-1045.
- 738 Brasington, J., Langham, J., Rumsby, B. (2003). Methodological sensitivity of morphometric
739 estimates of coarse fluvial sediment transport. *Geomorphology*, 53, pp. 299-316.
- 740 Brenna, A., Surian, N., and Mao, L. (2019). Virtual velocity approach for estimating bed
741 material transport in gravel-bed rivers: Key factors and significance. *Water Resources Research*,
742 55, pp. 1651-1674.
- 743 Brousse, G., Liébault, F., Arnaud-Fassetta, G., Vázquez-Tarrío, D. (2018). Experimental bed
744 active-layer survey with active RFID scour chains: Example of two braided rivers (the Drac and
745 the Vénéon) in the French Alps. *E3S Web of Conferences*, 40, 04016.
- 746 Cain, A., and MacVicar, B. (2020). Field tests of an improved sediment tracer including non-
747 intrusive measurement of burial depth. *Earth Surface Processes and Landforms*.
748 DOI:10.1002/esp.4980.
- 749 Cassel, M., Piégay, H., and Lavé, J. (2017a). Effects of transport and insertion of radio frequency
750 identification (RFID) transponders on resistance and shape of natural and synthetic pebbles:
751 applications for riverine and coastal bedload tracking. *Earth Surface Processes and Landforms*,
752 42, pp. 399-413.
- 753 Cassel, M., Dépret, T., and Piégay H. (2017b). Assessment of a new solution for tracking
754 pebbles in rivers based on active RFID. *Earth Surface Processes and Landforms*,
755 DOI:10.1002/esp.4152.
- 756 Cassel, M., Piégay, H., Fantino, G., Lejot, J., Bultingaire, L., Michel, K., and Perret, F. (2020).
757 Comparison of ground-based and UAV a-UAF artificial tracer mobility monitoring methods on a
758 braided river. *Earth Surface Processes and Landforms*, 45, pp. 1123-1140.

- 759 Chapuis, M., Bright, C.J., Hufnagel, J., and MacVicar, B. (2014). Detection ranges and
760 uncertainty of passive Radio Frequency Identification (RFID) transponders for sediment tracking
761 in gravel rivers and coastal environments. *Earth Surface Processes and Landforms*, 39(15), pp.
762 2109-2120.
- 763 Chapuis, M., Dufour, S., Provansal, M., Couvert, B., and de Linares, M. (2015). Coupling
764 channel evolution monitoring and RFID tracking in a large, wandering, gravel-bed river: Insights
765 into sediment routing on geomorphic continuity through a riffle-pool sequence. *Geomorphology*,
766 231, pp. 258-269.
- 767 Church, M. (2006). Bed material transport and the morphology of alluvial river channels. *The*
768 *Annual Review of Earth and Planetary Science*, 34, pp. 325-354.
- 769 Church, M., and Ferguson, R.I. (2015). Morphodynamics: Rivers beyond steady state. *Water*
770 *Resources Research*, 51, pp. 1883-1897.
- 771 Church, M., and Hassan, M.A. (1992). Size and distance of travel of unconstrained clasts on a
772 streambed. *Water Resources Research*, 28, pp. 299-303.
- 773 Church, M., and Rice, S.P. (2009). Form and growth of bars in a wandering gravel-bed river.
774 *Earth Surface Processes and Landforms*, 34, pp. 1422-1432.
- 775 Desloges, J.R., and Church, M. (1987). Channel and floodplain facies in a wandering gravel-bed
776 river. In *Recent development in fluvial sedimentology*, 39 (pp. 99-109). Society of Economic
777 Paleontologists and Mineralogists.
- 778 Eaton, B., Hassan, M., and Phillips, J. (2008). A Method for Using Magnetic Tracer Stones to
779 Monitor Changes in Stream Channel Dynamics. *Streamline: Watershed Management Bulletin*,
780 12(1), pp. 22-28.
- 781 Eaton, B., and Church, M. (2011). A rational sediment transport scaling relation based on
782 dimensionless stream power. *Earth Surface Processes and Landforms*, 37, pp. 901-910.
- 783 Environment and Climate Change Canada (2019). Canadian Climate Normals 1981-2010 Station
784 Data. Retrieved from:
785 http://climate.weather.gc.ca/climate_normals/results_1981_2010_e.html?stnID=82&autofwd=1
- 786 Ferguson, R.I., Bloomer, D.J., Hoey, T.B., and Werritty, A. (2002). Mobility of river tracer
787 pebbles over different timescales. *Water Resources Research*, 38(5), pp. 3-1 – 3-8.
- 788 Fuller, I.C., Large, A.R.G., and Milan, D.J. (2003). Quantifying channel development and
789 sediment transfer following chute cutoff in a wandering gravel-bed river. *Geomorphology*, 54,
790 pp. 307-323.
- 791 Haschenburger, J.K. (2013). Tracing river gravels: Insights into dispersion from a long-term field
792 experiment. *Geomorphology*, 200, pp. 121-131.
- 793 Haschenburger, J.K., and Church, M. (1998). Bed material transport estimated from the virtual
794 velocity of sediment. *Earth Surface Processes and Landforms*, 23, pp. 791-808.
- 795 Hassan, M.A., and Bradley, D.N. (2017). Geomorphic controls on tracer particle dispersion in
796 gravel bed rivers. In D. Tsutsumi, and J.B. Laronne (Eds.) *Gravel Bed Rivers: Processes and*
797 *Disasters*, 1 (pp. 159-184). John Wiley & Sons Ltd.

- 798 Hassan, M.A., and Roy, A.G. (2016). Coarse particle tracking in fluvial geomorphology. In G.M.
799 Kondolf, and H. Piégay (Eds.) *Tools in Fluvial Geomorphology. Second Edition* (pp. 306-323).
800 Chichester, West Sussex England: Wiley Blackwell.
- 801 Hassan, M.A., Church, M., and Ashworth, P.J. (1992). Virtual rate and mean distance of travel of
802 individual clasts in gravel-bed channels. *Earth Surface Processes*, 17, pp. 617 - 627.
- 803 Kasprak, A., Wheaton, J.M., Ashmore, P.E., Hensleigh, J.W., and Peirce, S. (2015). The
804 relationship between particle travel distance and channel morphology: Results from physical
805 models of braided rivers. *Journal of Geophysical Research: Earth Surface*, 120, pp. 55-74.
- 806 Lamarre, H., MacVicar, B., and Roy, A.G. (2005). Using passive integrated transponders (PIT)
807 tags to investigate sediment transport in gravel-bed rivers. *Journal of Sedimentary Research*, 75,
808 pp. 736-741.
- 809 Liébault, F., and Laronne, J.B. (2008). Evaluation of bedload yield in gravel-bed rivers using
810 scour chains and painted tracers: the case of the Esconavette Torrent (Southern French Prealps).
811 *Geodinamica Acta*, 21, pp. 23-34.
- 812 Liébault, F., Bellot, H., Chapuis, M., Klotz, S., and Deschâtres, M. (2012). Bedload tracing in a
813 high-sediment-load mountain stream. *Earth Surface Processes and Landforms*, 37, pp. 385-399.
- 814 Mao, L., Picco, L., Lenzi, M.A., and Surian, N. (2017). Bed material transport estimate in large
815 gravel-bed rivers using the virtual velocity approach. *Earth Surface Processes and Landforms*,
816 42, pp. 595-611.
- 817 McDowell, C., and Hassan, M.A. (2020). The influence of channel morphology on bedload path
818 lengths: Insights from a survival process model. *Earth Surface Processes and Landforms*. DOI:
819 10.1002/esp/4946.
- 820 McLean, D.G., Church, M., and Tassone, B. (1999). Sediment transport along lower Fraser River
821 1. Measurements and hydraulic computations. *Water Resources Research*, 35(8), pp. 2533-2548.
- 822 Middleton, L., Ashmore, P., Leduc, P., and Sjogren, D. (2019). Rates of planimetric change in a
823 proglacial gravel-bed braided river: Field measurement and physical modelling. *Earth Surface
824 Processes and Landforms*, 44, pp. 752-765.
- 825 Milan, D.J. (2013). Virtual velocity of tracers in a gravel-bed river using size-based competence
826 duration. *Geomorphology*, 198, pp. 107-114.
- 827 Misset, C., Recking, A., Legout, C., Bakker, M., Bodereau, N., Borgniet, L., Cassel, M., Geay,
828 T., Gimbert, F., Navratil, O., Piegay, H., Valsangkar, N., Cazilhac, M., Poirel, A., and Zanker, S.
829 (2020). Combining multi-physical measurements to quantify bedload transport and
830 morphodynamics interactions in an alpine braiding river reach. *Geomorphology*, 351.
- 831 Mollard, J.D. (1973). Airphoto interpretation of fluvial features. In *Fluvial processes and
832 sedimentation. National Research Council of Canada, Ottawa, ON* (pp. 341-380). Inland Waters
833 Directorate, Department of the Environment.
- 834 Montgomery, D.R., and Buffington, J.M. (1997). Channel-reach morphology in mountain
835 drainage basins. *Geological Society of America Bulletin*, pp. 596 – 611.

- 836 Neill, C.R. (1973). Hydraulic and morphologic characteristics of Athabasca River near Fort
837 Assiniboine (pp. 1-23). Alberta Research Council, Edmonton, Highway and River Engineering
838 Division Report REH/73/7.
- 839 Neill, C.R. (1987). Sediment balance considerations linking long-term transport and channel
840 processes. In C.R. Thorne, J.C. Bathurst, and R.D. Hey (Eds.) *Sediment Transport in Gravel-Bed*
841 *Rivers* (pp. 225-239). John Wiley & Sons Ltd.
- 842 Northwest Hydraulic Consultants Ltd. (1994). Impact of forest harvesting in terrain stability,
843 stream channel morphology and fisheries resources of the San Juan River Watershed, Vancouver
844 Island. <http://a100.gov.bc.ca/pub/acat/public/viewReport.do?reportId=23277>
- 845 O'Connor, J.E., Jones, M.A., and Haluska, T.L. (2003). Flood plain and channel dynamics of the
846 Quinault and Queets Rivers, Washington, USA. *Geomorphology*, 51, pp. 31-59.
- 847 Papangelakis, E., and Hassan, M., (2016). The role of channel morphology on the mobility and
848 dispersion of bed sediment in a small gravel-bed stream. *Earth Surface Processes and*
849 *Landforms*, 41, pp. 2191-2206.
- 850 Papangelakis, E., Muirhead, C., Schneider, A., and MacVicar, B. (2019). Synthetic Radio
851 Frequency Identification tracer stones with weighted inner ball for burial depth estimation.
852 *Journal of Hydraulic Engineering*, 145(12), 06019014.
853 [https://doi.org/10.1061/\(ASCE\)HY.1943-7900.0001650](https://doi.org/10.1061/(ASCE)HY.1943-7900.0001650)
- 854 Pfeiffer, A.M., Finnegan, N.J., and Willebring, J.K. (2017). Sediment supply controls
855 equilibrium channel geometry in gravel rivers. *Proceedings of the National Academy of Sciences*,
856 114(13), pp. 3346-3351.
- 857 Phillips, C.B., and Jerolmack, D.J. (2014). Dynamics and mechanics of bed-load tracer particles.
858 *Earth Surface Dynamics*, 2, pp. 513-530.
- 859 Phillips, C.B., and Jerolmack, D.J. (2019). Bankfull transport capacity and the threshold of
860 motion in coarse-grained rivers. *Water Resources Research*, 55, pp. 11316-11330.
- 861 Peirce, S.E.K. (2017). Morphological bedload transport in gravel-bed braided rivers. *Electronic*
862 *Thesis and Dissertation Repository*. 4595. <https://ir.lib.uwo.ca/etd/4595>
- 863 Pyrce, R.S., and Ashmore, P.E. (2003a). Particle path length distributions in meandering gravel-
864 bed streams: Results from physical models. *Earth Surface Processes and Landforms*, 28, pp.
865 951-966.
- 866 Pyrce, R.S., and Ashmore, P.E. (2003b). The relation between particle path length distributions
867 and channel morphology in gravel-bed streams: a synthesis. *Geomorphology*, 56, pp. 167-187.
- 868 Pyrce, R.S., and Ashmore, P.E. (2005). Bedload path length and point bar development in
869 gravel-bed river models. *Sedimentology*, 52, pp. 839-857.
- 870 Reid, H.E., Williams, R.D., Brierley, G.J., Coleman, S.E., Lamb, R., Rennie, C.D., and Tancock,
871 M.J. (2019). Geomorphological effectiveness of floods to rework gravel bars: Insight from
872 hyperscale topography and hydraulic monitoring. *Earth Surface Processes and Landforms*, 44,
873 pp. 595-613.

- 874 Rice, S.P., Church, M., Woolridge, C.L., and Hickin, E.J. (2009). Morphology and evolution of
875 bars in a wandering gravel-bed river; Lower Fraser River, British Columbia, Canada.
876 *Sedimentology*, 56, pp. 709-736.
- 877 Rollet, A.J., MacVicar, B., Piégay, H., Roy, A.G. (2008). A comparative study on the use of
878 passive integrated transponders to estimate sediment transport: first results (in French). *La*
879 *Houille Blanche*, 4, pp. 110-116.
- 880 Ryan, S.E., Porth, L.S., and Troendle, C.A. (2002). Defining phases of bedload transport using
881 piecewise regression. *Earth Surface Processes and Landforms*, 27, pp. 971-990.
- 882 Schneider J., Hegglin, R., Meier, S., Turowski, J.M., Nitsche, M., and Rickenmann, D. (2010)
883 Studying sediment transport in mountain rivers by mobile and stationary RFID antennas. In A.
884 Dittrich, K. Koll, J. Aberle, and P. Geisenhainer (Eds.) *River Flow* (pp. 1723-1730). Karlsruhe:
885 Bundesanstalt für Wasserbau. S.
- 886 Terra Remote Sensing Inc. (2018a). Project report: Renfrew. September 4, 2018. (pp. 1-29).
887 Sidney, BC.
- 888 Terra Remote Sensing Inc. (2018b). Project report: Aerial LiDAR and imagery survey at San
889 Juan River, Vancouver Island, BC. April 24, 2018. (pp. 1-51). Sidney, BC.
- 890 Terra Remote Sensing Inc. (2019). Project report: Juan River change detection survey. Port
891 Renfrew, BC. November 12, 2019. (pp. 1-45). Sidney, BC.
- 892 Tomsett, C., and Leyland, J. (2019). Remote sensing of river corridors: A review of current
893 trends and future directions. *River Research and Applications*, pp. 1-25.
- 894 Vázquez-Tarrío, D., and Batalla, R.J. (2019). Assessing controls on the displacement of tracers
895 in gravel-bed rivers. *Water*, 11, pp. 1-21.
- 896 Vázquez-Tarrío, D., and Menéndez-Duarte, R. (2014). Bedload transport rates for coarse-bed
897 streams in an Atlantic region (Narcea River, NW Iberian Peninsula). *Geomorphology*, 217, pp. 1-
898 14.
- 899 Vázquez-Tarrío, D., Recking, A., Liébault, F., Tal, M., and Menéndez-Duarte, R. (2018).
900 Particle transport in gravel-bed rivers: Revisiting passive tracer data. *Earth Surface Processes*
901 *and Landforms*, 44, pp. 112-128.
- 902 Vericat, D., Wheaton, J.M., and Brasington, J. (2017). Revisiting the morphological approach. In
903 D. Tsutsumi and J.B. Laronne (Eds.) *Gravel Bed Rivers: Processes and Disasters*, 1 (pp. 121-
904 158). John Wiley & Sons Ltd.
- 905 Water Survey of Canada (2019). Monthly Discharge Data for SAN JUAN RIVER NEAR PORT
906 RENFREW (O8HA010) [BC]. Retrieved from:
907 [https://wateroffice.ec.gc.ca/report/historical_e.html?stn=08HA010&mode=Table&type=h2oArc](https://wateroffice.ec.gc.ca/report/historical_e.html?stn=08HA010&mode=Table&type=h2oArc&results_type=historical&dataType=Monthly¶meterType=Flow&year=2017&y1Max=1&y1Min=1)
908 [&results_type=historical&dataType=Monthly¶meterType=Flow&year=2017&y1Max=1&y](https://wateroffice.ec.gc.ca/report/historical_e.html?stn=08HA010&mode=Table&type=h2oArc&results_type=historical&dataType=Monthly¶meterType=Flow&year=2017&y1Max=1&y1Min=1)
909 [1Min=1](https://wateroffice.ec.gc.ca/report/historical_e.html?stn=08HA010&mode=Table&type=h2oArc&results_type=historical&dataType=Monthly¶meterType=Flow&year=2017&y1Max=1&y1Min=1)
- 910 Wheaton, J.M., Brasington, J., Darby, S.E., and Sear, D.A. (2010). Accounting for uncertainty in
911 DEMs from repeat topographic surveys: improved sediment budgets. *Earth Surface Processes*
912 *and Landforms*, 35, pp. 135-156.

913 Wilcock, P.R., and McArdell, B.W., (1997). Partial transport of a sand/gravel sediment. *Water*
914 *Resources Research*, 33, pp. 235-245.

915 Wolman, M.G. (1954). A method of sampling coarse river-bed material. *Transactions, American*
916 *Geophysical Union*, 35(6), pp. 951-956.

917

918

919

920

921

922

923

924

925

926

927

928

929

930

931

932

933

934

935

936

937

938

939

940

941

942

943

944

945

946 **Figure 1.** Location of (a) the San Juan River watershed and (b) study sites for tracer monitoring.

947 **Figure 2.** San Juan River annual flood frequency (data sourced from WSC, 2019).

948 **Figure 3.** Grain size distributions for surface bed-material and tracers for (a) Bar 6, (b) Bar 7,
949 and (c) Bar 15.

950 **Figure 4.** Antennas used during tracer recovery surveys. Panel (a) shows the BP Plus Portable
951 wand antenna, and panel (b) shows the Cord Antenna System.

952 **Figure 5.** Time-lapse imagery of the apex of Bar 6 on (a) September 18th, 2017 at 1:45 pm. The
953 hydrometric station recorded a discharge of 1.2 m³/s at the time of this image. The apex of Bar 6
954 on (b) November 19th, 2017 at 3:45 pm. The hydrometric station recorded a discharge of 560.4
955 m³/s at the time of this image.

956 **Figure 6.** San Juan River hydrograph from September 2015 to September 2019. Data from
957 WSC, 2019.

958 **Figure 7.** (a) Relative tracer mobility, (b) median scaled path length, and (c) mean burial depth,
959 plotted against total excess flow energy.

960 **Figure 8.** Path length frequency distribution for (a) Bar 6, (b) Bar 7, and (c) Bar 15 mobile
961 tracers (i.e. transported more than 10 m downstream).

962 **Figure 9.** Tracer recovery locations for Bar 6 deployed in (a) 2015, (b) 2016, (c) 2017, and (d)
963 2018. Note that these maps include tracers recovered in surveys two or more years after
964 deployment.

965 **Figure 10.** Tracer recovery locations for Bar 7 deployed in (a) 2016, (b) 2017, and (c) 2018.
966 Note that these maps include tracers recovered in surveys two or more years after deployment.

967 **Figure 11.** Tracer recovery locations for Bar 15 deployed in (a) 2016, (b) 2017, and (c) 2018.
968 Note that these maps include tracers recovered in surveys two or more years after deployment.

969 **Figure 12.** Box plots of scaled tracer path lengths for each study site. Note: n_m is the number of
970 mobile tracers; the box represents the 25th and 75th percentiles; the line inside the box is the
971 median; vertical lines represent the 10th and 90th percentiles; black dots represent the maximum
972 observed path length.

973 **Figure 13.** Planform view of the migrating bedload sheet at the apex of Bar 6 (from 2017). Inset
974 shows the one-metre tall slip face at the downstream extent of the sheet

975 **Figure 14.** Box plots of scaled tracer path lengths as a function of initial morphologic unit. Note:
976 the box represents the 25th and 75th percentiles; the line inside the box is the median; vertical
977 lines represent the 10th and 90th percentiles.

978 **Figure 15.** Tracer burial for Bar 6 and Bar 7. The position of buried tracers that were recovered
979 between 2015 and 2018 are overlaid on the corresponding DoD in the upper panel. Those
980 recovered in 2019 are shown in the lower panel ovetop of the 2018-2019 DoD.

981 **Figure 16.** Tracer burial for Bar 15. The position of buried tracers that were recovered between
982 2015 and 2018 are overlaid on the corresponding DoD in the upper panel. Those recovered in
983 2019 are shown in the lower panel ovetop of the 2018-2019 DoD.

984 **Figure 17.** Tracer burial depth plotted against net elevation change in the DoD for the cell in
985 which the tracer was buried.

986 **Figure 18.** Tracer burial depths for (a) Bar 6, (b) Bar 7, and (c) Bar 15.

987 **Figure 19.** Path length (L) of individual tracers as a function of scaled grain size (D) for each
988 size fraction of tracers. Path length is scaled by the mean path length of the size fraction
989 containing the local D_{50} . Grain size is scaled by the D_{50} of local bed surface material. Yellow
990 dots represent the mean path length for each tracer size fraction across the three study sites. Note
991 that previous studies have scaled particle size by the local subsurface D_{50} , whereas the San Juan
992 data was scaled by the local surface D_{50} as no bulk grain size sampling was carried out.

993 **Figure 20.** Relative tracer mobility plotted as a function of grain size for each tracer size fraction
994 across all study sites. Grain size is scaled by the D_{50} of local surface bed material.

995 **Figure 21.** Mean scaled travel distance as a function of dimensionless stream power for various
996 channel types and the San Juan River. This figure is re-created from Figure 4 in Vázquez-Tarrío
997 et al. (2018).

998

999

1000

1001

1002

1003

1004

1005

1006

1007

1008

1009

1010

1011

1012

1013

1014

1015

1016

1017

1018

1019

1020

1021 **Table 1.** Grain size data for tracers and surficial bed material.

1022

Location	b-axis percentile	Grain Size (mm)		
		Tracers	Bed Material	Bed Material (Truncated)
Bar 6	D ₁₆	28-39	26	32
	D ₅₀	45-54	50	55
	D ₈₄	73-87	84	86
Bar 7	D ₁₆	28-29	16	34
	D ₅₀	45-46	43	56
	D ₈₄	73-74	87	97
Bar 15	D ₁₆	28-30	8	27
	D ₅₀	45-51	28	42
	D ₈₄	73-82	67	87

1023

1024

1025

1026

1027

1028

1029

1030

1031

1032

1033

1034

1035

1036

1037

1038

1039

1040

1041

1042 **Table 2.** Lidar survey metadata (sourced from TRS Inc., 2018a,b, 2019).

1043

Year of Survey	RMSE _v (m)	σ_v (m)	Average point density (points/m ²)
2015	0.026	0.036	12.8 ± 7.2
2018	0.032	0.037	28 ± 16.0
2019	0.069	0.062	38 ± 11.0

1044

1045

1046

1047

1048

1049

1050

1051

1052

1053

1054

1055

1056

1057

1058

1059

1060

1061

1062

1063

1064

1065

1066

1067

1068

1069

1070 **Table 3.** Summary of annual floods and tracer recovery results. Mobility rate is calculated as the fraction of tracers that were
 1071 recovered more than ten metres downstream of their initial position. Tracer path lengths are scaled by the length of the bar at which
 1072 they were seeded. Average burial depths include surface tracers.

1073

	Number of Events $Q > Q_{bf}$	Maximum Peak Discharge, Q_{max} ($m^3 s^{-1}$)	Total Excess Flow Energy, Ω_T ($MJ m^{-1}$)	Recovery Rate, R (%)	Mobility Rate, r_m	Median Path Length (m)	Median Scaled Path Length, L_{50}	Maximum Scaled Path Length, L_{max}	Average Burial Depth, B_{avg} (cm)
Bar 6									
2015-16	6	1,022	571	33	0.82	38	0.07	0.46	9.8
2016-17	4	749	331	66	0.89	69	0.12	0.78	5.7
2017-18	6	1,003	890	71	0.91	130	0.23	2.02	16.4
2018-19	5	942	479	75	0.88	155	0.28	0.79	19.6
Bar 7									
2016-17	4	749	331	76	0.80	97	0.18	0.92	4.4
2017-18	6	1,003	890	69	0.87	187	0.35	0.94	14.9
2018-19	5	942	479	79	0.93	219	0.41	1.41	13.0
Bar 15									
2016-17	4	749	180	70	0.48	155	0.27	0.96	5.1
2017-18	6	1,003	483	65	0.92	308	0.54	1.27	8.4
2018-19	5	942	260	75	0.94	197	0.32	1.34	8.5

1074

1075

1076

1077

1078

1079

1080

Formatted: Numbering: Continuous

1081 | **Table 4.** Tracer mobility and path length data aggregated across all years of tracer deployment
 1082 for each study site.

1083

	Bar 6	Bar 7	Bar 15
n_m	259	250	218
r_m	0.89	0.87	0.78
L_{50}	0.22	0.34	0.40
$n_{L>1.0}$	1	12	8
$r_{L>1.0}$	0.00	0.05	0.04
L_{max}	2.02	1.41	1.34

1084

1085 Note: n_m – number of mobile tracers, r_m – mobility rate, L_{50} – median scaled path length, $n_{L>1.0}$ –
 1086 number of tracers transported more than one bar length downstream, $r_{L>1.0}$ – tracer escape rate,
 1087 L_{max} – maximum observed scaled path length

1088

1089

1090

1091

1092

1093

1094

1095

1096

1097

1098

1099

1100

1101

1102

1103

1104

1105

1106

1107

Formatted: Numbering: Continuous

1108 **Table 5.** Tracer mobility and path length breakdown by initial morphologic unit.
 1109

Bar 6	Initial Morphologic Unit			Bar 6 (2016)	Initial Morphologic Unit	
	bar head	wetted channel	bar tail		bar edge	wetted channel
r_m	1.00	0.96	0.77	r_m	0.75	0.96
L_{50}	0.27	0.21	0.21	L_{50}	0.11	0.17
L_{max}	0.86	0.92	2.02	L_{max}	0.28	0.78

Bar 7	Initial Morphologic Unit		Bar 15	Initial Morphologic Unit		
	wetted channel	bar tail		bar head	wetted channel	bar tail
r_m	0.94	0.82	r_m	0.98	0.73	0.80
L_{50}	0.39	0.21	L_{50}	0.50	0.42	0.27
L_{max}	1.24	1.41	L_{max}	0.93	1.27	1.34

1110
 1111
 1112
 1113
 1114
 1115
 1116
 1117
 1118
 1119
 1120
 1121
 1122
 1123
 1124
 1125
 1126
 1127
 1128
 1129
 1130
 1131
 1132
 1133
 1134
 1135
 1136
 1137

1138 **Table 6.** Summary of tracer recovery in areas of morphologic change. Note: the fraction of
 1139 recovered tracers in brackets reflect recovery in areas of known morphologic change (i.e. tracers
 1140 deposited in areas of indeterminate change removed).
 1141

Location	Net Change in DoD				
	Indeterminate	Erosion		Deposition	
	Fraction of Recovered Tracers	Fraction of Recovered Tracers	B_{avg} (cm)	Fraction of Recovered Tracers	B_{avg} (cm)
Bar 6	0.51	0.06 (0.12)	12.1	0.43 (0.88)	18.5
Bar 7	0.35	0.06 (0.09)	5.1	0.59 (0.91)	10.3
Bar 15	0.73	0.08 (0.30)	5.7	0.19 (0.70)	10.6

1142

1143